

PACKAGING-INDUCED STRESSES ON MICROELECTROMECHANICAL
SYSTEMS

BY

DAPENG LIU

BS, Harbin Institute of Technology, 2009

DISSERTATION

Submitted in partial fulfillment of the requirements for
the degree of Doctor of Philosophy in Mechanical Engineering
in the Graduate School of
Binghamton University
State University of New York
2015

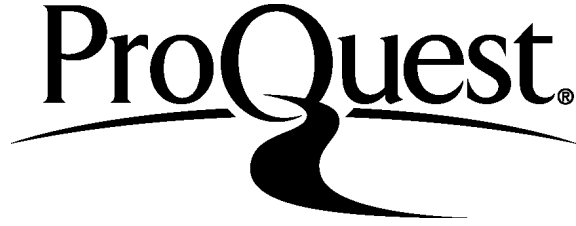
ProQuest Number: 10003700

All rights reserved

INFORMATION TO ALL USERS

The quality of this reproduction is dependent upon the quality of the copy submitted.

In the unlikely event that the author did not send a complete manuscript and there are missing pages, these will be noted. Also, if material had to be removed, a note will indicate the deletion.



ProQuest 10003700

Published by ProQuest LLC (2016). Copyright of the Dissertation is held by the Author.

All rights reserved.

This work is protected against unauthorized copying under Title 17, United States Code
Microform Edition © ProQuest LLC.

ProQuest LLC.
789 East Eisenhower Parkway
P.O. Box 1346
Ann Arbor, MI 48106 - 1346

© Copyright by Dapeng Liu 2015

All Rights Reserved

Accepted in partial fulfillment of the requirements for
the degree of Doctor of Philosophy in Mechanical Engineering
in the Graduate School of
Binghamton University
State University of New York
2015

October 02, 2015

Dr. Seungbae Park, Chair and Faculty Advisor
Department of Mechanical Engineering, Binghamton University

Dr. James M. Pitarresi, Member
Department of Mechanical Engineering, Binghamton University

Dr. Changhong Ke, Member
Department of Mechanical Engineering, Binghamton University

Dr. Shuxia Susan Lu, Member
Department of System Science and Industrial Engineering, Binghamton University

Dr. Yu Chen, Outside Examiner
Department of Electrical and Computer Engineering, Binghamton University

Abstract

Currently, several novel electronic products, such as various sensors utilizing microelectromechanical system (MEMS) technologies, have been introduced into the market. MEMS components have structures different from those of conventional electronic devices. As compared with most traditional integrated circuit (IC) products, packaging exhibits a greater influence on the performance of MEMS devices. For MEMS products, packaging-induced stress causes not only reliability issues but also performance concerns.

Overmolded packaging solutions, which are widely used for IC applications because of their cost-effectiveness, are also used for MEMS sensors. As a polymer-based material, the molding compound exhibits several unique features. For example, material properties such as modulus and thermal expansion are strongly affected by the glass transition temperature. The molding compound exhibits time-dependent behavior such as viscoelasticity; it absorbs moisture and swells on absorption with moisture. In several cases, the combination of these issues leads to a complex coupled-field problem. A substantial part of this dissertation is dedicated toward the effects of time, temperature, and moisture on the die stresses of MEMS by the finite-element method (Chapters 2–4). First, the effect of each individual factor is introduced, followed by a comprehensive study on their combined effects.

On the other hand, 3D packaging utilizing through-silicon-vias (TSVs) technology is being implemented by industry because of the increasing demand for a compact form factor, superior performance, and low cost. By providing a vertical electrical connection completely passing through a silicon die, this technology is reshaping the architecture of packaging. The TSV technology is being applied in several applications, such as IC and MEMS products. However, thermomechanical stress caused by the mismatch of thermal expansion is one of the major concerns for TSVs. In the second part of this dissertation (Chapters 5 and 6), the reliability risks for a type of TSV used for MEMS packaging are assessed. The TSV has a copper layer covering the side walls and bottom and a polymer-filled cavity. Stresses in risk sites are studied and ranked for this TSV structure by FEA modeling.

Acknowledgments

I would like to express my gratitude to my advisor Dr. Seungbae Park for his guidance throughout my research. The knowledge and technical skills that I have gained under his guidance will help me in building a successful professional career.

I would like to thank my committee members Dr. James Pitarresi, Dr. Changhong Ke, and Dr. Susan Lu for providing their valuable suggestions during my research.

I would also like to thank Prof. Frank Cardullo and Dr. Roy McGrann. I have worked as their teaching assistants in my first year at Binghamton and have considerably learnt from that experience. Working with them has been memorable. I would also like to thank Dr. Stephen Cain, Ms. Debbie Dittrich, Mr. Bill Infantolino, and Mr. Ron Kuracina of the Integrated Electronics Engineering Center for coordinating projects, which provided opportunities for more exposure to the packaging industry. In addition, I would like to thank Dr. Lawrence Lehman, Dr. Dae Young Jung, Mr. Bill Butler, and Mr. Chuck Waitkus for training me on the equipment in Analytical and Diagnostics Laboratory and giving me suggestions while performing experiments.

I would like thank the members of MEMS design team and packaging team of Analog Devices, Inc. at Wilmington, Massachusetts. It is a great honor to work with such a prestigious team and explore the world of electronic packaging.

Finally, I would also like to thank all members (as well as former members) in Dr. Park's research group for providing immense support and sharing their thoughts with me. It is a complete pleasure to be in such an innovative and productive group.

IN MEMORY OF

My Grandmother Chunyu Lin (1926–2012)

And Grandfather Yunchang Wang (1930–2015)

Table of Contents

List of Tables	xiii
List of Figures	xiv
Chapter 1. Introduction	1
1.1. Fundamentals of Electronic Packaging.....	1
1.1.1. Levels of Packaging	1
1.2. Packaging-Related Issues in Mechanical Engineering	4
1.2.1. Thermal Management	5
1.2.2. Thermomechanical Reliability	5
1.2.3. Reliability under Shock or Vibration	6
1.2.4. Moisture-Related Problems.....	6
1.2.5. Electromigration.....	7
1.2.6. Combined Loading Conditions	7
1.3. Research in This Dissertation	8
1.3.1. Effect of the Molding Compound on the Die Stress of MEMS Sensors	8
1.3.2. 3D Packaging and Its Implementation in MEMS	10
Chapter 2. Viscoelastic Behavior of Molding Compound and Its Effect on Stress	
Evolution in MEMS Packaging	16
2.1. Packaging Stress	16
2.2. Viscoelasticity.....	17
2.2.1. Generalized Maxwell Model and Prony Series.....	18
2.2.2. Time–Temperature Equivalence and Shift Functions.....	19
2.2.3. Dynamic Modulus.....	22

2.3. Effect of Viscoelastic Properties on Packaging Stress	24
2.3.1. Structure of the MEMS Sensor	24
2.3.2. Characterization of Material Properties	26
2.3.3. Stress vs. Time and Temperature	27
2.4. Summary	35
Chapter 3. Moisture Diffusion and Hygroscopic Swelling.....	36
3.1. Fundamentals of Moisture Diffusion and Related Issues	36
3.1.1. Hygroscopic Swelling	38
3.2. Mathematical Model for Moisture Diffusion.....	38
3.2.1. Fick's Law.....	38
3.2.2. Discontinuity of Concentration at the Material Interface	40
3.3. Finite Element Modeling of Diffusion Behavior	41
3.3.1. Analogy Method	41
3.3.2. Diffusion Elements and Coupled-Field Elements in ANSYS	45
3.3.3. The Direct Concentration Approach	50
3.4. Measuring Material Properties for Diffusion Analysis.....	62
3.4.1. Measuring Saturated Concentration and Diffusivity	63
3.4.2. Measuring CHS.....	66
3.5. Summary	74
Chapter 4. Conjugate Problem of Thermomechanical and Hygroscopic Loading	
with Viscoelastic Material Properties	75
4.1. Problem Statement	75
4.1.1. T_g Shift	76

4.2. Finite Element Simulation	78
4.2.1. Enhancing Solution Efficiency	80
4.2.2. Validation Simulation	82
4.2.3. Moisture Change during Temperature Cycle	84
4.2.4. Implementation of T_g Shift Effect in Simulation	86
4.2.5. Effect of Non-Uniform Moisture Distribution on the Stress Relaxation Behavior	90
4.3. Summary	96
Chapter 5. Introduction to 3D Packaging	98
5.1. Background	98
5.2. Chip-to-Chip and Chip-to-Wafer Interconnection	101
5.2.1. Bump Structure	102
5.2.2. Bumping and Assembly Process	105
5.2.3. Issues on Underfill	113
5.3. Wafer-to-Wafer Interconnection	116
5.3.1. With Simultaneous Underfill	117
5.3.2. Without Underfill	123
5.4. Summary	125
Chapter 6. TSV Technology in MEMS Packaging	126
6.1. Uniqueness of 3D Packaging for MEMS Application	126
6.1.1. Typical Structure of MEMS Sensor Packages	127
6.1.2. Stacking Schemes for 3D MEMS Packaging	127
6.2. Reliability of TSV	128

6.2.1. Effect of the Polymer Material Properties: CTE and Young's Modulus	130
6.3. Summary	133
Chapter 7. Closure	134
Reference	136

List of Tables

Table 1-1 Pros and cons of different 3D stacking schemes	12
Table 2-1 Material properties (except those of the molding compound and die attach adhesive)	26
Table 2-2 Material properties of the molding compound and die attach adhesive.....	27
Table 3-1 Material properties for analysis cases.....	47
Table 3-2 Material properties for “virtual CHS measurement” simulation.....	69
Table 3-3 Diffusivity and CHS values at various temperatures	74
Table 4-1 Prony pairs and the shift function of molding compound and die attach adhesive.....	79
Table 4-2 WLF shift function of molding compound and die attach adhesive	80
Table 4-3 Material properties for MEMS stress simulation	80
Table 6-1 Material properties for TSV stress simulation.....	131

List of Figures

Figure 1-1 Electronic packaging levels.....	2
Figure 1-2 Via-first, via-middle, and via-last approaches	11
Figure 1-3 TSV used in the MEMS product by STMicroelectronics	13
Figure 1-4 A MEMS package without wire bonds	14
Figure 1-5 Heterogeneous integration by TSV technology	15
Figure 2-1 Generalized Maxwell model	18
Figure 2-2 Stress relaxation test.....	19
Figure 2-3 3D model of the whole MEMS sensor	25
Figure 2-4 3D model of the MEMS showing the detailed structure	25
Figure 2-5 Temperature profile used to compare the effect of different final temperatures	29
Figure 2-6 Temperature profile used to compare the effect of different cooling rates.....	29
Figure 2-7 Thermal stress in both the X- and Y-directions at room temperature.....	30
Figure 2-8 Curve of thermal stress vs. time under different environment temperatures with the same cooling time constant.....	31
Figure 2-9 Thermal stress vs. temperature change curve	32
Figure 2-10 Stress–time curve showing the effect of different cooling rates on thermal stress.....	33
Figure 2-11 Curve of stress versus temperature showing the effect of different cooling rates on thermal stress.....	34
Figure 3-1 Schematic of “pop-corning” occurring at reflow	37
Figure 3-2 Concentration of moisture across the bimaterial boundary	40

Figure 3-3 Geometry and boundary conditions for the case study	47
Figure 3-4 Moisture concentration in a bimaterial specimen subject to the transient thermal condition ($t = 1800$ s).....	48
Figure 3-5 Moisture concentration in a bimaterial specimen subject to the transient thermal condition ($t = 3600$ s).....	48
Figure 3-6 Comparison of the moisture concentration and diffusion flux in a bimaterial specimen under the transient thermal condition calculated by the direct concentration approach with finite difference method and/or the normalized approach	52
Figure 3-7 Sandwich structure with two materials	53
Figure 3-8 Concentration of moisture on the left half of the sandwich structure	54
Figure 3-9 Diffusion flux on the left half of the sandwich structure	54
Figure 3-10 Geometry and boundary conditions for finite element analysis.....	55
Figure 3-11 Plot of moisture absorption with respect to time	65
Figure 3-12 Moisture weight gain and Fickian curves of the moisture desorption test under various temperatures	66
Figure 3-13 Setup of the DIC system	68
Figure 3-14 Calculation of averaged strain.....	70
Figure 3-15 Plot of strain versus concentration with the calculated CHS value from linear regression (Averaged approach I).....	71
Figure 3-16 Plot of strain versus concentration with the CHS values calculated from linear regression (Averaged approach II)	71
Figure 3-17 Plot of strain versus concentration with the CHS values calculated from linear regression (Local integration).....	72

Figure 3-18 Plot of strain versus concentration with the CHS values calculated from linear regression (DIC-based approach)	72
Figure 3-19 Hygroscopic strain at various temperatures	73
Figure 4-1 DMA result of dried, saturated, and baked specimen	77
Figure 4-2 FEA model and diagonal to obtain the out-of-plane deformation	79
Figure 4-3 Schematic cross section of the MEMS package	79
Figure 4-4 Deformation from experimental measurement using DIC	83
Figure 4-5 Deformation obtained from simulation	84
Figure 4-6 Desorption of moisture during temperature cycling	85
Figure 4-7 Effect of changing the reference temperature of the shift function	88
Figure 4-8 MEMS stress during temperature cycling	89
Figure 4-9 Flow chart showing the simulation using APDL	92
Figure 4-10 Effect of non-uniform moisture distribution on the stress relaxation behavior of the molding compound and resulted stress on MEMS die	93
Figure 5-1 3D SiP with wire bonds and flip-chip bumps	99
Figure 5-2 Cross-sectional image of a package with an interposer containing TSVs developed by Xilinx	101
Figure 5-3 Cross-sectional image showing interlocking Sn/Cu bumps and a Cu planar bump with TSVs	104
Figure 5-4 Image of the fabricated micro-inserts	104
Figure 5-5 Process of solder transfer in C4NP technologies	106
Figure 5-6 Cross-sectional image of Cu-filled TSV with Cu micro-bumps and X-ray photo of TSV after Sn plating	107

Figure 5-7 Schematic of SBM bumping	108
Figure 5-8 Cross-sectional image showing TSVs and coined bumps.....	108
Figure 5-9 A three-layer chip stack fabricated with sequential reflow by IBM	110
Figure 5-10 A gap exposed using a typical 50% corner fillet value in underfill dispensing	114
Figure 5-11 SEM image of flip-chip samples after capillary and vacuum underfill dispensing	114
Figure 5-12 Schematic of the process flow of wafer-to-wafer hybrid bonding.....	119
Figure 5-13 Cross-sectional images of TSVs and micro-bumps	119
Figure 5-14 SEM cross-sectional image of the joint structure before and after bonding	120
Figure 5-15 Comparison of the conventional joint structure and the WOW bumpless structure.....	121
Figure 5-16 Process flow of the WOW bumpless interconnection technology	122
Figure 5-17 A seven-layer wafer-stacking structure using the WOW process.....	122
Figure 5-18 Schematic of bonding an SOI wafer to the bottom wafer based on the IBM platform.....	124
Figure 5-19 SEM image of a four-layer stack fabricated with SiO ₂ fusion bonding	124
Figure 5-20 SEM cross-sectional image showing a TSV connecting two bonded wafers	124
Figure 6-1 Schematic of the cross-sectional image of the MEMS sensor with TSVs through the CMOS IC die	128
Figure 6-2 Schematic of a TSV structure	129

Figure 6-3 Schematic showing the critical location for TSV	130
Figure 6-4 Effect of CTE and Young's modulus of the TSV polymer on TSV stress at three critical locations	132
Figure 6-5 Effect of Young's modulus on the von Mises stress at the critical locations	133

Chapter 1. Introduction

1.1. Fundamentals of Electronic Packaging

For decades, one of the driving forces for the advancement of the electronic industry has been the progress of electronic packaging technology. This technology involves the assembly of components in a system, creation of electrical interconnections, and enclosure of the components or assemblies for protection. Electronic packages provide paths for power and signal distribution of an electrical system, protect internal devices from the environment, and dissipate the heat generated by the encapsulated components. Thus, the design of electronic packages significantly affects the performance and reliability of a complete electronic system.

1.1.1. Levels of Packaging

Modern electronic systems have very complicated structures; hence, an electronic packaging system consists of several levels. Figure 1-1 shows the schematic of one widely used classification method [1], where a complete packaging system is divided into three levels. First-level packaging refers to the assembly and connection of chips to the chip carrier, followed by encapsulation, if necessary. In second-level packaging, the first-level packages are connected to a printed circuit board (PCB) or circuit card. Then, the PCBs are mounted to the motherboard, forming third-level packaging. The definitions of these packaging levels might be slightly different in other studies [2]. For examples, a

level 0 might be used to refer to the interconnection between the devices in one chip, while fourth-level packaging might be used for more complicated electronic systems.

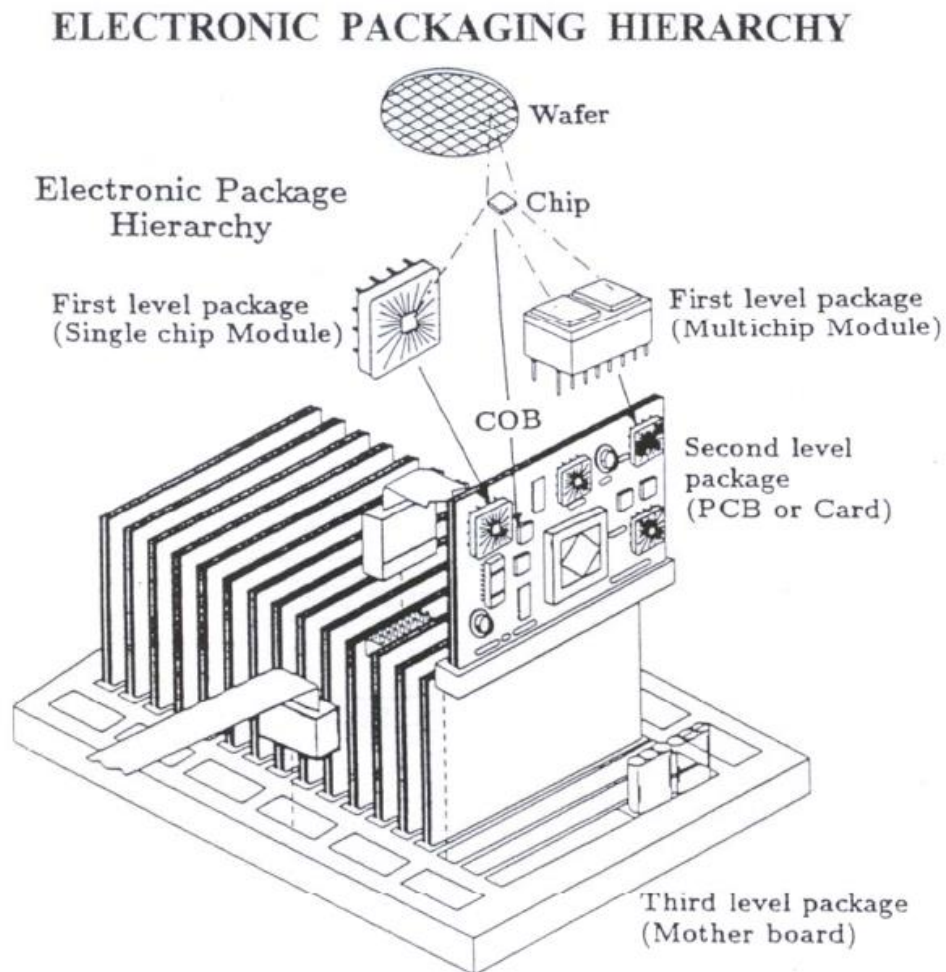


Figure 1-1 Electronic packaging levels [1]

1.1.1.1. First-Level Packaging

First-level packages can be classified into several categories based on the type of chip-substrate interconnect, substrate material, type of chip coverage, method of connection to the circuit board, and the shape and location of connections.

The connection of the chip to the substrate is a key technology for first-level packaging. For this key step, the three common bonding technologies are as follows: wire bonding, flip-chip bonding, and tape-automated bonding (TAB). In wire bonding, the silicon die is placed on the top of the substrate with a chip pad facing upwards, and metal wires are used to form the electrical connection between the chip and substrate by forming a ball or wedge bond. The most common combination of materials involves the bonding of a gold wire to an aluminum pad, while copper and aluminum wires are also widely used. Thermosonic, thermocompression, and ultrasonic methods can be employed for forming a bond. Wire bonding is widely used in packaging IC, MEMS, and light-emitting diodes (LEDs) [3].

In the 1960s, IBM developed the flip-chip technology [4], which is a method involving the connection of the chip to the substrate by conductive bumps. In this technology, the bumps are formed on the chip pads, and then chip is “flipped” and connected to the substrate. The conductive bumps serve as both mechanical and electrical connections. Flip-chip bonding not only significantly decreases the size of the package, but also leads to an increased number of inputs/outputs (I/Os) and better performance than wire bonding. Typically, flip-chip bumps are made by solder material by a reflow process, known as controlled collapse chip connection (C4), while other bumping (such as conductive adhesive and stub bond) and bonding methods (such as thermocompression) are also employed. For alleviating the mechanical stress induced by the coefficient of thermal expansion (CTE) mismatch and enhancing the reliability under temperature-cycling

conditions, underfill material is typically dispensed in the gap between the chip and substrate.

For TAB, the chip is first placed onto a flexible tape, and connected to the inner leads, creating interconnections, followed by testing. Then, the tape is moved to the target location, and the outer leads are cut and connected to the PCB substrate; finally, the package is encapsulated, and final testing is performed [5].

1.1.1.2. Second-Level Packaging

The first-level packages have to be further connected to the board for serving their functions, and the assembly of chip modules and other components on the PCBs is referred to as second-level packaging. Two common mounting schemes are as follows: pin-in-hole (PIH) and surface mount (SMT). The interconnections may be located in one or two lines on the periphery or on the bottom of the package as an array. SMT packages may have several different interconnected structures, such as ball grid array (BGA), land grid array (LGA), column grid array (CGA), J-lead, and gull wing. The connection can be designed to be pluggable if customization or replacement is often needed.

1.2. Packaging-Related Issues in Mechanical Engineering

Electronic packaging is an interdisciplinary area involving material science, electrical engineering, mechanical engineering, supply chain, and logistics. Within the domain of mechanical engineering, issues are predominantly divided into two categories: thermal

management and stresses induced by temperature and other environmental effects such as vibration and moisture.

1.2.1. Thermal Management

The generation of heat is inevitable for electronic products. For ensuring device operation at desired temperatures and preventing failures caused by thermal issues, the heat has to be dissipated. Thermal performance can be improved by the design of chip, package, PCB, or system, selection of materials, and choice of appropriate heat dissipation techniques. Heat dissipation approaches such as heat sinks, fans, and liquid cooling methods have been widely employed. Currently, several commercial software packages, such as Flotherm and Icepak (part of ANSYS), can be utilized to perform thermal analysis of electronic components and systems. With the continuous increase in the density of electronic devices, the challenges in thermal management will be more critical.

1.2.2. Thermomechanical Reliability

An electronic package is composed of different materials, and each material has its own CTE. Thermomechanical stresses are caused by the CTE mismatch between different materials. The electronic packaging process consists of multiple process steps, and the process temperature of each step can significantly vary. Hence, thermomechanical stresses exist in almost any electronic package. In addition, these packages experience temperature loading from internal heat sources and the environment.

Thermomechanical stress can adversely affect the reliability and performance of electronic components. The electronic components may fail because of over-stress failure; however, fatigue failure is more prevalent. For example, the temperature of the components increases when the devices are powered on and decreases when they are powered off. Thus, the components experience temperature cycles in their usage life. Solder joint reliability (SJR) under thermal loading is an important topic for electronic packaging. Besides, for some products such as MEMS sensors, stress also leads to the shift in the output signals, leading to less satisfactory performance. This issue will be one of the emphases of this dissertation.

1.2.3. Reliability under Shock or Vibration

Electronic components are exposed to vibration during manufacturing, transportation, and operation. Besides, these components may also be subjected to shock impact caused by either harsh usage conditions or accidental drop. Impact and vibration reliability have become crucial requirements as automotive electronics and portable consumer electronics are widely utilized [6].

1.2.4. Moisture-Related Problems

Moisture exhibits not only chemical but also mechanical effects on electronic packages. From the mechanical aspect, moisture can reduce the strength of some materials. Besides, volumetric expansion is associated with the absorption of moisture, which is referred to as hygroscopic swelling, resulting in stresses if different materials within the structure exhibit different extents of expansion. The situation is worse when moisture is vaporized

at high temperature. If an electronic package is to be soldered to the board by reflow soldering, which is common for SMT components, moisture sensitivity might be crucial. In a worst-case scenario, vapor pressure causes cracks and/or delamination with an audible sound. This phenomenon is referred to as popcorning. Chapter 3 will discuss moisture-related issues.

1.2.5. Electromigration

Electromigration is the transport of materials driven by the momentum transfer between the moving electrons and metal ions [7]. It can cause two failures: open circuit failure, caused by void formation, and short circuit failure, caused by unintended connection attributed to the piling up of conductive materials (i.e., whisker). Electromigration is mainly driven by the “electron wind force,” which is the product of atomic density and the drift velocity of moving ions; however, it is also significantly related to the temperature gradient and mechanical stress gradient [8]. Therefore, modeling electromigration using numerical methods can be very complicated.

1.2.6. Combined Loading Conditions

Under real usage conditions, an electronic package simultaneously experiences thermal, mechanical, and moisture conditions. Therefore, it is necessary to investigate the effect of combined loadings on the stress and/or life of the components and assemblies. Such combinations include: 1) vibration at different frequencies; 2) thermal cycling with power cycling; 3) thermal cycling with static mechanical loading; 4) thermal cycling with vibration; and 5) thermal and hygroscopic swelling. Miner’s damage rule has often been

employed for predicting fatigue life; however, some researchers have found that for some cases, Miner's rule does not accurately predict fatigue life because the mechanism of failure under the combined loading condition becomes different [9, 10]. Some prediction models based on damage mechanics have been proposed for predicting fatigue life under such conditions [10]. Besides, prognostication techniques have also been developed [11].

1.3. Research in This Dissertation

This dissertation focuses on the packaging of microelectromechanical systems (MEMS). The following chapters in this dissertation can be divided into two major parts. The first part, Chapters 2–4, discusses the effect of stress of the molding compound on MEMS dies. The second part, Chapters 5 and 6, discusses three-dimensional packaging techniques and their application in MEMS sensors, as well as studies and reliability issues associated with the TSVs. Chapter 7 summarizes the approaches and conclusions.

1.3.1. Effect of the Molding Compound on the Die Stress of MEMS

Sensors

Nowadays, overmolded packages have accounted for a major part of the packaging market. As compared to ceramic packages, overmolded packages can significantly decrease costs; hence, they have been widely used in integrated circuits (ICs), MEMS, and power electronics packaging. For overmolded packages, the molding compound comprises a significant portion of the total volume of the package. Hence, the properties

of the molding compound are crucial for the performance and reliability of the whole electronic component.

As a polymer-based material, the molding compound exhibits characteristics that are affected by time, temperature, and moisture. One of these material behaviors is viscoelasticity. As the name suggests, although the molding compound appears to be in a solid state, it also exhibits a viscous property similar to that of liquids. Because of viscoelasticity, the stress and strain state of the molding compound is dependent on time, and this material behavior is also affected by temperature. Besides, as a polymer-based material, several properties, such as CTE, are affected by the glass transition temperature (T_g), indicating that thermal expansion above and below T_g drastically changes. Furthermore, the molding compound absorbs moisture and swells upon exposure to a humid environment [12], while several other materials such as silicon and copper do not exhibit this behavior. Thus, hygroscopic swelling is another source of stress besides thermal expansion.

MEMS sensors are highly sensitive to stress. Hence, passing the reliability tests is necessary but not sufficient for the design of MEMS packages. Instead, the package designer has to make every endeavor to ensure that packaging stress is as low and constant as possible. Thus, viscoelasticity and moisture absorption should be considered for more accurately estimating stresses and strains inside the package. In this dissertation, Chapter 2 will discuss the effect of viscoelastic behavior, Chapter 3 will introduce moisture-related issues, and Chapter 4 will discuss the comprehensive effect.

1.3.2. 3D Packaging and Its Implementation in MEMS

Three-dimensional packages are electronic packages with stacked dies. In recent years, three-dimensional packaging has been attracting increasing attention because it allows for miniaturization, higher integration, and better performance. For ICs, the trend of integration density is described by the well-known Moore's Law: the number of transistors per unit area on ICs would roughly double every two years [13]. However, as the density of transistors increases, and the dimensions of the devices decreases, the further increase in the density of complex chips is becoming difficult and expensive by traditional approaches. However, using 3D architecture, circuits can be fabricated on different dies, and then these dies can be stacked and interconnected using packaging tools. A promising approach is to use through-silicon vias (TSVs) to provide a vertical path for electrical power and signal. As compared to wire bonding, TSV technology permits a significantly larger number of interconnects because the number of TSVs allowed in the die is proportional to the area of the chip, while wire bonds can only be distributed on the periphery of a die. Besides, TSVs provide significantly shorter distance for signal transmission than wire bonds. Thus, 3D packaging typically refers to stacking silicon dies (and/or wafers) and interconnecting those using TSVs.

1.3.2.1. TSV Fabrication: Via-First, Via-Middle, and Via-Last

Approaches

The fabrication of a TSV is one of the key processes in 3D packaging. Depending on when the TSV is made on the silicon wafer, the approaches for fabricating TSVs can be divided into three categories: via-first, via-middle, and via-last.

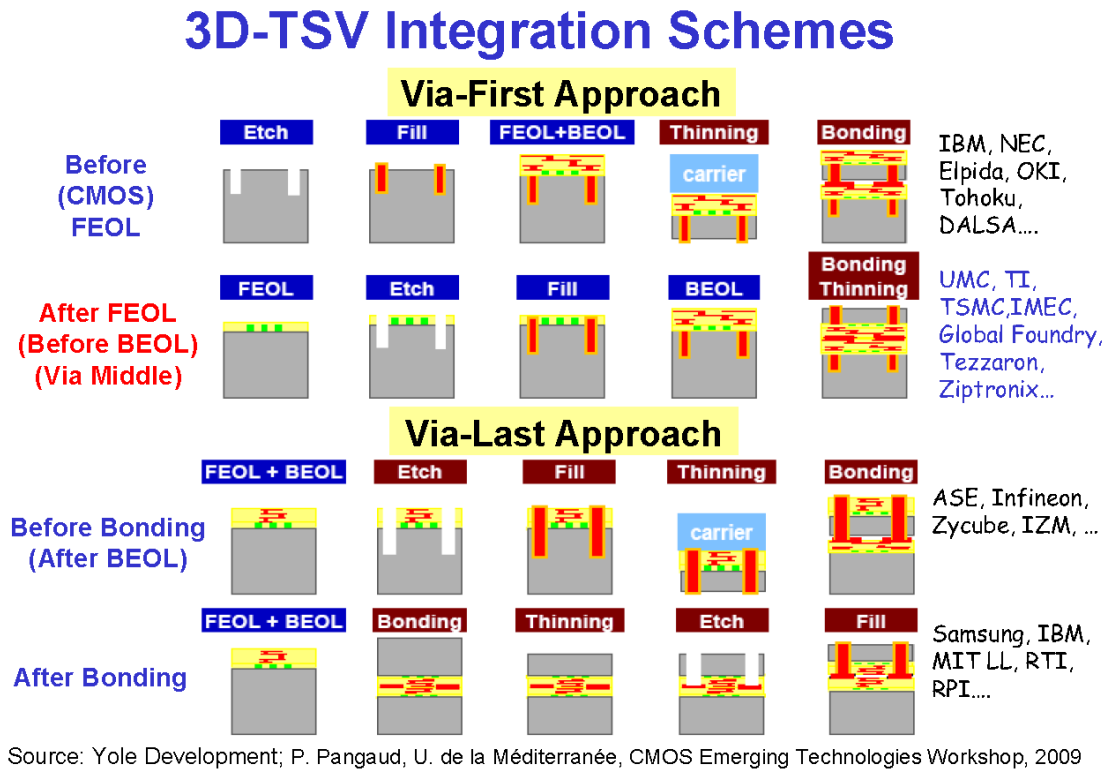


Figure 1-2 Via-first, via-middle, and via-last approaches [14]




The process for fabricating semiconductors can be divided into two stages: front-end-of-line (FEOL) and back-end-of-line (BEOL). In FEOL, individual devices such as transistors, capacitors, and resistors are patterned to the wafer, while in BEOL, those devices are connected with wirings on the wafer [15]. For the via-first approach, the

TSVs are fabricated before the FEOL. If the TSV is fabricated between the FEOL and BEOL, the process becomes via-middle, and in some studies [14], via-middle is considered as one variation of the via-first approach. For the via-last approach, the TSV is made after the BEOL, either before or after bonding. Most of the processes for fabricating TSVs require the thinning of wafers.

In recent years, extensive studies have been conducted on TSV fabrication. The typical procedure for making TSVs involves etching, deposition of an insulation layer and a seed layer, filling of the via using conductive materials, and chemical-mechanical planarization. The method of filling the via is dependent on the material; for copper, the most common material for via-filling, plating and chemical vapor deposition (CVD) are mostly employed.

1.3.2.2. Interconnecting the Dies

Table 1-1 Pros and cons of different 3D stacking schemes [16]

TSV interconnect methods			
	(1) C2C: chip-to-chip	(2) C2W: chip-to-wafer	(3) W2W: wafer-to-wafer
			
Pros	Flexible Use of KGD	Flexible Use of KGD	High throughput
Cons	Handling, Bonding	Handling, Bonding	Same chip size, Yield

Besides fabricating the TSVs, another important task is to bond the dies (chips) and/or wafers for creating an electrical connection between them. The methods for bonding and interconnection are categorized into three schemes: chip-to-chip (C2C), chip-to-wafer (C2W), and wafer-to-wafer (W2W). Table 1-1 lists the pros and cons for each stacking scheme, and Chapter 5 provides a review of the state-of-the-art of interconnection technologies.

1.3.2.3. Challenges, Applications, and Prospectus

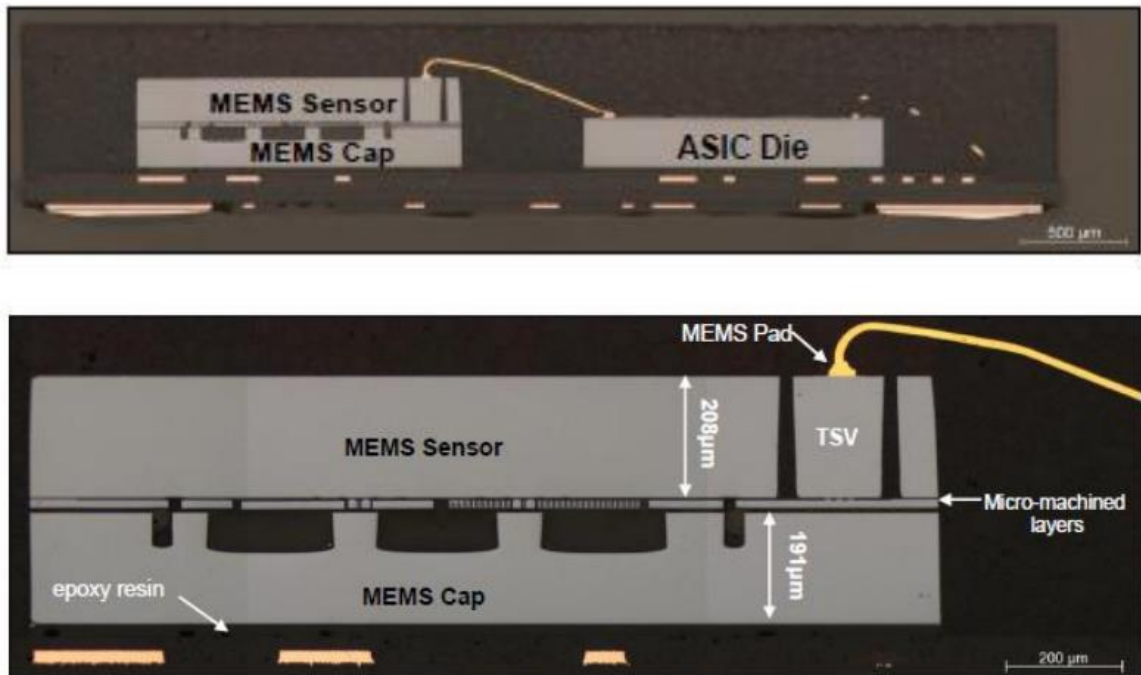


Figure 1-3 TSV used in the MEMS product by STMicroelectronics [17]

TSV-based 3D packaging is being accepted by the industry. Currently, it has been applied in interposers, memories, optical sensors, and MEMS products, etc. For MEMS products, although it does not contain a large number of I/Os and usually does not require

a great number of transistors to be integrated, 3D packaging does contribute to miniaturization. Besides, TSV technology permits more flexibility for the method of interconnection. For example, the wire bonds do not have to be on the side of MEMS devices (Figure 1-3). It is also possible to utilize the bonding methods that do not necessitate wire bonds (Figure 1-4).

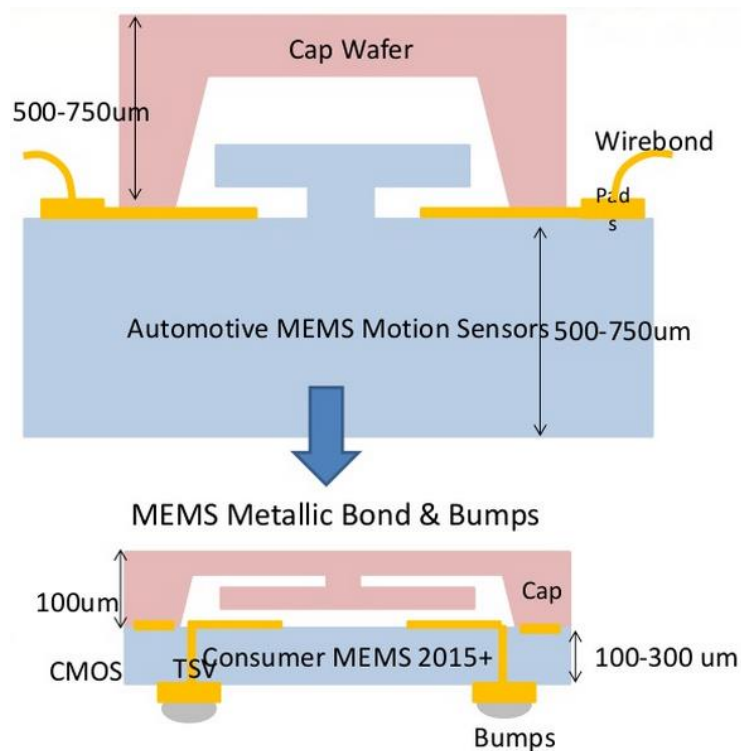


Figure 1-4 A MEMS package without wire bonds [18]

The prospective goal for 3D packaging is to achieve heterogeneous integration, which involves the integration of chips with significant different device technologies into a single package [19]. Heterogeneously integrated electronics are believed to be smart and powerful, with high performance, if this technology can be realized in the future.

TSV-based 3D packaging is a brand new area; hence, several challenges are observed. Beside the process development work such as via etching, filling, and wafer bonding, other challenges include thermal management, reliability (such as thermomechanical stress and electromigration), as well as establishing design rules and developing electronic design automation (EDA) tools. Thermal management is considered as one of the greatest challenges, albeit it is an exception for MEMS packaging. In this dissertation, TSV-related research is focused on thermomechanical reliability, which will be discussed in Chapter 6.

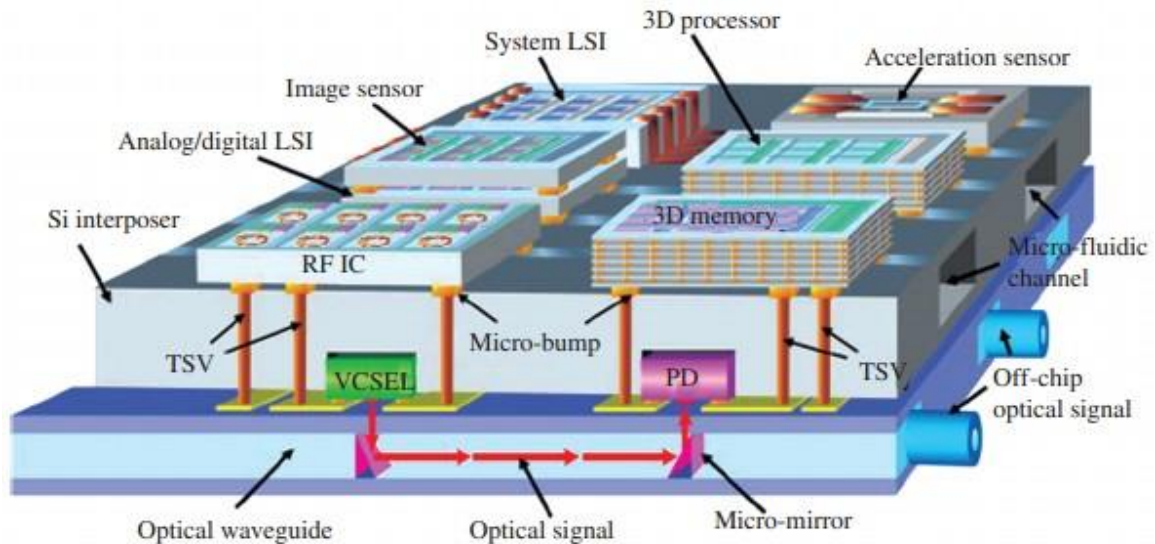


Figure 1-5 Heterogeneous integration by TSV technology [20]
 (LSI: Large Scale Integration; PD: Photodiode; RF: Radio Frequency; VCSEL: Vertical-Cavity Surface-Emitting Laser)

Chapter 2. Viscoelastic Behavior of Molding Compound and Its Effect on Stress Evolution in MEMS Packaging ¹

2.1. Packaging Stress

Packaging materials can considerably affect the reliability and performance of electronics components. On the one hand, materials such as the molding compound protect the package from the environment; while on the other hand, the different mechanical properties of different materials inevitably introduce stress into the package. Stress is an important concern for designers and manufacturers of MEMS. Stress causes not only physical failures but also performance issues [21-25]. For example, a high-sensitivity MEMS sensor may exhibit output signal offset problems caused by the residual stress originating from the cure shrinkage of the molding compound and the mismatch of the coefficient of thermal expansion (CTE) among different materials. Other factors that cause stress in electronic devices include the mismatch of the coefficient of hygroscopic swelling (CHS) and mechanical loading (static or vibration). In recent years, several researchers have employed different approaches for evaluating the packaging stress and its effect on MEMS.

¹ Part of this chapter is from Park, S., Liu, D., Kim, Y., et al., 2012, "Stress Evolution in an Encapsulated MEMS Package due to Viscoelasticity of Packaging Materials", 62nd Electronic Components and Technology Conference, May 29–June 1, San Diego, CA, with permission from IEEE. Copyright © 2012 IEEE.

2.2. Viscoelasticity

Among the different materials in the MEMS and other electronic packages, polymer-based molding compounds and die attach adhesives exhibit viscoelastic behavior. The viscoelasticity added complexity for accurately estimating packaging stress. Viscoelasticity is a time- and temperature-dependent property, and temperature and loading history may exhibit non-negligible roles in the evolution and final status of stress and strain for viscoelastic materials. For various reasons, the properties of such materials have often been treated simply as temperature-dependent elastic, and the time dependency is often ignored in finite element simulation. In some cases, it is true that this simplification reduces the computation time and cost, but for high-sensitivity devices such as MEMS sensors, time-dependent behavior must be considered for accurately assessing stress and evaluating its effect on output signal drifting.

In recent years, the viscoelasticity of packaging materials has drawn the attention of researchers. Several materials, which are commonly used in packaging, such as printed circuit board (PCB) material FR-4, are found to be actually viscoelastic. Kenner, Chae, and Woodworth have characterized the time-dependent property by experiments [26-28]. Ernst, Kim, and Krondorfer have measured stress relaxation and utilized the viscoelastic property in finite element model for investigating the effects of the material properties on the thermally loaded package, and their studies have shown that viscoelasticity may strongly affect the simulation result [23-25, 29, 30].

2.2.1. Generalized Maxwell Model and Prony Series

Properties of materials are crucial for accurately predicting stress and deformation by the numerical method. Unfortunately, viscoelasticity details are typically not available from material vendors. Therefore, measuring this material property and converting the data to a form acceptable by the FEA software is an integral part in this work. The ANSYS software utilizes the Prony series for representing the characteristics of viscoelastic materials.

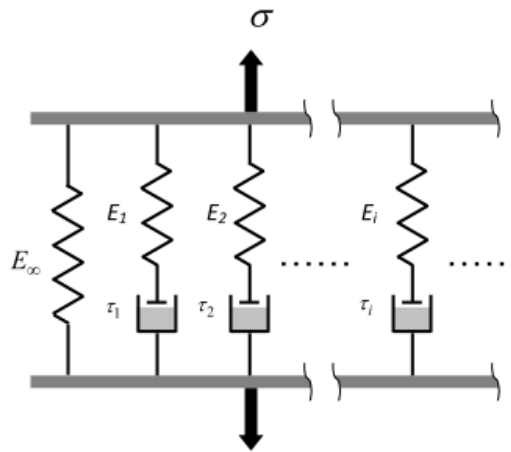


Figure 2-1 Generalized Maxwell model [28]

The meaning of the Prony series can be illustrated by the well-known generalized Maxwell model (also known as the Maxwell–Wiechert model or Wiechert model), which is shown in Figure 2-1. In this model, each Maxwell element, which is the combination of a spring and dashpot in series, exhibits its own viscosity and elasticity. Hence, assuming that a constant strain is applied (Figure 2-2), the relaxation modulus of the whole model can be expressed as

$$E(t) = \frac{\sigma(t)}{\varepsilon_0} = E_\infty + \sum_{i=1}^n E_i \exp\left(-\frac{t}{\tau_i}\right) \quad (2.1)$$

Here, $E(t)$ is the relaxation modulus, $\tau_i = \eta_i/E_i$ is the time constant, where η_i and E_i are the viscosity and modulus of the i^{th} component, respectively. This method of representation is called Prony series.

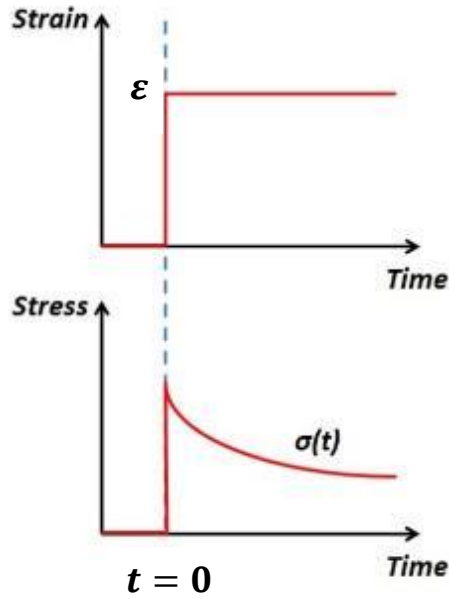


Figure 2-2 Stress relaxation test

2.2.2. Time–Temperature Equivalence and Shift Functions

Unlike other well-known rate-dependent models, Prony series does not contain any temperature term. For describing the effect of temperature, two methods are available. One method is to use different Prony series for different temperatures; however, the other method, shift function, is typically employed for adjusting the Prony series to adapt to different temperatures.

Suppose at temperature T_0 and time t_0 , the modulus can be expressed as

$$E(t_0^{(T_0)}) = E_\infty + \sum_{i=1}^n E_i \exp\left(-\frac{t_0^{(T_0)}}{\tau_i^{(T_0)}}\right) \quad (2.2)$$

At a higher temperature T_1 , the same relaxation modulus value is found at time t_1

$$E(t_1^{(T_1)}) = E_\infty + \sum_{i=1}^n E_i \exp\left(-\frac{t_1^{(T_1)}}{\tau_i^{(T_1)}}\right) = E(t_0^{(T_0)}) \quad (2.3)$$

Hence, we may obtain

$$\tau_i^{(T_0)} = \frac{t_0^{(T_0)}}{t_1^{(T_1)}} \tau_i^{(T_1)} \quad (2.4)$$

By substituting $\frac{t_0^{(T_0)}}{t_1^{(T_1)}} = A(T)$ and taking the logarithm, we get

$$\log(t_1^{(T_1)}) = \log(t_0^{(T_0)}) - \log A(T) \quad (2.5)$$

Hence, we can reach a conclusion that if we set time axis in a logarithmic scale, we can plot the stress relaxation curve under one temperature by shifting the curve obtained under another temperature. This is known as the time–temperature equivalence principle, and a material obeying this principle is referred to as a thermorheologically simple material. The logarithm of $A(T)$ is called the shift function.

2.2.2.1. Mastercurve

Under the assumption of a thermorheologically simple material, stress relaxation experiments can be performed at different temperatures, and the results can be fitted into a “mastercurve,” and then Prony series can be generated from the mastercurve. The shift distance can be determined and then used to determine the constants in the shift function. This process can be carried out by either using mathematical analysis tools or the built-in functions of FEA software. References [27, 31, 32] describe the method for obtaining Prony series and shift functions in detail.

2.2.2.2. Different Shift Functions

In engineering, the most frequently used shift function for polymers is the William–Landel–Ferry (WLF) function. The WLF function takes the following format:

$$\log_{10}A(T) = \frac{-C_1(T - T_{\text{ref}})}{C_2 + (T - T_{\text{ref}})} \quad (2.6)$$

Here,

C_1 and C_2 are two dimensionless constants, and

T_{ref} is a reference temperature chosen to construct the mastercurve.

Another commonly used shift function, the Tool–Narayanaswamy function, takes the Arrhenius form

$$\ln A(T) = \frac{H}{R} \left(\frac{1}{T_{\text{ref}}} - \frac{1}{T} \right) \quad (2.7)$$

Here, H/R represents the scaled activation energy. Another form of the Tool–Narayanaswamy shift function has a fictive temperature, which represents an intrinsic equilibrium temperature that is different from ambient temperature [33, 34]. Detail of this form will not be covered in this dissertation because such a form is rarely used for polymers.

ANSYS supports a user-defined shift function by using ANSYS user programmable features. Users may edit the Fortran subroutine “UsrShift.F” for writing their own shift function [33], if the WLF or Tool–Narayanaswamy does not fit well. For example, the “UsrShift.F” that comes with the ANSYS release describes a function with polynomial form by default:

$$\ln A(T) = C_1(T - T_{\text{ref}}) + C_2(T - T_{\text{ref}})^2 + C_3(T - T_{\text{ref}})^3 + \dots \quad (2.8)$$

Here, C_i is a material parameter. Users may choose to use the polynomial form or write any other shift functions and compile the subroutine and link to ANSYS.

2.2.3. Dynamic Modulus

Besides measuring the viscoelastic properties in the time domain employing the stress relaxation test, another common approach of characterization is dynamic mechanical analysis. In dynamic mechanical analysis, a sinusoidal stress is applied, and the strain in the material is measured. For viscoelastic material under vibratory conditions, the stress can be expressed as

$$\varepsilon = \varepsilon_0 \sin(t\omega) \quad (2.9)$$

and the stress can be expressed as

$$\sigma = \sigma_0 \sin(t\omega + \delta) \quad (2.10)$$

where $\omega = 2\pi f$, and f is the frequency of stress (strain) oscillation, t is the time, and δ is the phase lag.

A complex modulus is required to express the material behavior under such vibratory conditions. It can be divided into two parts: storage modulus and loss modulus:

$$E_{\text{comp}} = E_{\text{storage}} + jE_{\text{loss}} \quad (2.11)$$

where

$$E_{\text{storage}} = \frac{\sigma_0}{\varepsilon_0} \cos\delta \quad (2.12)$$

is the storage modulus representing the elastic portion,

$$E_{\text{loss}} = \frac{\sigma_0}{\varepsilon_0} \sin\delta \quad (2.13)$$

is the loss modulus representing the viscous portion, and $j = \sqrt{-1}$ is the imaginary unit.

2.2.3.1. Converting Prony Series to Storage Modulus and Loss

Modulus

The storage modulus and loss modulus can be calculated from Prony series by performing a Fourier transform [35]

$$E(\omega) = E_{\infty} + j\omega \sum_{i=1}^n \int_0^{\infty} E_i \exp(-i\omega t) dt \quad (2.14)$$

By separately taking the real and imaginary parts, we get

$$E_{\text{storage}} = E_0 \left(\alpha_\infty + \sum_{i=1}^n \frac{\alpha_i \tau_i^2 \omega^2}{1 + \tau_i^2 \omega^2} \right) \quad (2.15)$$

and

$$E_{\text{loss}} = E_0 \sum_{i=1}^n \frac{\alpha_i \tau_i \omega}{1 + \tau_i^2 \omega^2} \quad (2.16)$$

Here, $E_0 = E_\infty + \sum_{i=1}^n E_i$ is the modulus at $t = 0$, and $\alpha_i = E_i/E_0$ is the normalized modulus in Prony series.

The storage modulus and loss modulus can also be used as ANSYS input material properties².

2.3. Effect of Viscoelastic Properties on Packaging Stress

2.3.1. Structure of the MEMS Sensor

Figures 2-3 and 2-4 show the MEMS sensor package, which was studied using commercial FEA software ANSYS. Unlike the sensor studied by Krondorfer [23-25], in this package, the MEMS die is located on the top of the application-specific integrated circuit (ASIC) core, and they were attached by a die attach adhesive. The cap and the

² Use TBFIELD to define the setting to be dependent on and use TB, ELASTIC to define the material properties.

MEMS die are attached by sealing glass. The molding compound encapsulates the ASIC, die, and cap. The in-plane on the surface stress of the die center, which is located under that cap, will affect the output signal of this MEMS sensor.

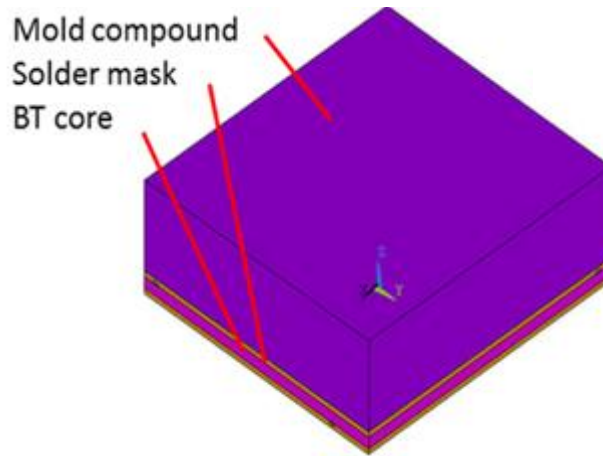


Figure 2-3 3D model of the whole MEMS sensor

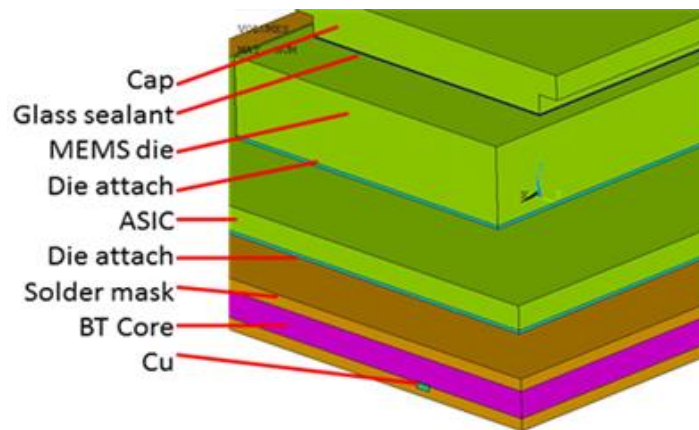


Figure 2-4 3D model of the MEMS showing the detailed structure (with mold removed)

2.3.2. Characterization of Material Properties

The properties of the molding compound and die attach adhesive used in the MEMS package are characterized by a series of experiments using dynamic mechanical analysis (DMA). The data for the die attach adhesive were obtained from the tensile test, while the molding compound was tested by the three-point bending method.

Table 2-1 Material properties (except those of the molding compound and die attach adhesive)

Material Property	Solder Mask	BT Core	Silicon	Seal Glass	Copper
CTE- α_1 ($10^{-6}/^{\circ}\text{C}$)	60	14	2.6	7	16.5
CTE- α_2 ($10^{-6}/^{\circ}\text{C}$)	130	5	-	-	-
T_g ($^{\circ}\text{C}$)	100	230	-	-	-
Modulus (GPa)	2.4	28	163	50	129
Poisson's ratio	0.2	0.3	0.22	0.3	0.35

Table 2-1 and 2-2 list the properties of the materials used in this study. As shown in Table 2-2, Prony series is normalized by dividing the modulus at time zero, as required by ANSYS. The modulus, Prony series, and shift functions of the molding compound and die attach adhesive are obtained from experiments, and other properties are provided by the material manufacturer. All viscoelastic properties are examined by simulating the experiment and comparing the simulation results with the experimental data.

Table 2-2 Material properties of the molding compound and die attach adhesive

	Die Attach		Molding Compound		
CTE- α_1 ($10^{-6}/^{\circ}\text{C}$)		98		9	
CTE- α_2 ($10^{-6}/^{\circ}\text{C}$)		174		34	
T_g ($^{\circ}\text{C}$)		-70		140	
Modulus (GPa)		2		22.6	
Poisson's ratio		0.35		0.35	
	Term	α_i	τ_i (s)	α_i	τ_i (s)
Normalized Prony Series	1	0.32	2.40×10^1	0.046	2.40×10^{-3}
	2	0.24	1.34×10^3	0.101	2.40×10^{-1}
	3	0.25	2.09×10^4	0.146	2.40×10^1
	4	0.083	5.13×10^5	0.246	2.40×10^3
	5	0.064	3.69×10^8	0.305	2.40×10^4
	6	-	-	0.128	2.40×10^6
Shift Function (WLF)	T_{ref}		-40		110
	C_1		12.03		-9.79
	C_2		111.8		-111.75

2.3.3. Stress vs. Time and Temperature

2.3.3.1. Profile of Thermal Loading

A curing temperature of 175 °C is used in the simulation. It is assumed that at this temperature, there is no thermal stress. A transient heat transfer analysis is performed for the generation of the cooling curve. Based on the dimension of the MEMS package, we can thus neglect the temperature non-uniformity within the object, and consider the temperature of the MEMS package as being a function of only time. Hence, the change in temperature is governed by a differential equation

$$Ah_f(T - T_\infty) = -\rho V c_p \frac{dT}{dt} \quad (2.17)$$

Here, T_∞ is the environment temperature, ρ is the density, V is the volume, A is the surface area, c_p is the specific heat, and h_f is the heat transfer coefficient (in other words, film coefficient), for natural convection in air, and h_f ranges from 1 to 10 W/(m²·K).

The solution yields

$$\frac{T - T_\infty}{T_i - T_\infty} = \exp\left(-\frac{t}{\tau}\right) \quad (2.18)$$

where T_i is the initial temperature, and $\tau = \rho V c / h A$ is the time constant. Obviously, the time constant only depends on material property, geometry, and convection condition, and it is independent of temperature. This equation can be further expressed as

$$T = (T_i - T_\infty)\exp(-t/\tau) + T_\infty \quad (2.19)$$

We assume that the MEMS sensor is then stored in an environment with constant temperature after cooling is completed.

Cases with different temperature profiles were simulated in the research:

1. Exponential decay to different temperatures (-25 °C, 25 °C, 45 °C, and 85 °C) with the same time constant (100 s).
2. Exponential decay to 25 °C with different time constants (50 s, 100 s, 300 s, and 600 s). $\tau = 100$ s is the closest to the manufacturing condition of this package.

For all cases mentioned above, the final time in the simulation is one week.

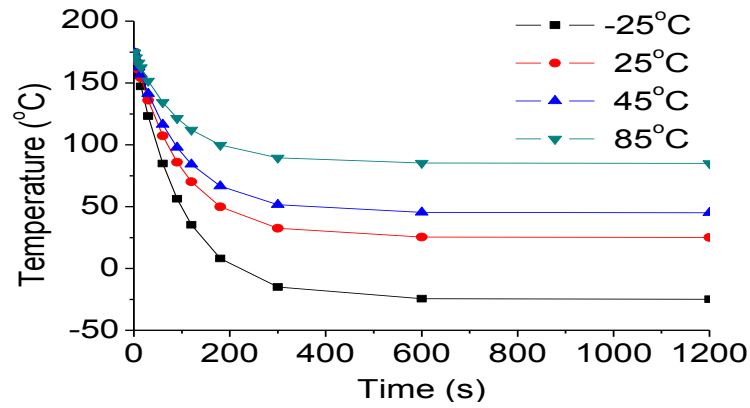


Figure 2-5 Temperature profile used to compare the effect of different final (working) temperatures

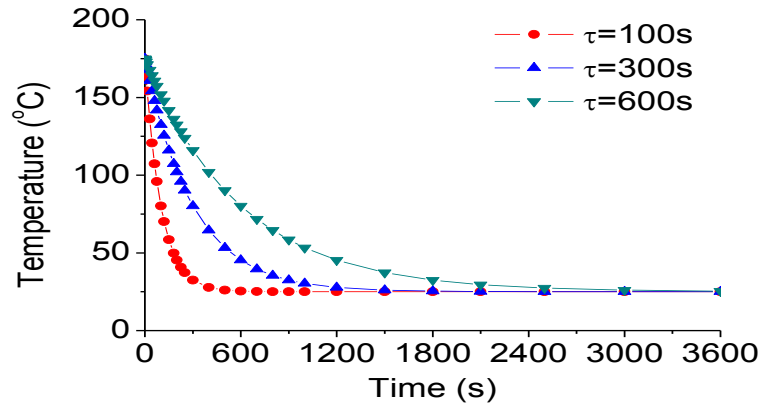


Figure 2-6 Temperature profile used to compare the effect of different cooling rates

2.3.3.2. Distribution and evolution of thermal stress

Stress in the in-plane direction of the die surface may affect the electrical performance of the package. Simulation results have shown that the Si die is subject to compressive stress in both x- and y-directions. The maximum compression stress occurs on the top surface of the die, as shown in Figure 2-7. The distribution of stress is approximately symmetric about the x-axis.

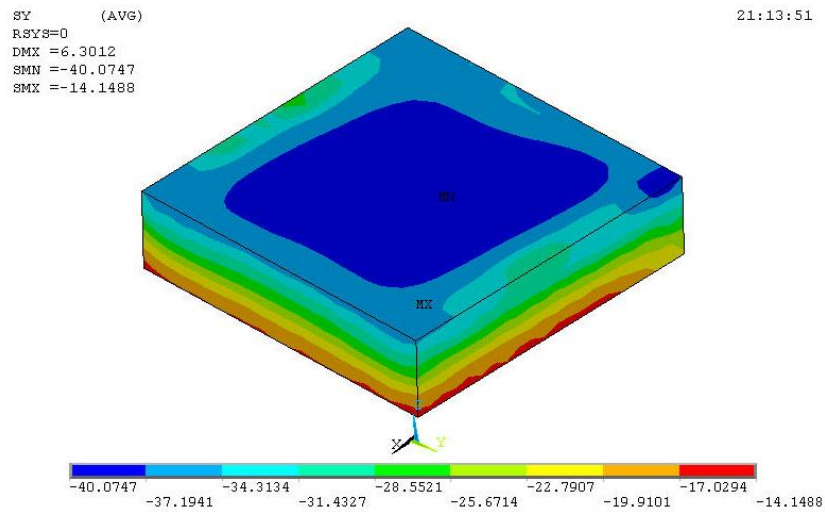
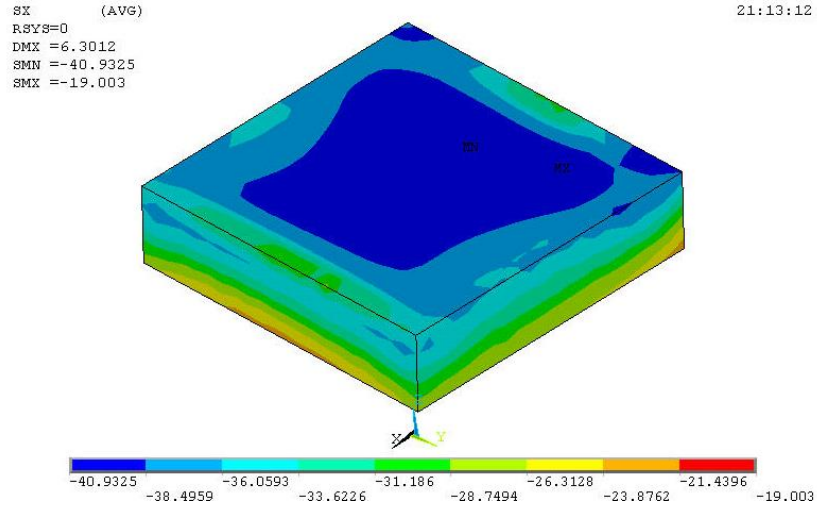


Figure 2-7 Thermal stress in both the X- (top) and Y-directions (bottom) at room temperature

For investigating the evolution of stress at the die center, the stress change is recorded on a node near the center of the die surface. Figure 2-8 and Figure 2-10 show the x-component of stress vs. time curves under different final temperatures and cooling rates. A logarithm scale is used for time, and the negative sign indicates that compression is

removed for the convenience of analysis. The stress–time curve for the y-component of stress is quite similar, with just a few percent differences in the magnitude.

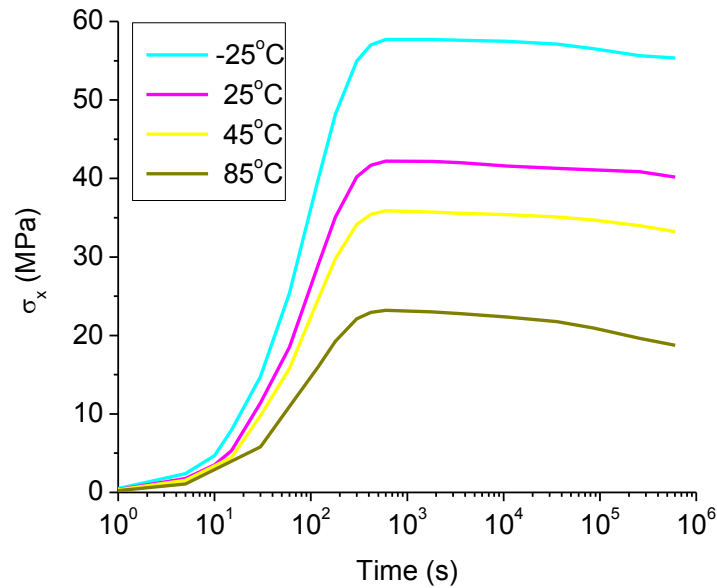


Figure 2-8 Curve of thermal stress vs. time under different environment temperatures with the same cooling time constant

In the cooling period, the change in temperature follows exponential decay. As temperature decreases, viscosity decreases, and the stress relaxation rate changes from fast to slow. Hence, stress rapidly increases.

When the temperature of the package gradually decreases to the final temperature, the temperature stabilizes at a constant value. In the constant temperature period, because of the viscoelasticity of the polymer material, stress slowly decreases with time, implying that the output signal shift may occur in the service life of a sensor. At higher temperature, this time-dependent behavior manifests (Figure 2-8).

The glass transition temperature T_g significantly affects material behavior. If we choose to plot a curve of stress versus temperature instead of stress versus time, we may observe that a turning point exists at the T_g of the molding compound, as shown in Figure 2-9.

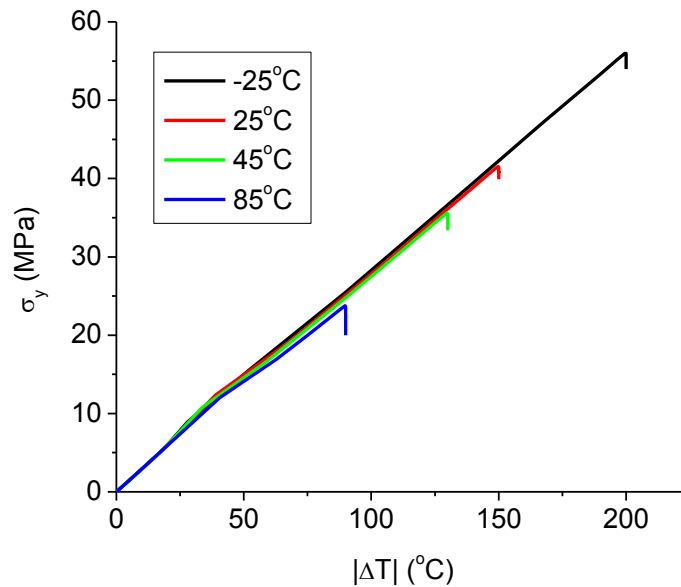


Figure 2-9 Thermal stress vs. temperature change curve

For the MEMS package studied in this case, thermomechanical stress results from the dependence of time and temperature of the polymer-based materials. The environmental temperature exhibits a strong effect.

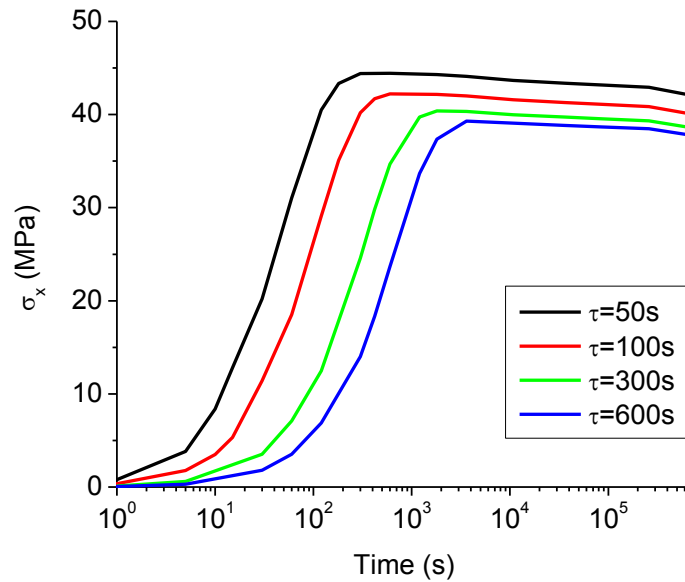


Figure 2-10 Stress–time curve showing the effect of different cooling rates on thermal stress ($T_{\infty} = 25^{\circ}\text{C}$)

2.3.3.3. Effect of the Cooling Rate

Viscoelasticity exhibits time-dependent behavior, and the loading history affects the final result. Hence, the history of temperature loading affects the stress level of the silicon die, even if the final temperature is the same. Although this feature is well known by material science researchers, few people have attempted simulating this effect on electronic components. In this study, we simulated the effect of different cooling rates by maintaining other parameters constant and changing the time constant. The result shows that the stress depends on the cooling rate. A slower cooling rate helps in the reduction of packaging stress, and a dramatic decrease in temperature may cause significantly greater stress (Figure 2-10).

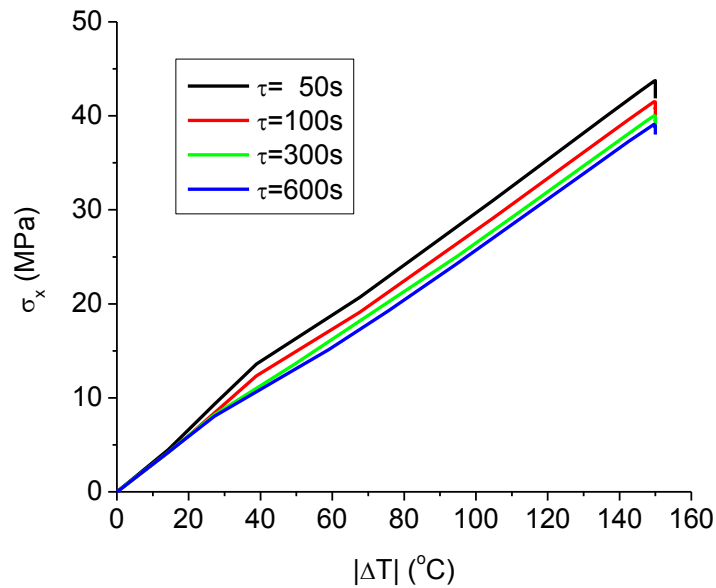


Figure 2-11 Curve of stress versus temperature showing the effect of different cooling rates on thermal stress ($T_{\infty} = 25^{\circ}\text{C}$)

Figure 2-11 shows the relation between the temperature and stress with different cooling time constants. From Figure 2-11, these curves clearly start to separate from each other when temperature almost decreases to T_g . When the temperature is lower than T_g , the curves almost become parallel with each other. Hence, we can further claim that the temperature range around T_g considerably affects thermal stress. Slow cooling will give the molding compound more time to relax its stress at temperature T_g . On the contrary, at a higher temperature, stress relaxation is rapid; hence, in all cases, the molding compound has sufficient time for stress relaxation. At low temperature, viscosity is weak, and the stress relaxation time is very long; hence, a short period of time does not significantly contribute to the packaging stress at that temperature. The dependency of the cooling rate actually indicates the necessity of utilizing the viscoelastic material model, because the

temperature-dependent elastic material model is probably not sufficiently accurate for electronic packages similar to the one studied in this research.

2.4. Summary

The stress change in a MEMS package was studied by finite element simulation. Results have shown that loading history, temperature, time, and cure shrinkage affect stress. Stress relaxation around T_g is crucial for the evolution of stress in the packages. In conclusion to this chapter, the intrinsic time-dependent feature of polymer-based materials may significantly affect the packaging stress in electronic packages; this effect should not be ignored, especially if the molding compound, which encapsulates a stress-sensitive component, experiences glass transition or its reverse process in manufacturing or usage.

Chapter 3. Moisture Diffusion and Hygroscopic Swelling

3.1. Fundamentals of Moisture Diffusion and Related Issues

Polymer-based materials typically absorb moisture. In the area of electronic packaging, these materials include the molding compound, die attach adhesive, underfill, and thin films for flexible substrates. These materials have been widely used in production because of several advantages such as cost, weight, and ease of manufacture; however, they also exhibit several disadvantages caused by moisture absorption.

As is widely known, moisture is often detrimental. For electronic products, the detrimental effects caused by moisture may include (but are not limited to):

- Corrosion of metal-based structures;
- Growth of dendrites;
- Current leakage;
- Reduction of adhesion strength;
- Stress caused by hygroscopic swelling (and shrinkage in desorption);
- Crack, delamination, and even popcorning phenomenon in reflow soldering.

Reliability issues during reflow are critical for molded packages. The most notorious type of failure in reflow is “popcorning” (Figure 3-1). The package absorbs moisture when it is exposed to the environment. At the start of reflow, the vapor pressure rapidly increases because of the increase in temperature, with the initiation of crack and/or delamination. With the continuous increase in temperature, crack may propagate and may cause

package bulge; finally, large cracks may be observed in the package with the release of vapor. The sound that occurs during the fracturing of the package is similar to that of making pop-corns.

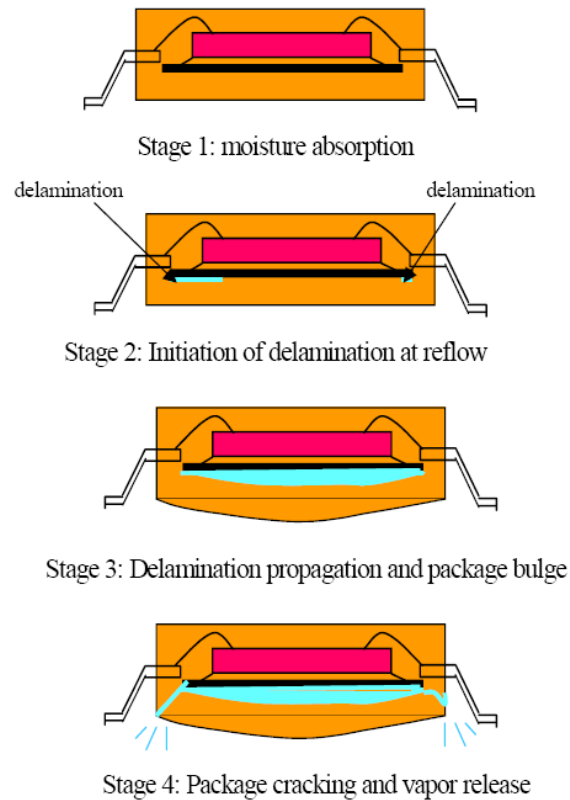


Figure 3-1 Schematic of “pop-corning” occurring at reflow [2]

Different packages may exhibit different sensitivity to moisture, because of the difference in structure, material, and process. The JEDEC³ and IPC⁴ have set industrial standards for the sensitivity levels of moisture for reflow soldering. The products need to be tested for

³ JEDEC is the abbreviation for the JEDEC (Joint Electron Device Engineering Council) Solid State Technology Association.

⁴ IPC represents the Association Connecting Electronics Industries, formerly known as Institute for Printed Circuits and Institute for Interconnecting and Packaging Electronic Circuits.

determining the moisture sensitivity level, and the corresponding storage and handling conditions have to be followed to ensure that the part does not fail by reflow soldering [36].

3.1.1. Hygroscopic Swelling

The absorption of moisture often leads to the volumetric expansion of materials, known as hygroscopic swelling. The coefficient of hygroscopic swelling (CHS) is a measure of the changes of the size of an object with a change in the moisture content:

$$\beta = \frac{\varepsilon_h}{C} \quad (3.1)$$

where ε_h is the hygroscopic strain, and C is the moisture concentration. Notably, the units for hygroscopic strain and moisture contents may vary in different studies. For example, certain studies have typically utilized percent and weight percentage to represent strain and moisture contents, respectively. Thus, it is imperative to ensure the compatibility of the units in the analysis.

3.2. Mathematical Model for Moisture Diffusion

3.2.1. Fick's Law

The most common mathematical model used to express the diffusion of moisture is Fick's Law [37]. Generally, the diffusion flux vector J can be described as

$$J = -D_x \frac{\partial C}{\partial x} - D_y \frac{\partial C}{\partial y} - D_z \frac{\partial C}{\partial z} \quad (3.2)$$

Some studies use matrix notation, in which case, this equation can be expressed as

$$\{J\} = -[D]\nabla C \quad (3.3)$$

where

$\{J\} = \{J_x \ J_y \ J_z\}^T$ is the diffusion flux vector;

$$[D] = \begin{bmatrix} D_x & 0 & 0 \\ 0 & D_y & 0 \\ 0 & 0 & D_z \end{bmatrix} \text{ is the diffusion matrix, and}$$

D_x , D_y , and D_z represent the diffusivities in the x, y, and z-direction, respectively;

$C(x, y, z, t)$ is the concentration of the diffusing substance (moisture);

$$\nabla = \left\{ \frac{\partial}{\partial x} \quad \frac{\partial}{\partial y} \quad \frac{\partial}{\partial z} \right\}^T \text{ is the gradient operator.}$$

Besides, diffusion is also governed by the conservation of mass:

$$\left(\frac{\partial J_x}{\partial x} + \frac{\partial J_y}{\partial y} + \frac{\partial J_z}{\partial z} \right) + \frac{\partial C}{\partial t} = r \quad (3.4)$$

where

t is time, and

r is the rate of generation of the diffusing substance per volume. For all the cases discussed in this dissertation, $r = 0$.

If the matrix notation is used, the conservation of mass is expressed as

$$\nabla \cdot \{J\} + \frac{\partial C}{\partial t} = r \quad (3.5)$$

where $\nabla \cdot$ is the divergence operator.

Combining Eq. (3.2) with Eq. (3.4) and letting $r = 0$, we have

$$\frac{\partial C}{\partial t} = \frac{\partial}{\partial x} \left(D_x \frac{\partial C}{\partial x} \right) + \frac{\partial}{\partial y} \left(D_y \frac{\partial C}{\partial y} \right) + \frac{\partial}{\partial z} \left(D_z \frac{\partial C}{\partial z} \right) \quad (3.6)$$

which is known as Fick's second law. For isotropic materials, this equation can be simplified to

$$\frac{\partial C}{\partial t} = D \left(\frac{\partial^2 C}{\partial x^2} + \frac{\partial^2 C}{\partial y^2} + \frac{\partial^2 C}{\partial z^2} \right) \quad (3.7)$$

3.2.2. Discontinuity of Concentration at the Material Interface

For each material, a maximum amount of moisture can be absorbed under certain conditions, known as saturation. Because the saturated moisture concentration is dependent on material, the concentration at the material interface is discontinuous (Figure 3-2). At a given temperature, the concentration of moisture at the material interface follows Nernst distribution:

$$\chi = \frac{C_{Mat1}}{C_{Mat2}} = \frac{C_{sat1}}{C_{sat2}} = \text{const} \quad (3.8)$$

where C_{Mat1} and C_{Mat2} represent the concentrations of the two materials at the interface, and C_{sat1} and C_{sat2} represent their saturated concentrations.

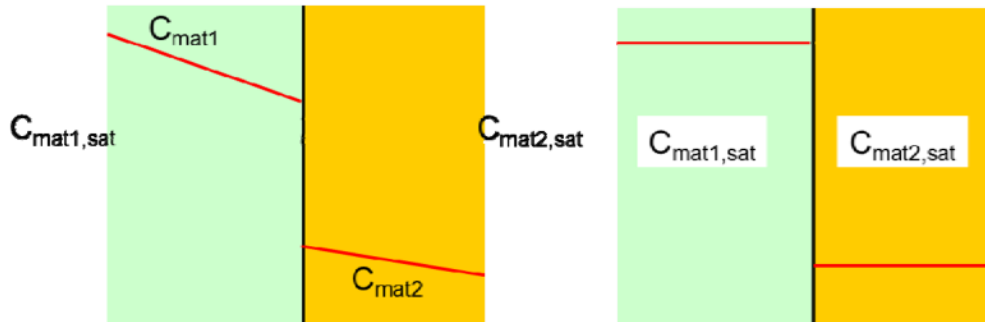


Figure 3-2 Concentration of moisture across the bimaterial boundary [2]

3.3. Finite Element Modeling of Diffusion Behavior⁵

3.3.1. Analogy Method

Two tasks must be accomplished for accurately simulating the diffusion of moisture in a system containing two or more materials. The first task is to numerically implement diffusion equations, and the second task is to appropriately handle the moisture concentration and flow at the interface of the two materials. Prior to the release of ANSYS 14, a widely used method adopted by ANSYS users to fulfill the first task was to employ thermal analogy, based on the similarity of the governing equations of heat transfer and moisture diffusion [38, 39]. For heat transfer, the diffusion equation gives

$$\rho c_p \dot{T} = \nabla \cdot (k \nabla T) \quad (3.9)$$

where q represents the heat flux, T represents the temperature, ρ represents the density, c_p represents the specific heat, and k represents the thermal conductivity. For the diffusion of moisture, the Fick's second law gives

$$\dot{C} = \nabla \cdot (D \nabla C) \quad (3.10)$$

which is the vector notation of Eq. (3.6). The similarity between Eq. (3.9) and Eq. (3.10) is clear; hence, a direct analogy can be easily formulated [38]. For ANSYS 14 and 14.5, the diffusion of moisture can be directly simulated using corresponding elements, and

⁵ Sub-sec. 3.3.1 and 3.3.2 have been reused, with permission, from Liu, D. and Park, S., 2014, "A Note on the Normalized Approach to Simulating Moisture Diffusion in a Multimaterial System Under Transient Thermal Conditions Using ANSYS 14 and 14.5," J. of Electronic Packaging, 134, p. 034501. Copyright © 2014 ASME.

coupled-field simulations with heat transfer and structural analyses can be simultaneously achieved [33, 40].

The second issue is typically handled using a normalized approach. If we recall Eq. (3.8),

$$\frac{C_{Mat1}}{C_{Mat2}} = \frac{C_{sat1}}{C_{sat2}}$$

we observe that discontinuity can be handled by the introduction of a normalized field variable

$$w = C/C_{sat} \quad (3.11)$$

Because $C_{sat} = SP_v$, where S is the solubility, and P_v is the ambient vapor pressure of the environment, an alternative is to define

$$\phi = C/S \quad (3.12)$$

as the normalized concentration, and in this case, the ambient vapor pressure P_v is treated as a boundary condition. By substituting the concentration C with $S\phi$ in Eq. (3.10), Fick's law in terms of normalized concentration yields

$$\dot{S}\phi + S\dot{\phi} = \nabla \cdot [D\nabla(S\phi)] \quad (3.13)$$

From a practical viewpoint, for most problems in packaging, the effect of the spatial temperature gradient can be neglected, and solubility for each material can be considered to be uniform as the spatial temperature difference is typically marginal to affect the

diffusion parameters in this particular research area. Based on this assumption, the diffusion equation for each material can be simplified as

$$\dot{S}\phi + S\dot{\phi} = \nabla \cdot (DS\nabla\phi) \quad (3.14)$$

Similarly, if another normalization method is adopted (such as using saturated concentration C_{sat}), Eqs. (3.13) and (3.14) will still hold, except that the solubility S will be replaced by the corresponding material property.

Solubility can be expressed as

$$S = S_0 \exp\left(\frac{E_s}{RT}\right) \quad (3.15)$$

where E_s is the activation energy for solubility, S_0 is a material property, and R is the gas constant. Clearly, $\dot{S} = 0$ under isothermal conditions (temporally and spatially, i.e., $\dot{T} = 0$ and $\nabla T = 0$); hence, Eq. (3.14) can be rewritten as

$$S\dot{\phi} = \nabla \cdot (DS\nabla\phi) \quad (3.16)$$

Another analogy scheme, referred to as the “normalized analogy,” can be formulated based on Eq. (3.9) and Eq. (3.16). This approach is suitable for solving diffusion problems issues in multi-material systems under isothermal conditions, for example, the ingress of moisture into electronic components encapsulated by the molding compound in the 85 °C / 85% RH (85/85) or highly accelerated stress test (HAST) test. However, this normalization method can give incorrect results under transient thermal conditions ($\dot{T} \neq 0$), or more general, temporally and spatially anisothermal conditions ($\dot{T} \neq 0$ and

$\nabla T \neq 0$) [38, 39, 41]. For transient thermal conditions, as solubility is a function of temperature, and ultimately a function of time, dropping the term $\dot{S}\phi$ would lead to erroneous results; unfortunately, this is the limitation of normalized analogy. The same issue arises if we normalize the moisture concentration with respect to the saturated concentration instead of solubility. For the saturated concentration,

$$C_{sat} = SP_v = S \times P_{sat} \times RH \quad (3.17)$$

and

$$P_{sat} = P_0 \exp\left(-\frac{E_{VP}}{RT}\right) \quad (3.18)$$

where P_{sat} represents the saturated vapor pressure, RH represents the relative humidity, E_{VP} represents the activation energy for vapor pressure, and P_0 is a constant. Hence,

$$C_{sat} = S_0 P_0 \exp\left(\frac{E_s - E_{VP}}{RT}\right) \times RH \quad (3.19)$$

Clearly, there is no guarantee that C_{sat} is independent of time; hence, conducting normalization with respect to C_{sat} is not suitable for transient thermal conditions, either. In other words, there is no way to further simplify Eq. (3.14) under transient thermal conditions unless the normalized concentration can be defined as concentration divided by a time- and temperature-independent material property. Based on the results of experimental measurement, that is $E_s \approx E_{VP}$ for several electronic packaging materials [42], Jang et al. have defined that property as [39]

$$M = S_0 P_0 \quad (3.20)$$

and defined

$$\varphi = C/M \quad (3.21)$$

as the new normalized concentration. Obviously, M is temperature-independent. Thus, Eq. (3.14) can be simplified to a form similar to Eq. (3.16), with S replaced with M , which is referred to as the “modified solubility.” This analogy scheme is named the “advanced analogy,” and in contrast, the normalization method using the solubility or saturated concentration is referred to as the “conventional” method by Jang et al. The simulation results obtained from the different methods are compared in Ref. [39].

3.3.2. Diffusion Elements and Coupled-Field Elements in ANSYS

ANSYS has adopted a normalized approach in its diffusion elements⁶ (and coupled-field elements with diffusion capability⁷) to handle the discontinuity issue at the material boundaries. The ANSYS Theory Reference provides a governing equation:

$$\frac{\partial(C_{sat}\bar{C})}{\partial t} = C_{sat}[D]\nabla^2\bar{C} \quad (3.22)$$

where $\bar{C} = C/C_{sat}$ is the normalized concentration [33]. This equation, mathematically, has the same form as Eq. (3.14), with the only difference being notation. The “saturated concentration” a material property (MPDATA, CSAT), and the ANSYS parametric

⁶ PLANE238, SOLID239, and SOLID240 (ver. 14.5 or later)

⁷ PLANE223, SOLID226, and SOLID227 (ver. 14 or later)

design language (APDL) allows this property to be input as temperature-dependent [33]⁸. Apparently, other normalization methods can be implemented by simply inputting the corresponding properties (such as solubility S or modified solubility M) as the “CSAT” property in the material model.

Equation (3.22) is obviously correct; however, the method of handling this equation may lead to incorrect results. If the “saturated concentration” (CSAT) is simply updated in a stepwise manner, the effect of the rate change (\dot{C}_{sat} or \dot{S}) will not be included in the calculation, repeating erroneous results as in the analogy method.

However, there is no example of temperature-dependent saturation in the documentation of ANSYS. Therefore, we performed a case study using the identical transient thermal problem as in Ref. [39]. Figure 3-3 shows the model geometry. As for the material properties, the solubility–temperature relation is assumed to have the form as in Eq. (3.15), and diffusivity–temperature is assumed to follow the Arrhenius equation:

$$D = D_0 \exp\left(-\frac{E_D}{RT}\right) \quad (3.23)$$

where E_D is the activation energy for diffusivity, which is dependent on material, and D_0 is a material-dependent constant.

⁸ The reference manual of ANSYS 15 states that CSAT must not be dependent on temperature. However, the APDL (ANSYS Parametric Design Language) and ANSYS GUI do permit such a method of input.

Table 3-1 summarizes the material properties. The temperature increased 1 °C per minute from room temperature, while the vapor pressure was set at 3207 Pa (saturated vapor pressure at 25 °C) and maintained constant during heating.

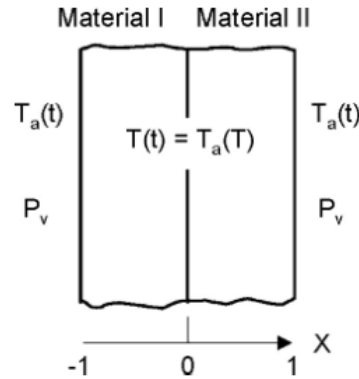


Figure 3-3 Geometry and boundary conditions for the case study
 $(T_a = 25 + t/60 \text{ } ^\circ\text{C}, P_v = 3207 \text{ Pa})$

Table 3-1 Material properties for analysis cases

	Material 1	Material 2
$D_0(\text{m}^2 \text{ s}^{-1})$	5×10^{-3}	4×10^{-3}
$S_0(\text{kg m}^{-3} \text{ Pa}^{-1})$	6×10^{-10}	2×10^{-10}
$E_D(\text{J mol}^{-1})$	5×10^4	5×10^4
$E_S(\text{J mol}^{-1})$	4×10^4	4×10^4

Two normalization methods were compared: one is a “conventional” normalization method with respect to the solubility S , and the other is the advanced normalization approach. For the latter case, a temperature-dependent boundary condition should be applied [39]:

$$\varphi_{BC}(t) = \frac{C(t)}{M} = \frac{S(t)P_v}{M} = \frac{S_0P_v}{M} \exp\left[\frac{E_s}{RT(t)}\right] \quad (3.24)$$

An eight-node diffusion element (PLANE238) was used for the finite element simulation. A program written using the finite difference method (FDM) was also used for verification, and the algorithm is described in detail in Ref. [38].

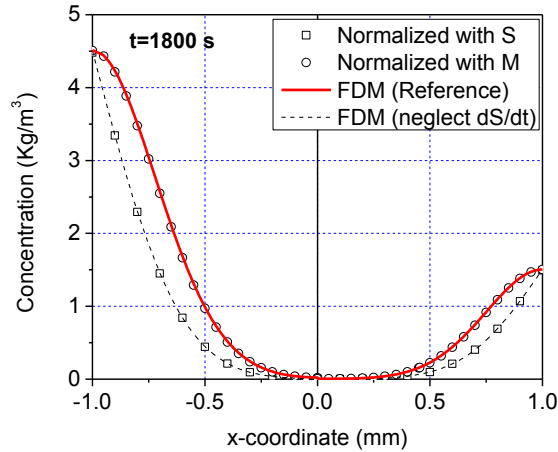


Figure 3-4 Moisture concentration in a bimaterial specimen subject to the transient thermal condition ($t = 1800$ s)

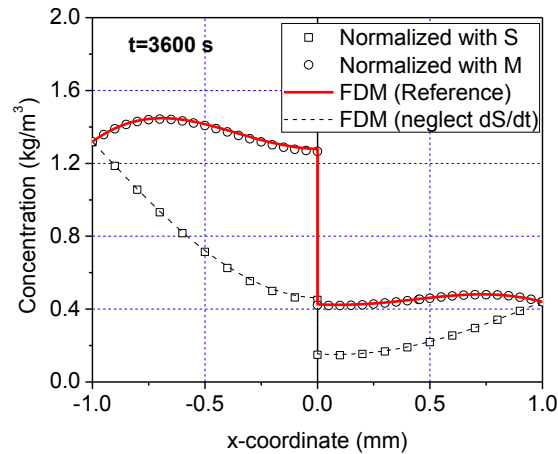


Figure 3-5 Moisture concentration in a bimaterial specimen subject to the transient thermal condition ($t = 3600$ s)

Figures 3-4 and 3-5 show the simulation results; different normalization methods clearly gave different values. The results from the “conventional” normalization method significantly deviate from the reference values. Actually, the incorrect results in Fig. 5 of

Ref. [39] are regenerated. The normalized approach using modified solubility (M) gives the same results as the FDM calculation, and the values agree with prior simulation results in Ref. [39].

For illustrating the root of the erroneous results, we forced \dot{S} to be zero in the FDM program to intentionally generate a “wrong” solution, and the data perfectly matched the incorrect FEM results. Clearly, the effect of the rate of change of the “CSAT” property was omitted by the program; therefore, the “saturated concentration” property in ANSYS (MPDATA, CSAT) must not be temperature-dependent for simulations under transient thermal conditions; otherwise, the result would be inaccurate. As a result, performing simulation under such conditions becomes very tricky. A more complicated “truly anisothermal” case ($\dot{T} \neq 0$ and $\nabla T \neq 0$) is not covered in this paper as the conclusion will be evident [39].

3.3.2.1. Summary and Discussion on ANSYS Diffusion Elements

Our case study has indicated that for a multi-material system under transient thermal conditions, the simulation result using current versions of ANSYS is dependent on the normalization method. The newly developed diffusion elements behave in a manner similar to thermal elements; however, there are apparent differences between the transient thermal and moisture diffusion simulations. For the thermal analysis of solid materials, the temperature dependency of density ρ and specific heat c_p could be very weak; however, for moisture diffusion analysis, solubility changes exponentially with

temperature. Using a temperature-dependent material property for normalization will lead to erroneous results in moisture diffusion analysis. Although the analogy method is no longer needed for ANSYS users after the release of version 14, the accumulated knowledge about normalization methods is still valuable.

3.3.3. The Direct Concentration Approach

As shown in subsection 3.3.1, Jang's normalized approach is derived from the approximate equivalence of the activation energy for vapor pressure and solubility, and M_1 , M_2 and their ratio are constants. Although this is applicable for a wide range of applications, such an approximation is not universally applicable. For example, the E_s value becomes different if the temperature is higher than T_g [41], and the ratio of moisture concentration at the two sides of the interface is not always a constant. Therefore, it is promising to develop a method that does not rely on such a relation, which will have a potentially larger field of application than the advanced normalized approach. In 2009, Xie et al. have reported their direct concentration approach (DCA) [41]. The DCA has been implemented using ABAQUS for investigating moisture-related issues during reflow [43].

The following points are required for the implementation of the DCA:

1. Using concentration (instead of normalized concentration) in simulation.
2. The material interface consists of two sets of nodes, one for each material.
3. A set of constraint equations are applied to the interfacial nodes to “join” two materials together for a continuity relation. The constraint equation is given by Eq. (3.8);

however, in this case, χ can be dependent on temperature. The authors of Ref. [41] claimed that, by doing so, the continuity equation for diffusion flux,

$$D_1 \frac{\partial C_1}{\partial n} = D_2 \frac{\partial C_2}{\partial n} \quad (3.25)$$

where n is the normal direction of the location at the interface, “will automatically be satisfied through the finite element formulation,” “according to the variational principle.”

Because the ratio of the concentration of two materials at the material boundary can be dependent on temperature, the constraint equation needs to be updated if necessary. Because such capability is not supported by commercial software, a new analysis with an updated constraint equation and moisture distribution obtained from the last step of previous analysis needs to be performed.

3.3.3.2. Examination of the Direct Concentration Approach

Despite more complicated programming caused by the application and update of constraint equations (especially when dealing with a 3D Model), the DCA appears to be promising because of its independence of the solubility (or saturated concentration) of the diffusion substance. However, the DCA gives different results for the same case as in subsection 3.3.2. As shown in Figure 3-6 (a), DCA gives slightly greater concentration values than other approaches. However, this difference is not caused by numerical error and cannot be eliminated. More importantly, we can find that the slope on the left and right side of DCA curve is different if we take a closer look at Figure 3-6 (a), indicating that the diffusion flux is discontinuous across the material interface, which violates the

law of mass conservation. As shown in Figure 3-6 (b), the ratio of the diffusion flux at the interface between material 1 and material 2 ($J_{1R}/J_{2L}|_{x=0}$, where $J_1 = \partial C_1/\partial x$ and $J_2 = \partial C_2/\partial x$) equals 1/3, which is the inverse of the ratio of the solubility (S_1/S_2).

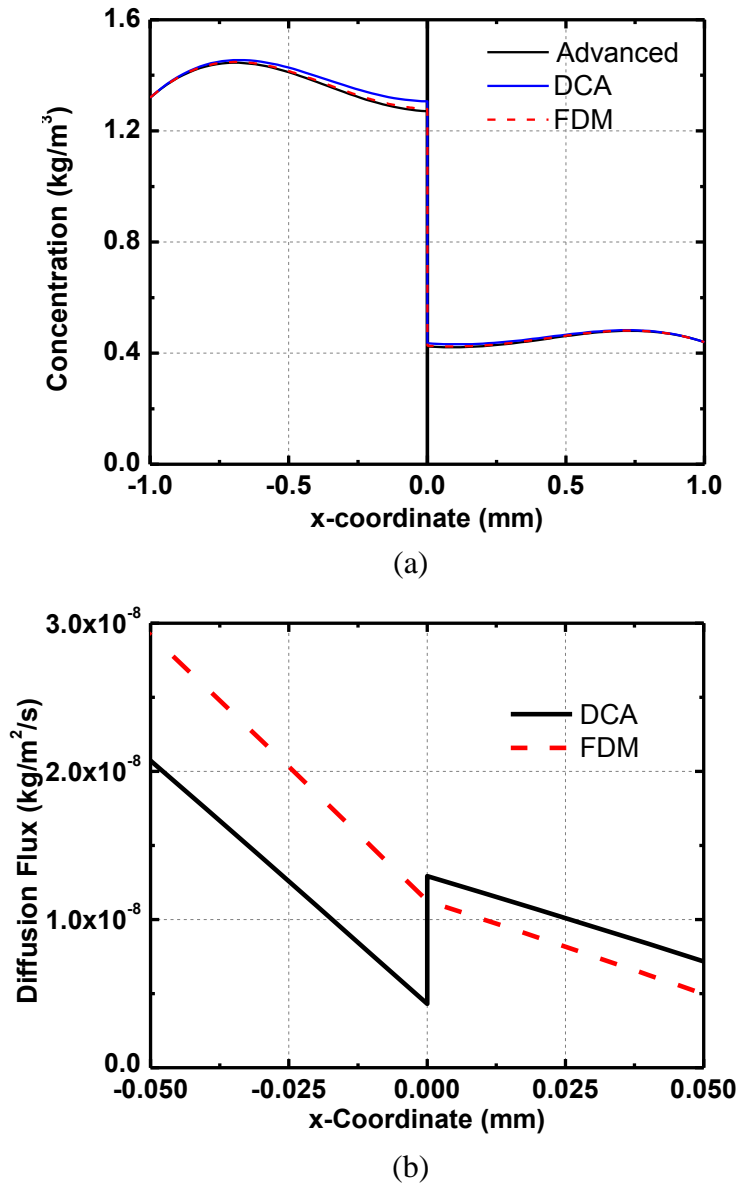


Figure 3-6 Comparison of the moisture concentration (a) and diffusion flux (b) in a bimaterial specimen under the transient thermal condition calculated by the direct concentration approach with finite difference method and/or the normalized approach ($t = 3600$ s)

Frankly, the case in subsection 3.3.2 is not a very good case to show the difference between DCA and the correct approaches because the diffusion flux through the material interface is quite limited; hence, the subtle difference of flux is too difficult to be observed. A better case is to use a sandwich structure with two materials (Figure 3-7). The left and right portions have the same material, and the middle portion is made of another material. Assuming that the length of the left, middle, and right portions is 1 mm, 2 mm, and 1 mm, respectively, the moisture ingresses into the assembly from both the left and right sides (but not top and bottom). This model can be reduced to the one in Figure 3-3 using symmetry, with the only difference on the boundary and loading conditions. To simplify the simulation setup, the temperature is set as a constant value of 85 °C. The vapor pressure remains the same as that in Figure 3-3. After the thermal condition is set up, the only change that we need to make is to remove the diffusion boundary condition at the right end of Figure 3-3, because the software will automatically assume that the flux at this surface equals zero by default.

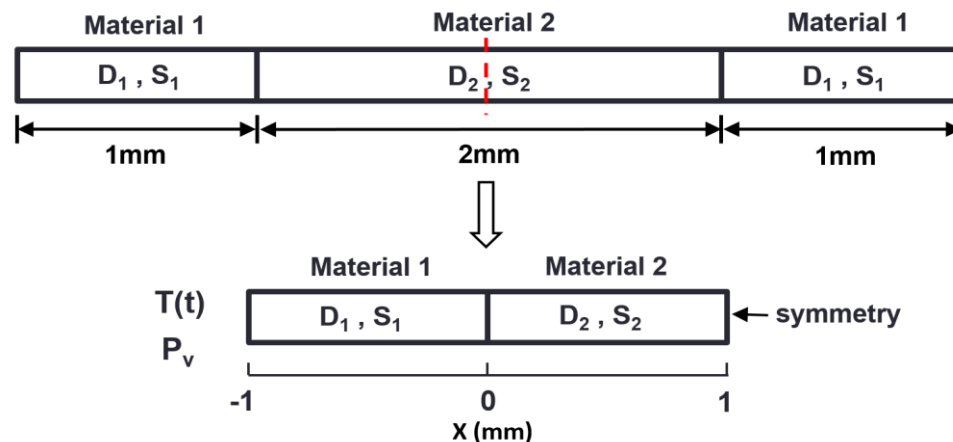


Figure 3-7 Sandwich structure with two materials (infinite length in the vertical direction)

For this new case, all moisture absorbed by material 2 needs to travel through the material interface; hence, it is suitable to contrast the difference. Figure 3-8 and Figure 3-9 plot the moisture distribution and diffusion flux of the left half of the sandwich assembly, respectively, with the origin at the material interface. The DCA clearly leads to discontinuous flux at the interface, implying that a wrong solution is obtained.

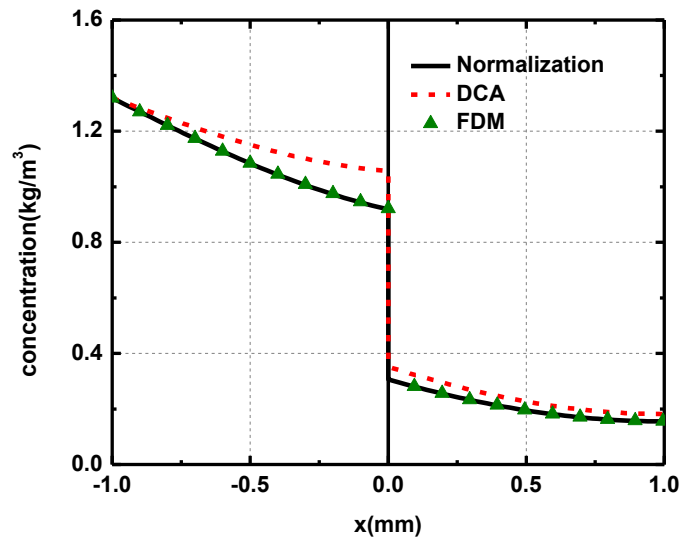


Figure 3-8 Concentration of moisture on the left half of the sandwich structure

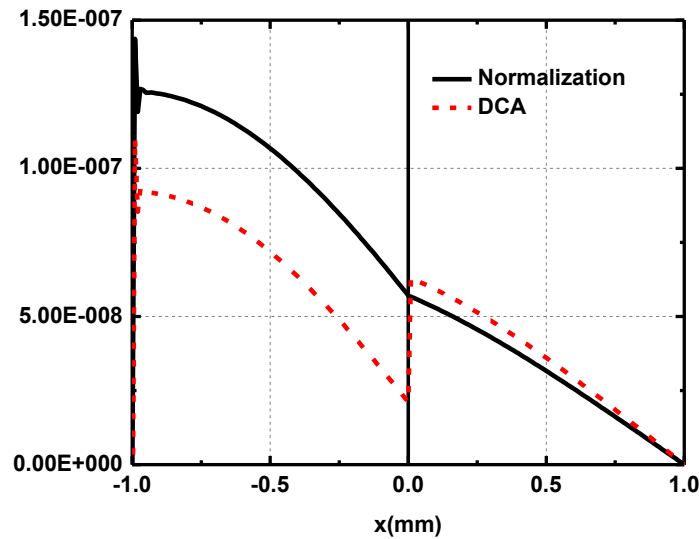


Figure 3-9 Diffusion flux on the left half of the sandwich structure

The discontinuity of flux using DCA occurs during the implementation of the constraint equations in finite element simulation, which can be proved using the theory of finite element methods. To simplify the derivation, we consider a one-dimensional (1D) model with bar elements, and each element has only two nodes.

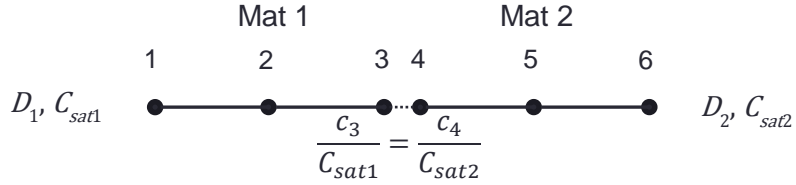


Figure 3-10 Geometry and boundary conditions for finite element analysis

Therefore, the shape function is

$$\{N\} = [1 - x/h \quad x/h]^T \quad (3.26)$$

where h is the length of the element. Therefore, the concentration over the element can be expressed as

$$C = \{N\}^T \{C_e\} \quad (3.27)$$

where $\{C_e\}$ is the nodal concentration vector.

The governing equation for diffusion in the finite element method can be derived by the Galerkin method as

$$[K^d]\{C_e\} + [C^d]\{\dot{C}_e\} = \{R_e\} \quad (3.28)$$

where $[K^d]$ is the diffusion conductivity matrix, $[C^d]$ is the diffusion damping matrix, and $\{R_e\}$ is the combination of element diffusion flux, applied flow rate, and generation

of diffusion substances. For moisture diffusion studied in this dissertation, there is no generation of moisture. Besides, no specified flow rate is applied to the material interface.

The diffusion conductivity matrix can be derived as

$$[K^d] = C_{sat} \int_0^h (\nabla\{N\}^T)^T [D] (\nabla\{N\}^T) dx \quad (3.29)$$

The value of C_{sat} will be assigned as 1 if direct concentration is used. In this case, for 1D 2-node element, the equation above yields

$$[K^d] = \frac{1}{h} \begin{bmatrix} D & -D \\ -D & D \end{bmatrix} \quad (3.30)$$

We assume that both material 1 and material 2 have the same number of elements and that the length of each element is the same. To reduce the amount of work in writing the matrix, we only consider a finite element model with four elements, two for each material. Assuming that at the material interface, each material has its own node (i.e., they are not sharing the common node), there will be a total of six nodes in the model. The diffusion conductivity matrix after the assembly process becomes

$$[K^d] = \frac{1}{h} \begin{bmatrix} D_1 & -D_1 & & & & \\ -D_1 & 2D_1 & -D_1 & & & \\ & -D_1 & D_1 & & & \\ & & & D_2 & -D_2 & \\ & & & -D_2 & 2D_2 & -D_2 \\ & & & & -D_2 & D_2 \end{bmatrix} \quad (3.31)$$

where all blanks are zero.

For transient analysis, the element diffusion damping matrix is

$$[C^d] = C_{Sat} \int_0^h \{N\} \{N\}^T dx \quad (3.32)$$

Hence,

$$[C^d] = \frac{h}{6} \begin{bmatrix} 2 & 1 \\ 1 & 2 \end{bmatrix} \quad (3.33)$$

and after assembly, this matrix becomes

$$[C^d] = \frac{h}{6} \begin{bmatrix} 2 & 1 & & & & \\ 1 & 4 & 1 & & & \\ & 1 & 2 & & & \\ & & & 2 & 1 & \\ & & & 1 & 4 & 1 \\ & & & & 1 & 2 \end{bmatrix} \quad (3.34)$$

If no constraint equation is applied to the nodes at material interface, we can easily write the equations at the material interfaces by expanding the matrix multiplication and rearranging the items. For the material 1 on the left, it yields

$$\left(\frac{D_1 \frac{(c_3 - c_2)}{h} - R_3}{h} \right) + \frac{1}{6} (c_2 + 2c_3) = 0 \quad (3.35)$$

where c_i is the i_{th} element of the vector $\{C_e\}$, and R_i is the i^{th} element of the vector $\{R_e\}$.

The first item in this equation corresponds to $\partial J / \partial x$, and the second item corresponds to $\partial C / \partial t$ of Eq. (3.4). Therefore, we can further say $J_{1R} = -R_3$ and $J_{1L} = -D_1 \frac{(c_3 - c_2)}{h}$;

hence, the equation yields

$$\frac{J_{1R} - J_{1L}}{h} + \left(\frac{\partial C_{Mat1}}{\partial t} \right)_{x=0} = 0 \quad (3.36)$$

The equation on the other side can be expressed in the same manner:

$$\left(\frac{-D_2 \frac{(c_5 - c_4)}{h} - R_4}{h} \right) + \frac{1}{6} (\dot{c}_5 + 2\dot{c}_4) = 0 \quad (3.37)$$

Similarly, for this case, letting $J_{2L} = R_4$ and $J_{2R} = -D_2 \frac{(c_5 - c_4)}{h}$, we can get

$$\frac{J_{2R} - J_{2L}}{h} + \left(\frac{\partial C_{Mat1}}{\partial t} \right)_{x=0} = 0 \quad (3.38)$$

By default, $R_3 = R_4 = 0$ if no boundary condition is applied.

In the DCA, the constraint equation is applied so that the nodes at the interface will have the relation $c_3 = \chi c_4$. There are three ways to implement this relation in FEM, namely, master–slave elimination, penalty augmentation, and Lagrange multiplier adjunction. In this dissertation, the master–slave method is used.

For master–slave elimination, the degree-of-freedom (DOF) to be eliminated is the slave DOF, and the remaining one is the master DOF. Therefore, a new set of DOFs $\{\widehat{C}_e\}$ will be established after the elimination of the slave DOF from the original set of DOF $\{C_e\}$.

The old and new sets of DOF are related by a transformation matrix:

$$\{C_e\} = [T]\{\widehat{C}_e\} \quad (3.39)$$

In this case, if c_3 was chosen as the slave DOF, this equation above shall be

$$\begin{Bmatrix} c_1 \\ c_2 \\ c_3 \\ c_4 \\ c_5 \\ c_6 \end{Bmatrix} = \begin{bmatrix} 1 & & & & & \\ & 1 & & & & \\ & & \chi & & & \\ & & 1 & & & \\ & & & 1 & & \\ & & & & 1 & \end{bmatrix} \begin{Bmatrix} c_1 \\ c_2 \\ c_4 \\ c_5 \\ c_6 \end{Bmatrix} \quad (3.40)$$

Because the χ value remains constant in finite element analysis, and $c_3 = \chi c_4$ is always satisfied, it is easy to find that $\dot{c}_3 = \chi \dot{c}_4$. Hence, the same transformation matrix also relates the derivative matrix

$$\{\dot{C}_e\} = [T] \{\widehat{C}_e\} \quad (3.41)$$

Replacing Eq. (3.39) and (3.41) into Eq. (3.28) and pre-multiplying with $[T]^T$, we get

$$[T]^T [K^d] [T] \{\widehat{C}_e\} + [T]^T [C^d] [T] \{\widehat{C}_e\} = [T]^T \{R_e\} \quad (3.42)$$

Letting $[\widehat{K}^d] = [T]^T [K^d] [T]$, $[\widehat{C}^d] = [T]^T [C^d] [T]$, and $\{\widehat{R}_e\} = [T]^T \{R_e\}$, the equation above becomes

$$[\widehat{K}^d] \{\widehat{C}_e\} + [\widehat{C}^d] \{\widehat{C}_e\} = \{\widehat{R}_e\} \quad (3.43)$$

After this transformation, the new diffusion conductivity matrix becomes

side equals J_{2L}/h , where J_{1R} is the flux at the right boundary (material interface) of material 1, and J_{2L} is the flux at the left boundary of material 2. Clearly, for $C_{sat1}/C_{sat2} = \chi$, we can always $J_{1R} = J_{2L}/\chi$ if the DCA is used. This numerical relation is independent of diffusivity and boundary conditions.

For steady-state analysis, $\{\dot{C}_e\}$ equals zero, and it is significantly easier to calculate the concentration at this condition. By dropping all the \dot{c}_i terms, Eq. (3.46) becomes

$$-\chi D_1 \frac{c_3 - c_2}{h} = -D_2 \frac{c_5 - c_4}{h} = J_{\text{const}} \quad (3.47)$$

The diffusion flux at each material is a constant. If the concentration at the left-most and right-most point of this four-element assembly has fixed c_L and c_R values, we may get

$$c_L = \chi c_4 + \frac{2h J_{\text{const}}}{\chi D_1} \quad (3.48)$$

$$c_R = c_4 - \frac{2h J_{\text{const}}}{D_2}$$

In a realistic situation, the concentration at the boundary is given in Eq. (3.17). Considering that the sizes of the electronic packages are small, the temperature and humidity around the sample can be treated as uniform. Therefore, we have $c_L/c_R = \chi$. Hence, it is easy to get $J_{\text{const}} = 0$. In this special situation, diffusion is indeed continuous; however, the DCA should be developed for transient analysis in multi-material structures; unfortunately, the DCA approach does not work properly under transient conditions.

As for the simulation cases in Ref. [41], the diffusivity, saturated concentration, and solubility of material 1 is 1000 times (or even more) of material 2. Hence, the flux through the material interface is expected to be very small, and the discontinuity issue can barely be observed.

In summary, using the DCA as described in Ref. [41] will lead to the discontinuity of diffusion flux at the material interface. This issue originates from the implementation of the constraint equations. Because of the limited time, a simple bimaterial model was used for theoretical proof, but it would be easy to prove that the same conclusion still holds for more a general geometry and meshing. The master–slave elimination method was used to implement the constraint equation, and readers who are interested in computational mechanics or computational heat and mass transfer may work on the penalty and Lagrange multiplier methods.

3.4. Measuring Material Properties for Diffusion Analysis⁹

The diffusivity, CHS, and solubility (or saturated concentration) are important material properties for diffusion analysis; hence, numerous researchers have investigated these properties [2, 42, 44-46]. However, compared with the measurement of Young’s modulus and CTE, the measurement of diffusivity and CHS is time-consuming and not as

⁹ Reused, with permission, from Kim, Y., Liu, D., Lee, H., et al., 2015, “Investigation of Stress in MEMS Sensor Device Due to Hygroscopic and Viscoelastic Behavior of Molding Compound”, IEEE Transactions on Components, Packaging and Manufacturing Technology, **5** (7), pp. 945–955. Copyright © 2015 IEEE.

straightforward. In this section, the measurement methods and procedure are briefly introduced for readers who are not familiar with this area.

3.4.1. Measuring Saturated Concentration and Diffusivity

Usually, samples with cuboid shapes are utilized for measurement because an analytical solution for the weight gain (or weight loss) with respect to time can be obtained for such a geometry. The moisture weight gain and saturated weight gain (in weight percentage) are defined as

$$w(t) = \frac{W(t) - W_{dry}}{W_{dry}} \times 100 \quad (3.49)$$

$$w_{sat} = \frac{W_{sat} - W_{dry}}{W_{dry}} \times 100 \quad (3.50)$$

where $W(t)$ represents the instantaneous weight, W_{sat} represents the saturated weight, and W_{dry} represents the dried weight of sample. The concentration of moisture is defined by

$$C(t) = \frac{W(t) - W_{dry}}{V} \quad (3.51)$$

where V is the specimen volume. For the saturated condition, the above equation changes to

$$C_{sat} = \frac{W_{sat} - W_{dry}}{V} \quad (3.52)$$

Obviously, the concentration can be easily related to moisture weight gain using the density of the molding compound.

The analytical solution of Fickian diffusion has been well reviewed in Refs. [44] and Ref. [47]. For moisture loss, the analytical solution of Eq. (3.7) is

$$\frac{W(t)}{W_{sat}} = \frac{512}{\pi^6} \sum_{l=0}^{\infty} \sum_{m=0}^{\infty} \sum_{n=0}^{\infty} \frac{\exp\left(\frac{-Dt}{L_{eqv}^2}\right)}{(2l+1)^2(2m+1)^2(2n+1)^2} \quad (3.53)$$

where

$$L_{eqv}^2 = \left\{ \left[\frac{(2l+1)\pi}{x_0} \right]^2 + \left[\frac{(2m+1)\pi}{y_0} \right]^2 + \left[\frac{(2n+1)\pi}{z_0} \right]^2 \right\}^{-1} \quad (3.54)$$

where L_{eqv} is an equivalent length scale, x_0 , y_0 , z_0 are the length, width, and thickness dimensions, respectively [48]. Diffusivity is determined by the nonlinear regression fit of the experimental data using Eq. (3.53). The relationship between diffusivity and temperature is known to follow the Arrhenius formula, which is expressed as Eq. (3.23).

To determine the saturated condition, molding compound samples need to be dried by baking and placed in an environmental chamber for absorption tests. The weight of samples should be periodically monitored, for instance, using TGA or a high-precision electronic scale until the saturated condition was achieved. Besides, similar to every experimental measurement, it is important to know the precision of the equipment as well as the repeatability of the test method. For example, Figure 3-11 shows the weight gain with respect to time from the absorption test under 85 °C/85%RH, in which four molding

compound samples with the same dimension were measured [49]. The resolution of the scale was 0.01 mg. The error bar in Figure 3-11 indicates good repeatability for this measurement; hence, the number of samples can be reduced in future measurement if the same equipment is used.

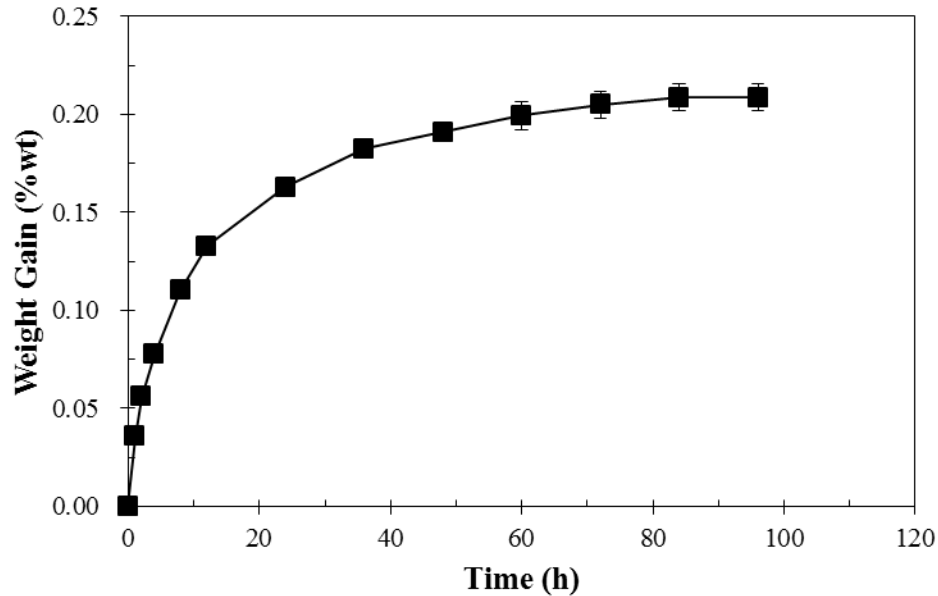


Figure 3-11 Plot of moisture absorption with respect to time [49]

Based on the result shown in Figure 3-11, samples were placed in a chamber with an environment of 85 °C/85%RH for 84 h to achieve saturation. Then, some of them were used for the measurement of moisture diffusivity, while the remaining were utilized for hygroscopic strain measurement. For diffusivity measurement, one sample was measured at each temperature. The specimen was removed from the chamber, placed on a high-precision electronic scale for weight measurement, and placed back into the chamber after measurement. The error caused by such a procedure was found to be negligible [50]. Figure 3-12 shows the experimental data and analytical Fickian fit data. The results

follow the Arrhenius relationship (Eq. (3.23)), with $D_0 = 3039.83083 \text{ mm}^2/\text{s}$ and $E_D = 60884.53465 \text{ J/mol}$.

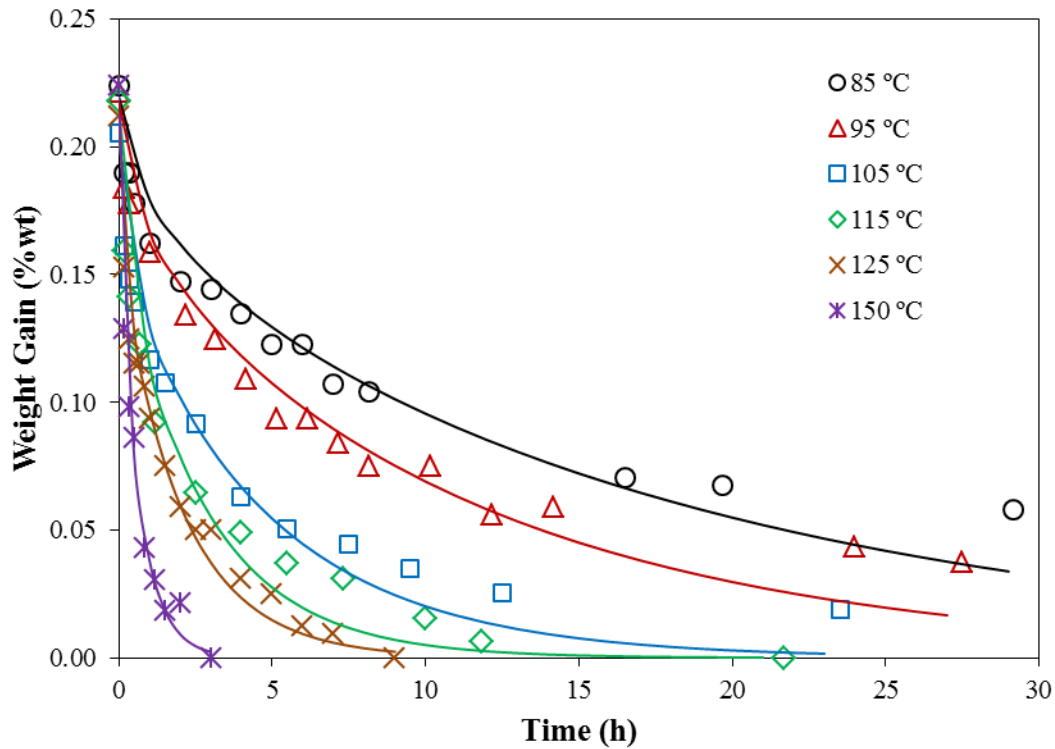


Figure 3-12 Moisture weight gain (bullets) and Fickian curves (lines) of the moisture desorption test under various temperatures [49]

3.4.2. Measuring CHS

Several researchers have measured CHS over a wide temperature range [12, 51-53].

Both moisture concentration and dimension change are needed for calculating the CHS value. The concentration can be measured by an analytical balance or TGA, as discussed in the previous subsection; and the dimension change can be measured using a thermomechanical analyzer (TMA). However, the TMA is based on the probing points (typically, it measures CHS by the dimensional change in the thickness direction because

of the shape of the specimen), while moisture distribution is non-uniform within the specimen. Therefore, the CHS measurement results would be inaccurate if the non-uniformity of moisture distribution is not handled correctly. Zhou has proven that if the hygroscopic strain is only obtained by two-point measurement through the center of the specimen, and if moisture is averaged in the volume, the result would be erroneous. Instead, it is necessary to recalculate the moisture concentration along the local line whose length is measured by TMA. Zhou has confirmed her measurement methodology by finite element simulation [45, 54].

The digital image correlation (DIC), which is a form of photogrammetry, is a non-contact, full-field optical measurement technique in which both in-plane and out-of-plane displacement can be computed by the pictures of the target object at the initial and deformed stages [55]. This is attained by correlating thousands of identical pixels (facets) on the object of measurement, which are considered as strain gauges. The implementation of the DIC technique for CHS measurement has been well established [53, 56]. Unlike other conventional techniques, such as TMA, the full-field deformation of the specimen can be obtained by DIC. Hence, the local strain variation in the sample caused by the spatial property deviation and spatial non-uniformity of moisture can be removed. On the other hand, TMA only measures the deformation in a limited area of the sample where the probe is located, which might result in the misinterpretation of strain. Park [53] and Jang [56] et al. have demonstrated that the DIC technique can be successfully adopted to determine the molding compound CHS. To cope with the initial moisture loss of the sample, Kwak has developed a new DIC measurement setup that eliminates heating [57].

Specimens having identical dimension were placed in preheated chambers. Deformation measurement by DIC and weight loss measurement were performed simultaneously. In this manner, the moisture loss during ramp up temperature can be effectively minimized. Figure 3-13 shows the DIC set up. White speckles were applied on the specimen surface by a spray for generating facets before the specimens were placed in the oven to dry. The saturated specimen was placed in a preheated oven, and the in-plane deformation of its surface was captured. After placing in the preheated chamber, the specimen expanded until it reached isothermal temperature. Then, it started to shrink because of moisture loss. Typically, this shrinkage lasts for 1–2 min, and this initial expansion was not included in CHS calculation. After this initial expansion, the image was captured in a pre-set interval. Then, the hygroscopic strain was calculated by DIC analysis.

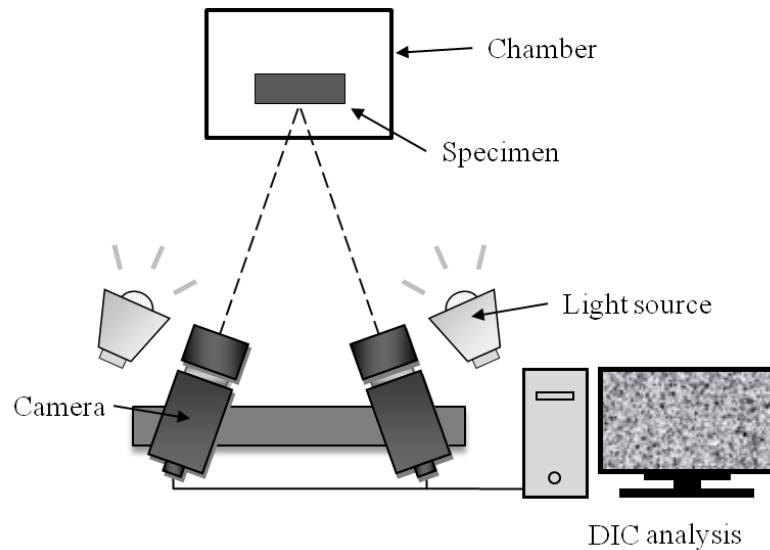


Figure 3-13 Setup of the DIC system [49]

For demonstrating the effect of non-uniformity of moisture concentration and for showing that the DIC-based approach can effectively handle moisture non-uniformity, a “virtual CHS measurement” is performed using FEA. The dimension of the “specimen” is 10 mm by 10 mm by 1.6 mm. Table 3-2 lists the material properties used in the simulation. The specimen is assumed to be saturated at time zero, and CHS is measured during desorption.

Table 3-2 Material properties for “virtual CHS measurement” simulation

Material Property	Value and Unit
Diffusivity (D)	$4.5 \times 10^{-6} \text{ mm}^2/\text{s}$
Input CHS (β)	$0.2 \text{ mm}^3/\text{mg}$ ($0.2 \times 10^{-3} \text{ m}^3/\text{kg}$)
Saturated concentration (CSAT)	$0.0045 \text{ mg}/\text{mm}^3$ ($4.5 \text{ kg}/\text{m}^3$)
Young’s modulus (E)	20 GPa
Poisson’s ratio (ν)	0.3

Four different measurement approaches were compared [58]:

1. Averaged approach I: Thickness–direction strain (w.r.t. the dry state) measured by the probe vs. averaged concentration (w.r.t. dry state)
2. Averaged approach II: thickness–direction strain (w.r.t. saturation) measured by the probe vs. averaged concentration change (w.r.t. saturated state)

3. The approach proposed by Zhou: thickness–direction strain measured by the probe vs. integrating the local hygroscopic concentration through the center of the plate.
4. DIC-based method: averaged length (or width) direction strain by DIC (Figure 3-14) vs. averaged concentration change (w.r.t. first read point). In the numerical implementation, we used 81 equally spaced points in a 1/8 symmetry model for calculating the dimension change and then averaged the results.

Figure 3-15–Figure 3-18 show the strain–concentration curves. Linear regression was used to calculate the CHS (slope). The reference value for calculated CHS is $0.2 \text{ mm}^3/\text{mg}$, which equals the input CHS. Only the results in the first 10 h are considered because most measurements can be finished within this time.

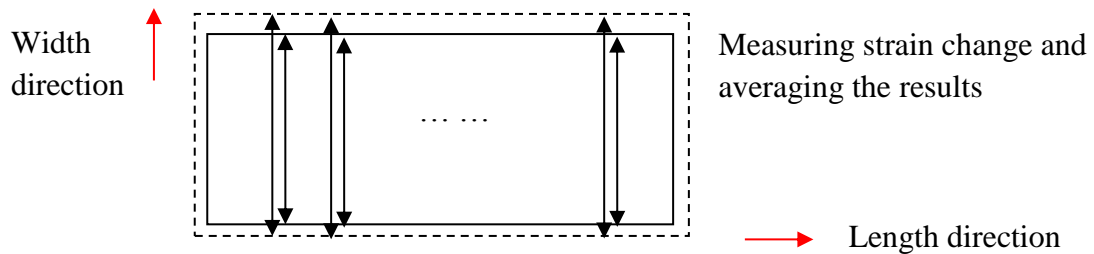


Figure 3-14 Calculation of averaged strain
(Dash lines represent the edge before deformation, while the solid lines represent the edge after shrinkage caused by desorption. Not drawn to scale.)

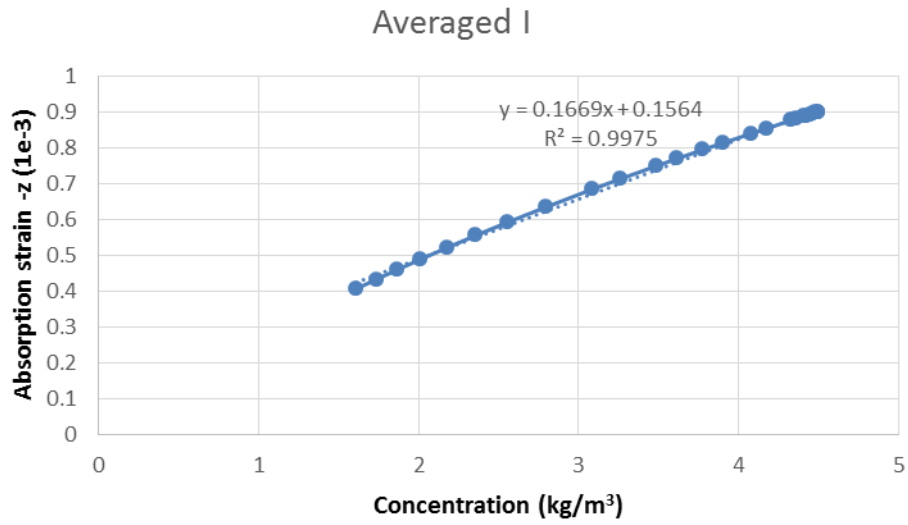


Figure 3-15 Plot of strain versus concentration with the calculated CHS value from linear regression (Averaged approach I)

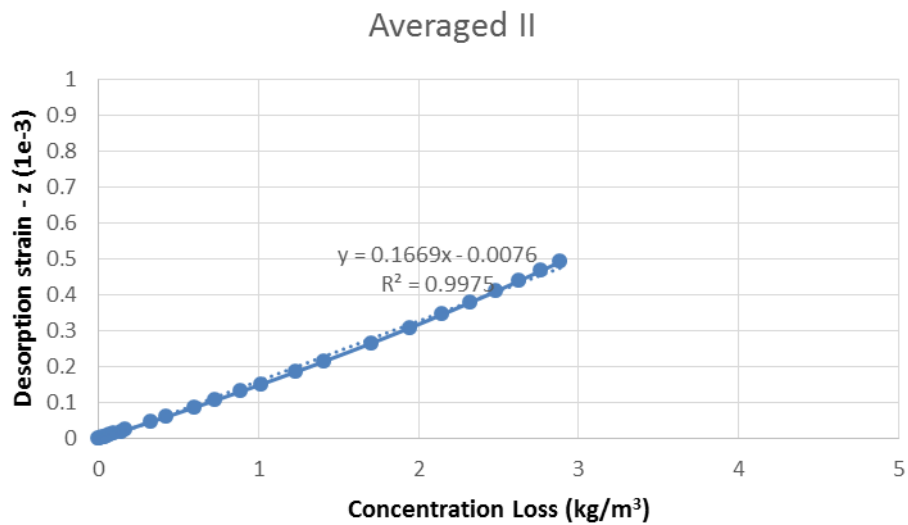


Figure 3-16 Plot of strain versus concentration with the CHS values calculated from linear regression (Averaged approach II)

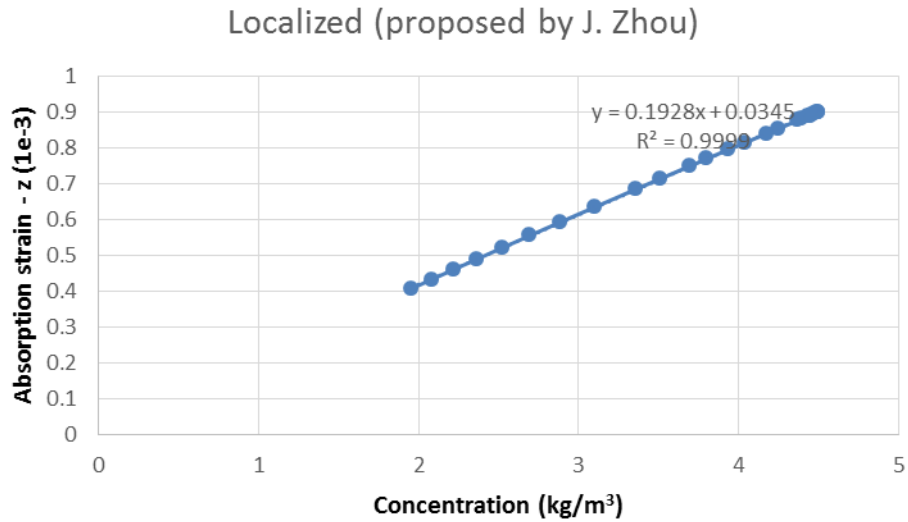


Figure 3-17 Plot of strain versus concentration with the CHS values calculated from linear regression (Local integration)

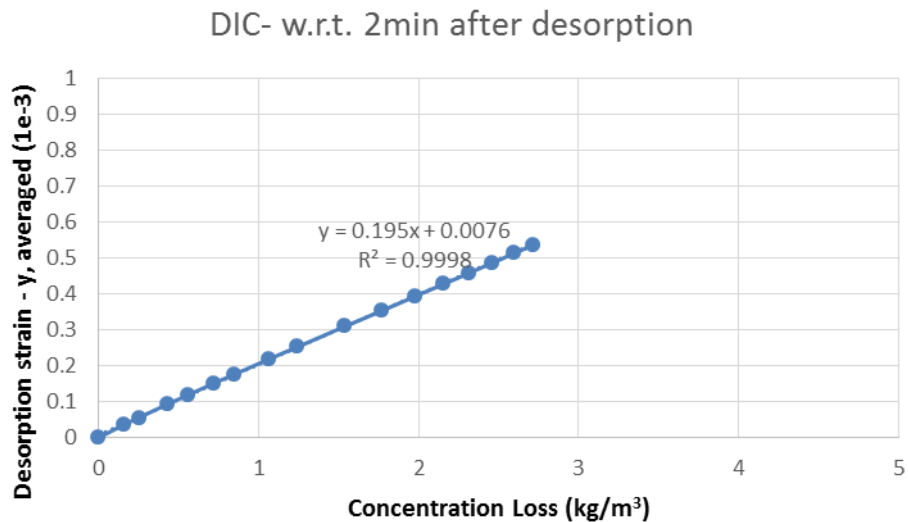


Figure 3-18 Plot of strain versus concentration with the CHS values calculated from linear regression (DIC-based approach)

Clearly, the DIC-based method exhibits theoretical accuracy similar to that obtained from the method proposed by Zhou, and both are more accurate than the “averaged approach.”

Figure 3-18 shows an exemplary plot of hygroscopic strain (measured using DIC) with respect to time during the desorption of moisture. Based on the test results of weight loss and strain measurement, the hygroscopic strain as a function of moisture concentration can be calculated, and Table 3-3 lists the corresponding CHS.

As pointed out by Zhou [58], the real value of CHS can be theoretically calculated by using the dimension change between the dry and saturated conditions. However, this method might be too time-consuming, which implies high cost for TMA-based measurement. Besides, there are only two data points available in the measurement, indicating that the result is possibly erroneous if the concentration or strain at any point is incorrect.

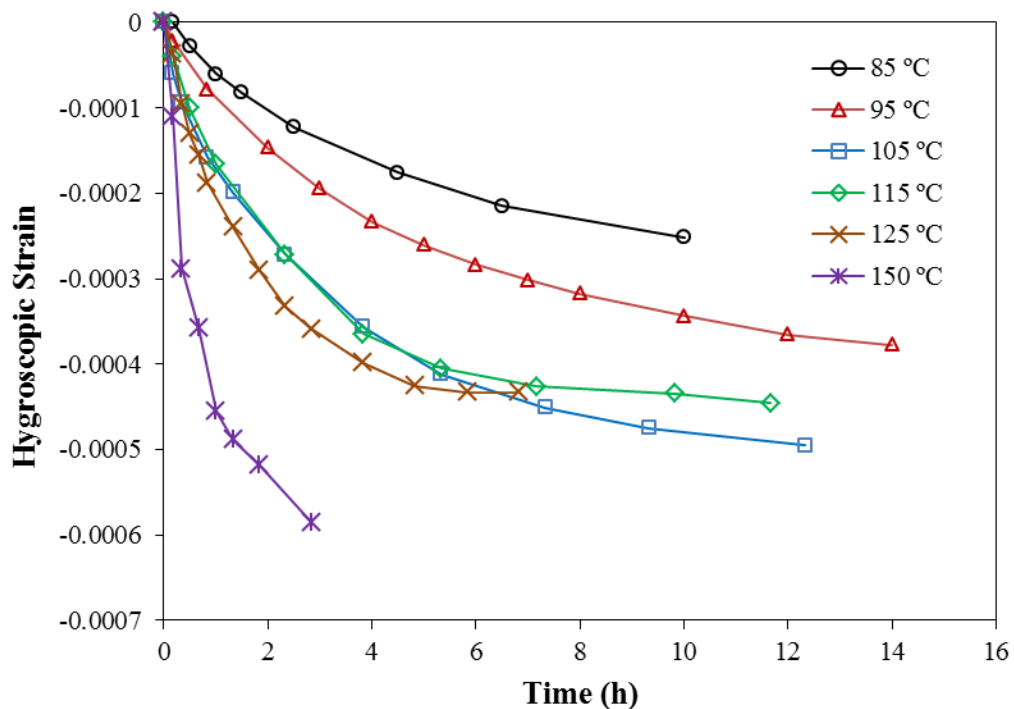


Figure 3-19 Hygroscopic strain at various temperatures [49]

Table 3-3 Diffusivity and CHS values at various temperatures

Temperature (°C)	Diffusivity (mm ² /s)	CHS (mm ³ /mg)
85	3.46E-06	0.133
95	5.28E-06	0.149
105	1.28E-05	0.188
115	2.19E-05	0.163
125	2.95E-05	0.166
150	9.29E-05	0.228

Although the FEA has shown that the DIC-based approach can provide similar theoretical measurement, a small difference is still observed (Figure 3-18). It is possible to eliminate this error by scaling the measurement value by a coefficient, which is ratio of the input and output CHS of the simulation. Such a method has been employed by Zhang [2].

3.5. Summary

This chapter covers the fundamentals of moisture diffusion and its impact on microelectronic reliability. Because different materials exhibit different capability for absorbing moisture, the concentration at the material interface is not continuous. A major part of this chapter is focused on the numerical method for simulating the diffusion of moisture in a multi-material system, and different methods for dealing with the discontinuity of concentration are examined. The direct concentration approach (DCA) that was published by Xie et al. in the Journal of Electronic Packaging is incorrect, and a simplified proof is given using the theory of finite element method. Besides, the experimental methods of measuring the moisture-related material behaviors are introduced and compared.

Chapter 4. Conjugate Problem of Thermomechanical and Hygroscopic Loading with Viscoelastic Material Properties ¹⁰

4.1. Problem Statement

When a MEMS sensor is in use, it is exposed to an environment that imposes both thermal and humidity conditions on the product. Thus, it is necessary to study the comprehensive effect of temperature and moisture. Several experimental tests such as 85/85 (85°C with 85% relative humidity) and highly accelerated stress test (HAST) have been developed for evaluating the reliability of the parts under combined temperature and humidity conditions, and temperature humidity bias (THB) testing has even included electrical bias. Such tests have been widely used in industry and are also taught in classical text books for reliability engineering.

¹⁰ With permission from IEEE, part of this chapter is from Kim, Y., Liu, D., Lee, H., et al., 2015, "Investigation of Stress in MEMS Sensor Device Due to Hygroscopic and Viscoelastic Behavior of Molding Compound", IEEE Transactions on Components, Packaging and Manufacturing Technology, 5 (7), pp. 945 – 955. Copyright © 2015 IEEE. Minor revisions are made to some equations for avoiding the use of symbols, which have been defined in other chapters with different meaning.

Besides, there are some differences between the warpage data in the "Validation Simulation" section of this dissertation and the data in the published paper because of the following reasons: a) The curves representing 25 °C are removed, because the relative warpage with respect to itself always gives zero. b) In the paper published previously, the length of the diagonal for simulation is longer than that of measurement because of the slight difference in geometry and if data points at the end of diagonal line can be obtained by the DIC. In this paper, the curves are re-aligned so that the center of the curves are the same; then, the start and end portion of the simulation data are trimmed so that the length along the abscissa for both curves will be the same. The deformation data are also reset accordingly so the deformation at the end points will be zero. c) The number of sampling points for simulation and measurement are changed to the same.

However, numerical methods for simulating the combined effect of thermal and moisture conditions are far from being well developed, partially because of the lack of diffusion capability for most simulation software. A common method to handle this issue is to calculate moisture diffusion by implementing the fundamental concepts of heat transfer, and hygroscopic swelling strain can be treated as an additional thermal strain in simulation [2, 39, 52, 57, 59-62]. Some alternative approaches have also been proposed. For example, one approach for ANSYS users is to use “fluence,” another type of body load that is provided by the ANSYS software, to account for the swelling effect [59, 62]. Fan and Zhao have investigated stress caused by the combined thermal, hygroscopic swelling, and vapor pressure load using this method [61]. However, it is difficult to implement the nonlinearities into simulation. For example, “fluence” is not compatible with viscoelastic material properties [62]. Yoon et al. have proposed a method of linking the routines for the purpose of conducting nonlinear stress analysis of semiconductor packages subjected to moisture as well as temperature excursions using ABAQUS [59, 62]. However, such a method involves tricks such as changing the record key and defining the total strain caused by hygroscopic swelling and thermal expansion [62], which added difficulty to the implementation.

4.1.1. T_g Shift

The absorption of moisture by polymeric materials affects their mechanical performance. The stress relaxation curves has been observed to shift towards the left with increasing water content, which is equivalent to the decrease in glass transition temperature (T_g) [63]. A similar behavior can be observed for the storage modulus vs. temperature curve

[64]. Figure 4-1 shows the effect of moisture on the storage modulus of the molding compound measured in Chapter 3. The explanation of this phenomenon is that water molecules interact with the intermolecular forces between the polymer chains, serving as the plasticizer.

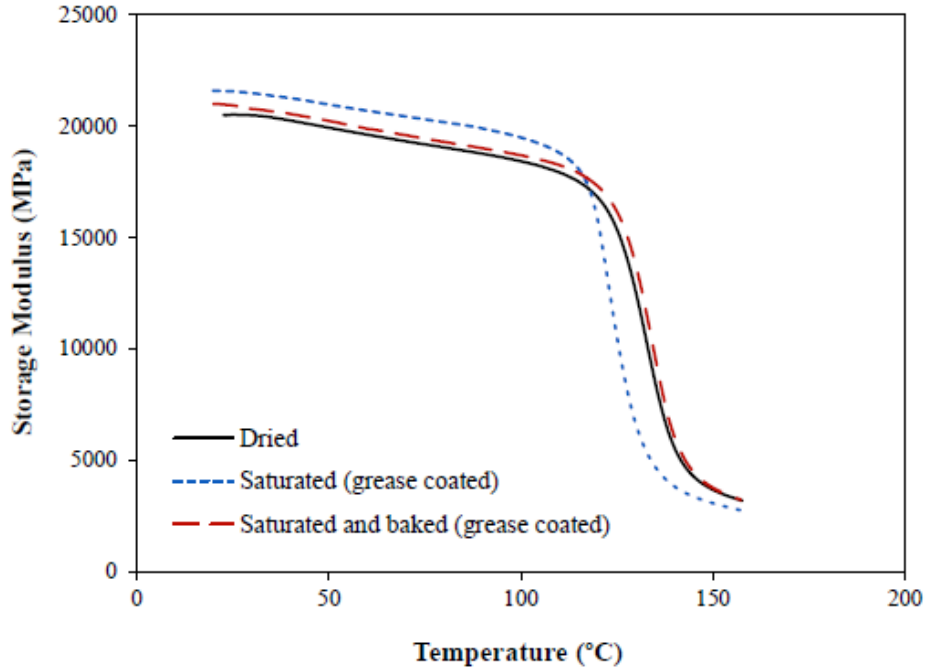


Figure 4-1 DMA result of dried, saturated, and baked (120°C for 5 h) specimen

4.1.1.1. Time–moisture Superposition

The time–water contents superposition has been suggested for the construction of the master curve to describe the hygro-viscoelastic behavior under humid environment [65-67]. For example, a WLF-type shift function, which is analogous to Eq. (2.6), was proposed to account for the effect of moisture on stress relaxation:

$$\log \alpha_H = -\frac{C_1^*(M_c - M_{ref})}{C_2^* + (M_c - M_{ref})} \quad (4.1)$$

where $\log \alpha_H$ is the horizontal shift distance along the abscissa (logarithm scale), M_c is the water content, M_{ref} is the reference water content, and C_1^* , C_2^* are empirical constants determined by the experiment.

Although such a shift function has been proposed to quantitatively describe the T_g shift behavior, the combination of both hygroscopic and viscoelastic characteristics needs to be investigated, with emphasis on the impact of moisture on the viscoelastic behavior, as it has not been published before.

4.2. Finite Element Simulation

A MEMS sensor (exterior shown in Figure 4-2 and cross-section shown in Figure 4-3) was used in this study, and ANSYS 14.5 was utilized as the simulation tool. The elements SOLID 226 and SOLID227 were implemented for building the molding compound, while SOLID186 and SOLID187 were used for other materials. The XYZ displacement of one edge node, YZ displacement of another edge node, and Z displacement of the other edge node on the top surface of the MEMS were constrained as the boundary condition for removing rigid body motions. As the temperature of the post mold cure (PMC) process was 175 °C, it was determined to be the stress-free temperature. The material properties for the molding compound and the die attach adhesive were measured in the laboratory (Table 3-3, Table 4-1, and Table 4-2) while the material properties for other materials were obtained from other studies (Table 4-3).

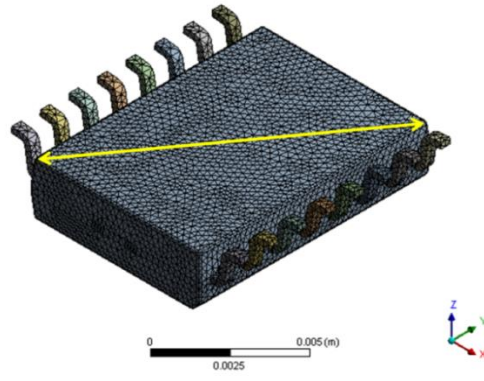


Figure 4-2 FEA model and diagonal to obtain the out-of-plane deformation

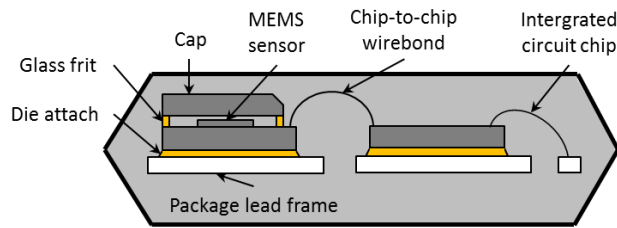


Figure 4-3 Schematic cross section of the MEMS package [68]

Table 4-1 Prony pairs and the shift function of molding compound and die attach adhesive

Molding compound			Die Attach Adhesive		
i	E_i/E_0	τ_i (s)	i	E_i/E_0	τ_i (s)
1	0.040086	0.00284	1	0.057977	0.04066
2	0.061685	0.09544	2	0.084608	0.33913
3	0.051816	1.07389	3	0.120664	2.36345
4	0.137576	10.97108	4	0.102022	24.90482
5	0.107145	104.67782	5	0.051822	318.07815
6	0.121312	434.37762	6	0.054827	1456.59888
7	0.120439	434.73504	7	0.083160	6787.83588
8	0.101512	3065.44095	8	0.099344	75803.5832
9	0.164514	12118.4368	9	0.083345	3105960
10	0.047320	259531.795	10	0.105378	103861000
11	0.022634	6074150	11	0.047853	8948410000
12	0.006793	8875370000	12	0.045569	1.31E+13
E_0 (MPa)	20712.9626		E_0 (MPa)	1733.89353	

Table 4-2 WLF shift function of molding compound and die attach adhesive

Molding compound			Die Attach Adhesive		
T_{ref} (°C)	C_1	C_2	T_{ref} (°C)	C_1	C_2
100	-22.7755	-258.8707	-40	-82.85527	-465.48732

Table 4-3 Material properties for MEMS stress simulation

Material	E (GPa)	CTE (ppm/°C)	ν
Silicon	163	2.6	0.22
Lead frame	129	16.6	0.34
Molding compound	below 100 °C	Table 4-1 & 4-2	13
	above 100 °C		44
Die attach adhesive	Table 4-1 & 4-2	153	0.35
Seal glass	below 135 °C	50	7
	above 135 °C	40	15

4.2.1. Enhancing Solution Efficiency

The SOLID226 and SOLID227 elements are 3D coupled-field solid elements. The degree-of-freedom (DOF) on each node is dependent on the physical field involved in the simulation. For structure-diffusion coupled analysis, there are four degrees-of-freedom on each node: the displacement of each direction (u_x, u_y, u_z) and moisture concentration (CONC). If the temperature also needs to be calculated, structure-thermal-diffusion analysis can be performed, and a fifth DOF (temperature, T) will be involved.

These coupled-field elements are advantageous in that they contain all necessary degrees-of-freedom; hence, it is typically possible to obtain the final solution in just one analysis. Coupling is implemented by formulating proper element matrices or element load vectors. Such a method of coupling is known as direct coupling. Direct coupling is advantageous for handling nonlinear problems; however, a large number of DOFs can become a burden

in computing because the computational complexity of the matrix operation is a power function of the matrix size. In contrast, sequential coupling involves several sequential analyses, each belonging to a different physical field, and the results from the previous analysis are applied as loads for the following analysis. Sequential coupling does not require coupled-field elements.

As mentioned in Chapters 2 and 3, the spatial temperature gradient on a MEMS package can typically be neglected. Besides, several treatments were applied on the model for improving solution efficiency. The materials that are not permeable to moisture are modeled using SOLID186 and SOLID 187, which are 3D solid elements that also have a mid-side node. The moisture contents in the die attach adhesive was not considered in the simulation because the amount of moisture in the die attach is significantly smaller than that in the mold; hence, the die attaches were also modeled using structural solid elements. The degenerated 20-node elements (SOLID226 and SOLID186) in tetrahedral shape were converted to 10-node elements (SOLID227 and SOLID187).

It is imperative to properly set the coupling option and select the proper equation solver. Two coupling options can be used: matrix coupling (strong coupling) and load vector coupling (weak coupling). Matrix coupling leads to an unsymmetrical matrix, but a coupled response is obtained after one iteration in linear analysis. For load vector coupling, a symmetric matrix is produced, but at least two iterations are required to achieve a coupled response [33].

The preconditioned conjugate gradient (PCG) solver is an iterative equation solver, which requires less disk file space than the sparse direct equation solver, and runs faster for large models. Therefore, the PCG solver is suitable for analyses in this chapter. However, the PCG solver only applies to symmetrical matrices. Therefore, load vector coupling has to be selected in key options for the elements; otherwise, the sparse solver will be automatically chosen if the program finds that the PCG solver is not suitable for unsymmetrical matrices. The simulation has shown that using load-vector coupling with the PCG solver can significantly decrease computational time.

In addition, shared-memory parallel computing was applied for the complete utilization of computational resources of the server. The number of processors was set to the maximum number allowed by the software license. It is also possible to use distributed computing through a message passing interface (MPI). The differences between these high-performance scientific computing technologies can be found in Ref. [69].

4.2.2. Validation Simulation

For the validation of simulation, the out-of-plane deformation of the MEMS sensor device was measured by DIC and compared with the simulation result. The simulation model was cooled from 175 °C to 25 °C. The relative deformation to 25 °C was analyzed to eliminate the effect of cure shrinkage. This approach is valid because this study is focused on the comparison of relative stress, and cure shrinkage is an additional deformation and is constant with changes in temperature [70]. The data for comparison were extracted from the diagonal of the bottom surface (Figure 4-2). The simulation

results did not identically match those obtained from experiments; however, the out-of-plane deformation range over temperature can be estimated with reasonable accuracy (Figure 4-4 and 4-5). As for the discrepancy between numerical simulation and optical measurement, DIC results typically exhibit more variation along the measurement path; however, if we compare the mean deformation value (i.e., the area under the curve divided by the length) at each temperature (averaging the datum collected from each location), the simulation and experiment exhibit similar trends on the relationship between deformation and temperature in the range of 50 °C to 150 °C. In addition, the residuals of the mean deformation for all temperatures are less than 0.6 μm , while the sensitivity of DIC measurement for this sample dimension is 1 μm . Admittedly, the residual for some data points are beyond this value; however, the residuals do not have any credible correlation with temperature.

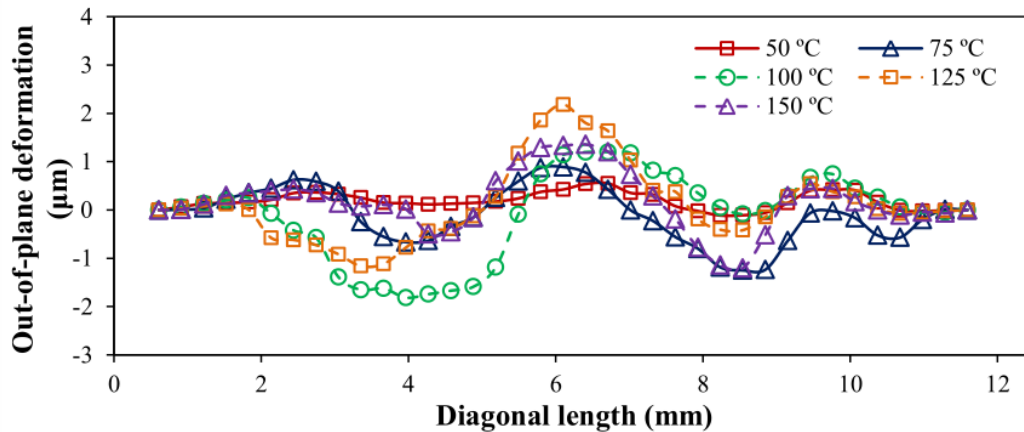


Figure 4-4 Deformation from experimental measurement using DIC

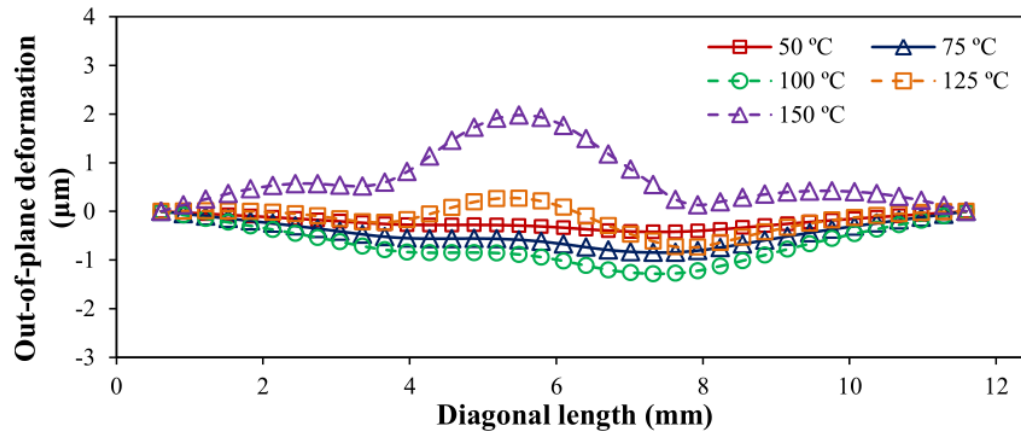


Figure 4-5 Deformation obtained from simulation

In addition, the FEA stress and displacement data were imported to the MEMS sensor and package interaction (MPI) simulations at ADI. The result of MPI was internally validated with device offset.

4.2.3. Moisture Change during Temperature Cycle

Temperature cycling was simulated to evaluate the effect of moisture on the MEMS device under stress. After the sample was cooled to 25 °C from 175 °C (stress-free temperature), it absorbed moisture and reached saturation. Then, the sample underwent temperature cycling, in which the desorption of moisture occurred simultaneously. A saturated concentration (C_{sat}) of 0.004 mg/mm³, measured at the 85°C/85%RH condition, was also utilized for 25 °C, because there is no strong relationship between the saturated concentration and temperature below 100 °C [24]. Each cycle consists of ramp up and ramp down processes at a rate of 2.5 °C/min, 125 °C dwelling for 15 min, and 25 °C dwelling for 15 min. For implementing the fully saturated condition at 25 °C in the

simulation, the transient effect on diffusion field was switched off at 25 °C, and the saturated condition was applied on the surface of the mold (fully saturated boundary condition). This step was solved for the generation of a fully saturated steady-state solution. After the model was saturated, the concentration of moisture at the surface of mold was changed to zero (fully dried boundary condition), and the time integration on the diffusion field was switched on to include the transient effect of moisture diffusion. This is the first step of the desorption process. The transient effect on structural fields remained off during the whole simulation. The amount of moisture in the mold was calculated and plotted in Figure 4-6. It is obvious that the desorption rate at high temperatures is much greater than at low temperatures. After two cycles, about a half of the moisture still remains in the molding compound.

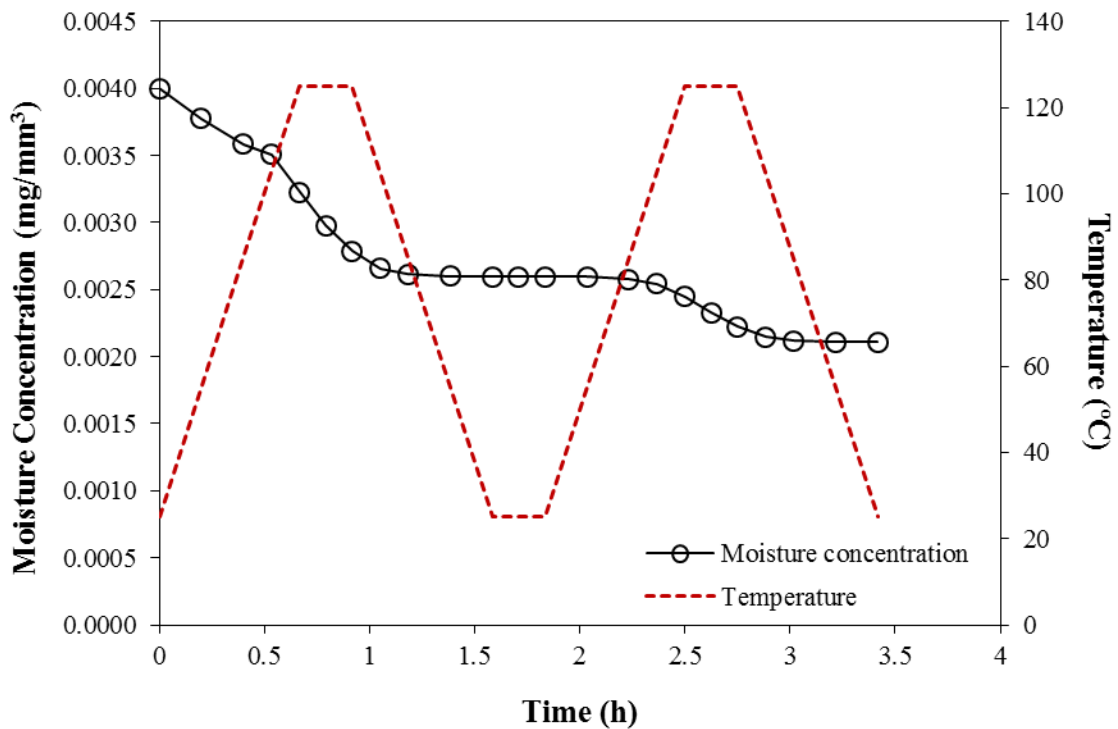


Figure 4-6 Desorption of moisture during temperature cycling

4.2.4. Implementation of T_g Shift Effect in Simulation

The CHS can be handled with ANSYS 14 or a later version by inputting a material property called the “coefficient of diffusion expansion,” while the impact of moisture on viscoelastic behavior is a more challenging issue in simulation. The dry, moisturized molding compound has been observed to exhibit different behavior in the stress relaxation test [65-67] and dynamic test (Figure 4-1). Previously, researchers have proposed the idea of “time-water contents superposition,” in an attempt for describing the relationship between moisture contents and stress relaxation using shift functions such as WLF. Despite the efforts in conducting experiments, this effect has not been sufficiently emphasized in simulation. In this study, for illustrating the impact of moisture on viscoelasticity, the T_g in the shift function was modified. Instead of performing a series of stress relaxation tests, the new shift function was estimated for saturated samples based on the amount of T_g shift from the DMA test.

If we recall, we can theoretically calculate the storage modulus from Prony series by performing a Fourier transform

$$E(\omega) = E_{\infty} + j\omega \sum_{i=1}^n \int_0^{\infty} E_i \exp(-i\omega t) dt \quad (2.14)$$

which gives

$$E_{\text{storage}} = E_0 \left(\alpha_{\infty} + \sum_{i=1}^n \frac{\alpha_i \tau_i^2 \omega^2}{1 + \tau_i^2 \omega^2} \right) \quad (2.15)$$

and recall that the shift function is used to correlate the material behaviors at different temperatures (rewritten from Eq. (2.4) and Eq. (2.5))

$$\tau_i^{(T)} = \frac{\tau_i^{(T_{\text{ref}})}}{A(T)} \quad (4.2)$$

where

$$\log_{10}A(T) = \frac{-C_1(T - T_{\text{ref}})}{C_2 + (T - T_{\text{ref}})} \quad (2.6)$$

If the reference temperature T_{ref} is decreased in the WLF shift function (Eq. (2.6)) by ΔT maintaining C_1 , C_2 , and Prony series as the same, the stress relaxation curves would shift leftward by the corresponding amount in the logarithm time scale. In addition, the storage modulus with respect to the temperature curve will shift leftward by exactly ΔT . To demonstrate this effect, a curve of modulus versus temperature, as shown in Figure 4-7, was plotted for dry and saturated mold material by a theoretical calculation. The T_g shift effect is clearly similar to the trend observed in experiments. The shift function for the molding compound can be updated in each load step:

$$\log_{10} \alpha_T = - \frac{C_1 \{T - [T_{\text{ref}} - \Delta T(C)]\}}{C_2 + \{T - [T_{\text{ref}} - \Delta T(C)]\}} \quad (4.3)$$

where $\Delta T(C)$ represents that the amount of T_g shift is a function of the moisture content (concentration).

For simplifying the simulation, the amount of T_g shift (ΔT) was set to be proportional to the moisture concentration. For the saturated condition, a shift of 10 °C was applied.

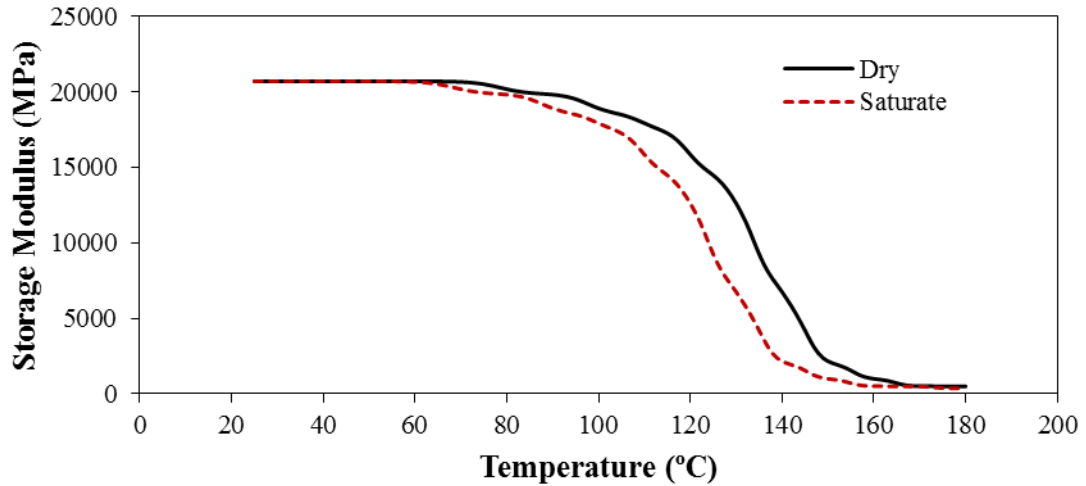


Figure 4-7 Effect of changing the reference temperature of the shift function (1 Hz test frequency)

Figure 4-8 shows the impact of moisture on MEMS stress during thermal cycles. Three cases were compared: 1) considering both hygroscopic swelling and T_g shift, 2) only considering the hygroscopic effect, and 3) “dry” sample, which exhibits no moisture effect. For implementing the T_g shift effect, the easiest approach is to change the shift function for the molding compound after each load step using the moisture data in Figure 4-6. The normal stress was plotted on the X-axis at the center node of the top surface of MEMS. The time left at the origin point on the X-axis is an arbitrary time before temperature cycling begins. The initial point indicates the stress at 25 °C after the cooling process begins from 175 °C. The expansion of the molding compound caused by moisture absorption alleviates the compressive stress from the cooling process before temperature cycling. After temperature cycling, three notable phenomena are observed. First, the compressive stress decreases in temperature cycling, caused by the stress relaxation effect of the molding compound. The most significant change happens in the

first cycle. Second, the hygroscopic swelling behavior results in small compressive stress; however, the effect becomes less significant as the moisture is lost because of thermal cycling. Finally, when the T_g shift effect is considered, the stress change is greater. As a result, the stress after cycling is smaller.

This simulation result should be an indicator of the deviation of the MEMS device output from its initial null output. Assuming that the starting points of the graph in Figure 4-8 are the initial device outputs after the PMC process, the greater signal shift is clearly generated with moisture after temperature cycling. This signal shift can be minimized by the design of a robust sensor, selection of appropriate packaging material, and optimization of the manufacturing process.

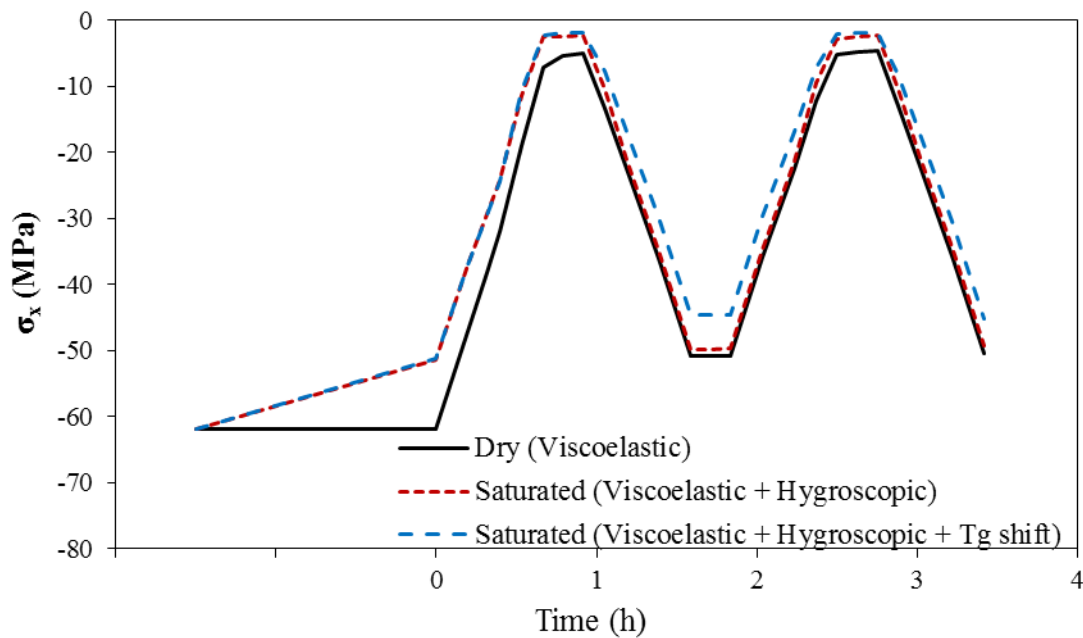


Figure 4-8 MEMS stress during temperature cycling

4.2.5. Effect of Non-Uniform Moisture Distribution on the Stress

Relaxation Behavior

In Figure 4-8, the T_g shift effect is implemented by changing the shift functions for the mold using the averaged concentration shown in Figure 4-6. In fact, the concentration of moisture within the mold is spatially different. Therefore, the curve with T_g shift effect in Figure 4-8 is the result of a partially lumped method, because the CHS is calculated using the moisture concentration of each element in the mold, while the modified shift function is achieved by the averaged concentration. For a rigorous investigation, it is necessary to apply different shift functions to different elements according to their own concentration and compare the difference with the partially lumped approach. Besides, two simulations were required for obtaining curve with the T_g shift effect in Figure 4-8: the first one calculated concentration, while the second applied the new shift functions based on the calculated concentration; some manual interventions were involved. This is quite natural for a research process, but it is better to make the simulation more automatic and accomplish the task in one analysis.

4.2.5.1. Implementation Using APDL

The APDL is a powerful scripting language, which allows for control flows such as choice and loops. APDL can be used to parametrically build geometry, control meshing, set up solution control, access the result, and automatically write into data files using the desired format.

By default, the shift functions that were built in ANSYS are only dependent on temperature. Thus, it is impossible to input a moisture-dependent shift function using the APDL code. However, it is possible to change the assignment of materials to any element in the model, although such usage is not recommended. Therefore, we can pre-define several additional material models for different moisture levels, each having its own shift function with all other material properties unchanged. It would be advisable to have consecutive material ID numbers for those material models defined for the molding compound, which adds convenience to programming. The molding compound has to be assigned with a defined material ID for meshing. If the moisture is not uniform at the start, we can temporarily assign any material ID, for example, the ID for “dry” mold, then set the material property according to the amount of moisture before the first load step involving moisture. This is the initialization of material assignment.

After each load step, the concentration of moisture in each element is checked in the general postprocessor (/POST1) using a loop in APDL code. The new material ID that will be associated to each element in the next step is calculated and it is written into a file containing a series of “MPCHG” command lines:

```
MPCHG, New_Material_ID, Element_ID
```

The number of lines in the command file equals the number of mold elements in the finite element model.

Because the moisture concentration of each element is a real number, but the number of pre-defined material models is limited, some round-off errors are generated. However,

because of a large number of elements, the round-off errors may possibly cancel with each other considerably.

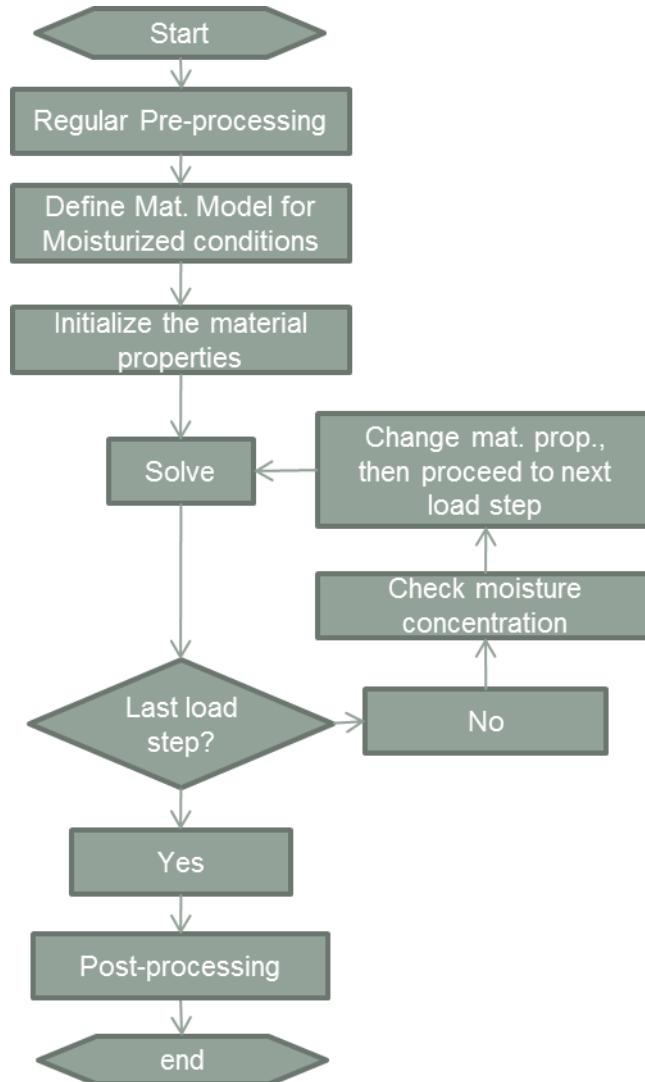


Figure 4-9 Flow chart showing the simulation using APDL

After the command file is written to the disk, the program returns to the solution processor to restart analysis. Then, the command file is read, and the material

assignments are updated by executing all commands in the file. After the material properties are updated, the solve command for the next load step is executed. This process continues until the final load step in the analysis is completed. Finally, post-processing is performed for retrieving the results for further analysis. Figure 4-9 show the simulation flow chart.

Two simulations were performed using this approach. In one simulation, 10 additional material models were defined for describing the behavior of materials under moisture conditions. Therefore, shift functions for 11 different moisture levels (from the dry to the saturated state) are available in the model. In the other one, 40 additional material models were defined for the same range of moisture concentration.

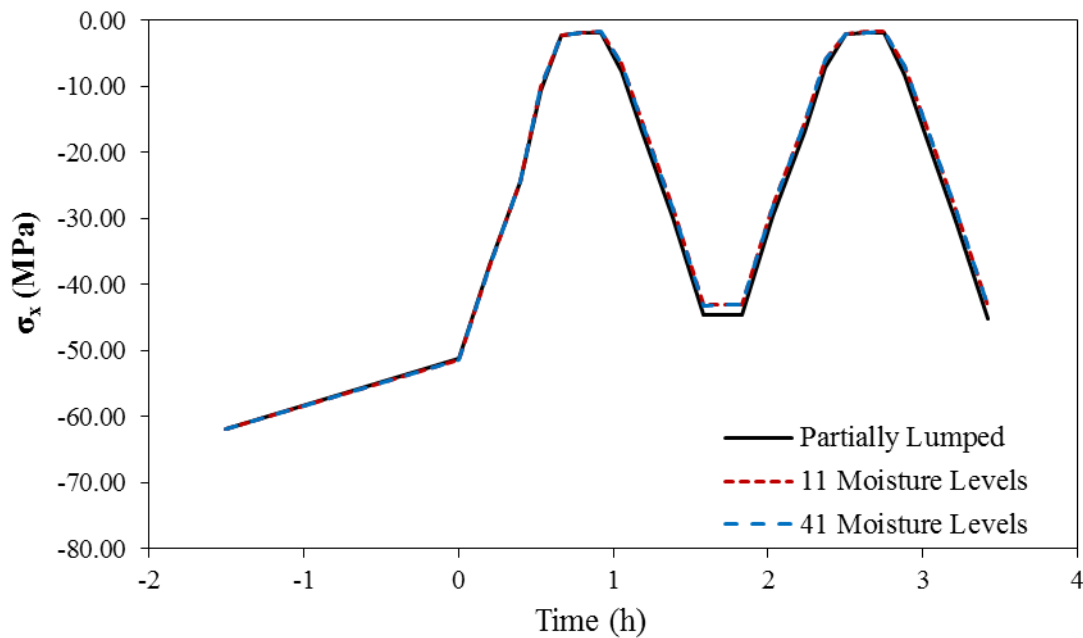


Figure 4-10 Effect of non-uniform moisture distribution on the stress relaxation behavior of the molding compound and resulted stress on MEMS die

Figure 4-10 compares the MEMS die stress with and without considering the effect of non-uniform moisture distribution on the stress-relaxation behavior of the molding compound. The solid line represents the result from the “partially lumped” method, which ignores the moisture non-uniformity when applying the T_g -changed shift function, but considers the moisture non-uniformity for calculating hygroscopic strain. This curve is the same one as the “Viscoelastic + Hygroscopic + T_g shift” curve (dash with large spacing) in Figure 4-8. If the effect of non-uniform moisture distribution on the stress-relaxation is considered, the stress–time curve will be similar to the two dash curves in Figure 4-10. The relative difference between two dash lines is less than 0.1 MPa; hence, it is difficult to distinguish them, while the difference between the solid and dash lines becomes distinct starting from the cooling step of the first cycle. Compared with the “partially lumped” method, the stresses calculated when considering the effect of non-uniform moisture distribution on stress relaxation are smaller. Generally, the difference between the solid and dash is smaller at higher temperature and becomes larger at lower temperature, and such a difference in the second cycle is more obvious than in the first cycle. The maximum difference with a value of 1.8 MPa occurs at the end in the simulation, which is approximately 30% of the difference between the dry and saturated parts with moisture non-uniformity considered for both strain and T_g shift calculations. Therefore, it is advisable to include the effect of non-uniform moisture distribution on the stress-relaxation behavior in the model.

4.2.5.2. User-Programmable Feature

The ANSYS user programmable feature (UPF) permits users to write their own routines (usually in Fortran) and link them to ANSYS or use them as external commands to access a database, define a new material behavior, set up a new failure criterion, create a special element type, or modify and monitor existing elements.

ANSYS provides a user-defined subroutine “UsrShift.F,” which allows the users to write their own shift function that was not built in with the software release, for example, polynomial-based shift function in Eq. (2.8). The input and output arguments for the subroutine have been defined and cannot be changed; otherwise, the subroutine cannot work normally. The input and output are defined as

```
*deck, UsrShift    USERDISTRIB  parallel  user                                jlu
c Copyright ANSYS.  All Rights Reserved.
      subroutine UsrShift(dx1,dx1half,timinc,
&                temp,dtemp,tofst,propsh,nTerms)
c*****
c   calculate pseudotime time increment according
c   to a user specified shift function
c
c *** Notice - This file contains ANSYS Confidential information ***
c
c  input arguments:
c    timinc  (dp,sc,in)      - time increment
c    temp    (dp,sc,in)      - current temperature, t_n+1
c    dtemp   (dp,sc,in)      - temperature increment, t_n+1 - t_n
c    tofst   (dp,sc,in)      - temperature offset to absolute zero
c                               (specified by TOFFST command)
c    propsh  (dp,ar,in)      - Constants for shift function
c                               (User's input using TB,SHIFT,,,USER)
c    nTerms  (int,ar,in)     - number of user defined constants
c                               (specified in TB,SHIFT,,,nTerms,USER)
c  output arguments:
c    dx1     (dp,sc,out)     - pseudotime increment
c    dx1half (dp,sc,out)    - pseudotime increment over the upper half span
c*****
```

where *dp* represents double precision, *int* represents integer, *sc* represents scalar, *ar* represents array, *in* represents input argument, and *out* represents output argument in

the comment part. Unfortunately, the moisture data cannot be accessed using the information available in this subroutine. Thus, it is not possible to write a “grand” shift function, which involves both temperature and moisture concentration, by the simple modification of the `UsrShift.F` subroutine. Another idea for implementing the “grand” shift function is rewriting the material model, which can retrieve the moisture concentration and pass it to a new subroutine for the grand shift function. However, the work required for this task will be enormous. The users have to update the stress state and calculate the Jacobian matrix, and potential issues exist on convergence. Comparatively, implementation using APDL is easier. Hence, the effect of non-uniform moisture distribution on the stress-relaxation behavior was only studied by ADPL-based simulation.

4.3. Summary

This chapter covers several gaps in previous studies. Previously, the comprehensive effect of hygroscopic swelling and thermal expansion has seldom been studied using the viscoelastic model. Although Yoon et al. have developed a method for combining all these three effects [59, 62], no detailed study has been reported for MEMS packaging stress with this scheme. Besides, moisture has been found to accelerate stress relaxation; however, such effects have never been considered in simulation before.

In this chapter, comprehensive studies are conducted on the hygro-thermo-viscoelastic behavior of the molding compound and the resultant packaging stresses. Transient moisture simulation is performed, and the stress induced by thermal and hygroscopic

effects is simultaneously calculated. The impact of moisture on the stress relaxation behavior is implemented in ADPL, and results show that it is advisable to consider such an effect.

Chapter 5. Introduction to 3D Packaging¹¹

Three-dimensional (3D) packaging with through-silicon-vias (TSVs) is an emerging technology, which features smaller package size, higher interconnection density, and better performance; 2.5D packaging using silicon interposers with TSVs is an incremental step toward 3D packaging. TSV formation and interconnection between chips and/or wafers are two key enabling technologies for 3D and 2.5D packaging, and different interconnection methods in chip-to-chip, chip-to-wafer, and wafer-to-wafer schemes have been developed. This chapter reviews the state-of-the-art interconnection technologies reported in recent technical papers. Issues such as bump formation, assembly and bonding, and underfill dispensing in each interconnection type, are discussed.

5.1. Background

In recent years, driven by the demand for new electronic products with smaller size, lower power consumption, and better performance, 3D packaging is attracting increasing attention from academia and industry. Traditional electronics are integrated in a 2D scheme; in the past, typically only one chip was encapsulated in a package. Later, the

¹¹ Reprinted, with permission, from Liu, D. and Park, S., 2014, “Three-Dimensional and 2.5Dimensional Interconnection Technology: State of the Art”, J. of Electronic Packaging, **136**, p. 014001. Copyright © 2014 ASME.

system in package (SiP) technology led to the encapsulation of several chips into a single package, which increases the speed while reducing the size of the package.

Some of the earliest 3D packages were stacked die SiP packages with wire bond connection. In these packages, different dies might be connected either directly with each other or indirectly using a substrate. In some types of packages, wire bonding and flip-chip technologies can be used together. The bottom-most chip is connected to the substrate with flip-chip solders, while other chips are connected using wire bonding (Figure 5-1). However, the density of the wire bonds is restricted by the dimension of the die periphery, and a relatively long wiring path also prohibits further improvement in performance. Hence, 3D interconnection technology using TSVs is the most promising solution for next-generation packages. Compared with wire bonding, TSV-based approaches provide shorter wiring distances and higher density; therefore, they have a smaller form factor and better electrical performance.

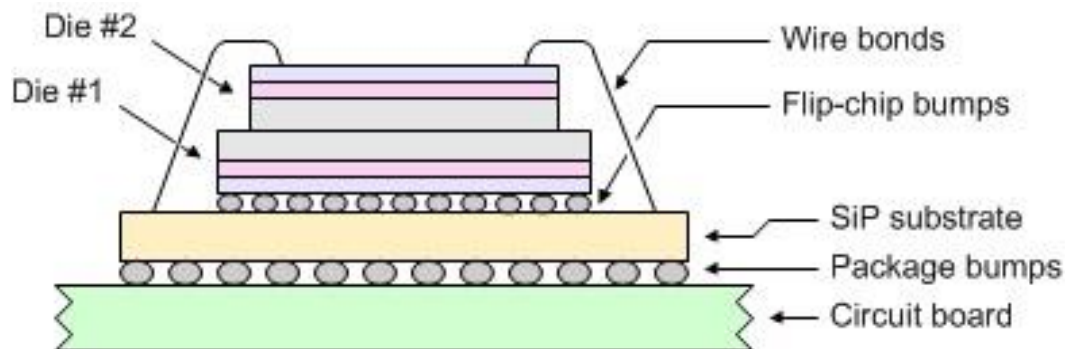


Figure 5-1 3D SiP with wire bonds and flip-chip bumps [71]

In recent years, methods for fabricating TSVs have been extensively investigated, and different types of TSVs have been developed. From the geometry point of view, annular

or fully filled vias with different taper angles were manufactured [72]. The filling material might be copper (Cu), tungsten (W), polysilicon [73], solder material with Cu particles [74], and conductive adhesive [75], etc. Some TSVs serve as electrical connections while some are designed as thermal TSVs (TTSVs) to dissipate the heat and improve thermal management [76, 77]. Various manufacturing processes have been studied for the creation of a void-free TSV as rapidly and cheaply as possible. Currently, although 3D packages with TSVs have not been widely used in products, electronic packages with silicon interposers containing TSVs (such as Xilinx Virtex-7 FPGA [78], etc.) are already entering the market. Because the coefficient of thermal expansion (CTE) of the silicon interposer is similar to that of the die, the silicon interposer can prevent the brittle ultra-low κ dielectric material of the die from cracking. Packages with TSV interposers are regarded as 2.5D packages. Figure 5-2 shows a cross-sectional image of the Xilinx Virtex-7 FPGA product, and the Si interposer with TSVs can be clearly observed.

For the electronics manufacturing industry, 3D packaging is a brand new area, which is significantly more than simply creating TSVs through wafers or dies. It involves challenges in various aspects such as materials [79], process control, supply chain, thermal management [76], reliability [80], and design guidelines. Among 3D integration processes, it is crucial for creating interconnections between the stacked dies or wafers. A reliable, low-cost, high-performance 3D package must be assembled with a reliable interconnection technology. Generally, technologies for 3D interconnection are categorized into three stacking schemes: chip-to-chip (C2C), chip-to-wafer (C2W), and

wafer-to-wafer (W2W). In each scheme, the interconnection technologies differ from each other in terms of the interconnection structures, interconnection and underfill materials, and process flows. In journals and at conferences that focus on 3D packaging, several novel types of interconnections have been reported. In this paper, recent advances in 3D and 2.5D interconnection technologies are summarized, and the similarities, differences, advantages, and potential drawbacks of these approaches are discussed briefly.

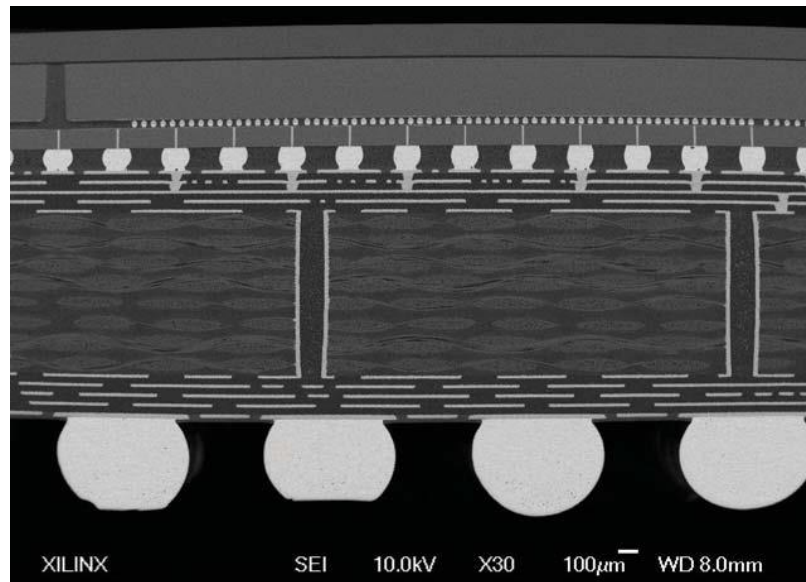


Figure 5-2 Cross-sectional image of a package with an interposer containing TSVs developed by Xilinx [78]

5.2. Chip-to-Chip and Chip-to-Wafer Interconnection

Currently, chip-to-chip (also known as die-to-die or D2D in some studies) stacking is being widely researched in 3D interconnection. In this stacking scheme, although the

TSVs are typically fabricated at the wafer level, the wafer is diced into chips before stacking. This technology not only minimizes the change in bonding tools but also ensures that only “known good dies” (KGDs) are used in the assembly, which affords high yield. Chip-to-chip stacking is a very flexible technology, and chips with different sizes can be integrated in one package. Chip-to-wafer (also known as die-to-wafer, D2W) approaches may also share these advantages. In the chip-to-wafer approach, the difference lies in the fact that the chips are connected to the wafer, and the singulation of each stack is performed after the assembly, or even after underfill dispensing and molding [81]. Multiple chips can be bonded to a temporary carrier and then simultaneously assembled to the wafer. Therefore, chip-to-wafer stacking can achieve throughput higher than that obtained by chip-to-chip stacking. In addition, a specially designed template can be used as the carrier for improving alignment precision [82]. In recent years, numerous advances have been reported in chip-to-chip and chip-to-wafer approaches, several of which use fine-pitch micro-bumps or Cu pillars for interconnection and adopt improved underfill dispensing technologies.

5.2.1. Bump Structure

In recent years, various types of interconnection with different materials, sizes, and even structures have been reported. Common interconnection structures, such as micro-bumps and Cu pillars, have been used in 3D chip-stacking structures [83-92]. Generally, interconnection is trending in the direction of smaller dimension, finer pitch, and higher interconnection density. Bumps with a pitch of 10 μm have already been studied [84]. In recent years, some innovative bump structures have been invented, such as the Ni micro-

insert [93-95] and the Cu–Sn interlocking bump [96, 97]; they have also been applied to 3D interconnections. Figure 3 shows a cross-sectional view of interlocking bumps fabricated by Jang et al. [98]. Sn bumps (25 μm in diameter and 15 μm in height) were fabricated on one chip, and the Cu interlocking bumps on the other chip were inserted into the Sn bumps using flip-chip bonding. Planar bumps (70 μm in diameter and 10 μm in height) directly fabricated on Cu TSV were also used in the same paper (Figure 5-3). Souriau et al. have utilized micro-insert interconnection technology in their chip-to-wafer stacking study [99]. In that process, a matrix of micro-inserts composed of Ni was inserted in a soft NiSn material, which was formed on the corresponding location on the wafer (or on other dies). Figure 5-5 shows the image of the micro-inserts matrix. These novel structures have several benefits. First, they meet the trend of miniaturization in the packaging industry and enable high-density interconnection, one of the driving forces of TSV-based 3D integration. A small bump size not only decreases the distance between dies but also leaves more space on the die so that more TSVs can be fabricated. Second, these structures are compatible with mature flip-chip bonding techniques for chip-to-chip or chip-to-wafer connections. In addition, mechanical robustness and electrical performance have been tested [98, 100]. Some disadvantages of these novel structures have also been pointed out in studies. For instance, the micro-insert approach is sensitive to planarity, and non-flatness may increase electrical resistivity [93].

The Cu pillar bump technology has emerged in recent years. This technology enables a small pitch size and high interconnection density. Compared with the solder-bump-based interconnection, a Cu pillar with a solder cap exhibits several advantages such as higher

standoff and less solder spread out [101, 102]. Although this technology was invented not long ago, it has already been used in 3D/2.5D packaging [89, 103], and the effect of solder capping material has been studied [104]. Direct Cu to Cu bonding by thermocompression, which can connect two Cu pillars (or studs) without using any solder material, has also been researched [105, 106].

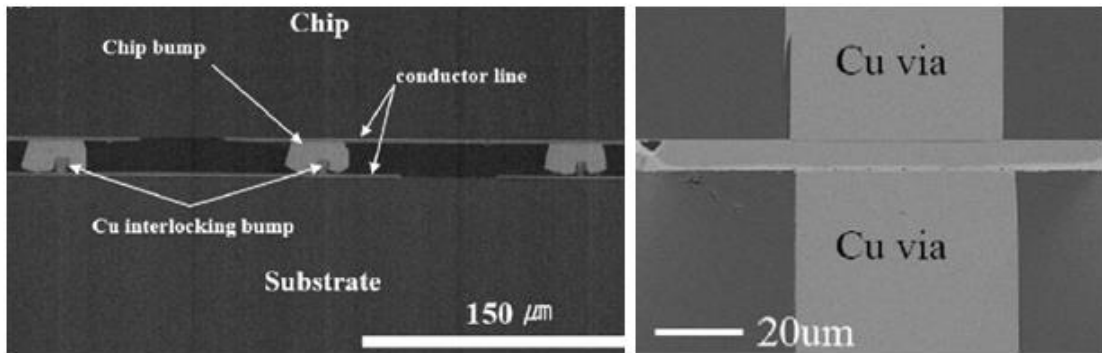


Figure 5-3 Cross-sectional image showing interlocking Sn/Cu bumps (left) and a Cu planar bump with TSVs (right) [98]

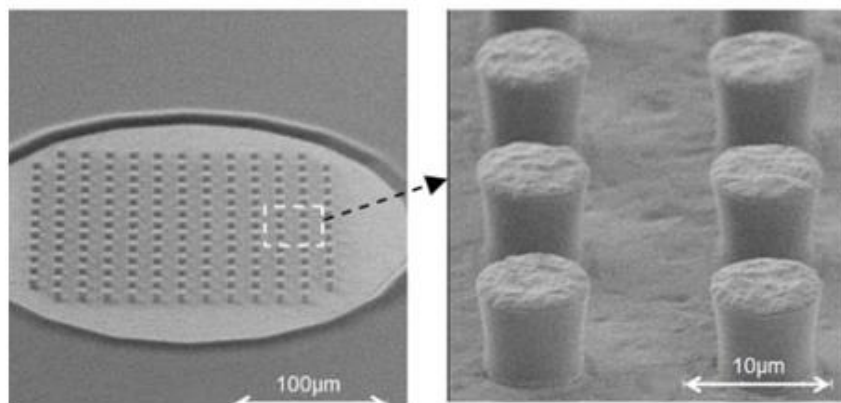


Figure 5-4 Image of the fabricated micro-inserts [99]

5.2.2. Bumping and Assembly Process

Bump or pad formation is an important step in packaging. Various bumping methods have been investigated for making the process more efficient and reliable.

The controlled collapse chip connection (C4) technology, which was invented by IBM in the 1960s, is a well-established interconnection technology. Since its invention, different methods of making C4 bumps, such as masked evaporation [107], paste screening [108], and photolithographic electroplating [109], have been developed. Currently, IBM has developed C4 bumping technology, the C4-New Process (C4NP); this technology has already been used in 3D chip-stacking [91, 92, 110]. The C4NP process utilizes a glass mold with cavities to transfer solder to the wafer. Molten solder is injected in the mold cavities, and then the mold is aligned below the wafer. Then, the wafer and mold are heated above the melting temperature of the solder in a sealed-off manufacturing environment; as a result, the solder will wet the under-bump metallization (UBM) and attach to the wafer. Figure 5-5 shows the schematic of the C4NP process. Compared with other bumping methods, this approach combines several advantages, such as the capability of fabricating fine-pitch bumps in volume production, easy change of solder materials, environmentally friendly manufacturing (no plating chemical), and low cost. [110].

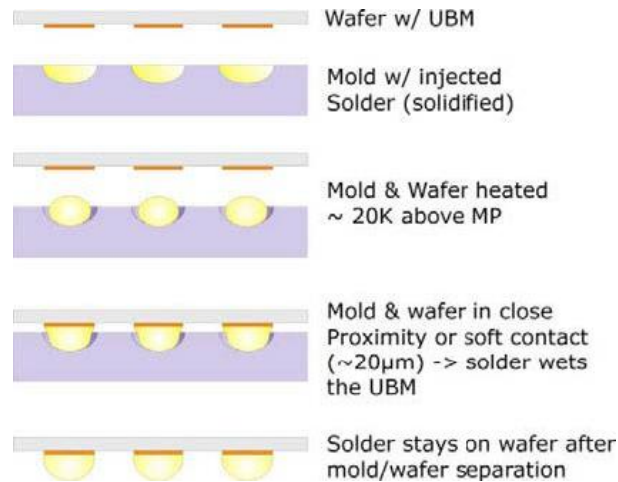


Figure 5-5 Process of solder transfer in C4NP technologies [91]

Plating can be utilized for fabricating tiny bumps; it is another popular method for bumping and forming UBM. Electrolytic and electroless plating are widely used; for example, Cu pillars with different solder caps can be formed by electroplating [111]. Reflow and plasma cleaning, which removes contamination and the oxidation layer, might be conducted after plating [112]. Various deposition methods are also commonly employed. For example, in the micro-insert approach by Souriau et al., Ni and NiSn layers are formed by electroplated chemical deposition (ECD) on a Ti/Cu seed layer, while the seed layer is deposited by physical vapor deposition (PVD) [99].

Typically, TSVs are made by an approach involving (usually, chemical-mechanical planarization, CMP) the removal of overburden Cu. However, recently, by improving the TSV filling process, the Cu micro-bumps on the active side of the TSV are directly formed by electroplating in the TSV-filling process; hence, there is no need to remove Cu

and perform extra bumping on that side [113]. Figure 5-6 shows the TSVs and Cu micro-bumps fabricated by this novel process.

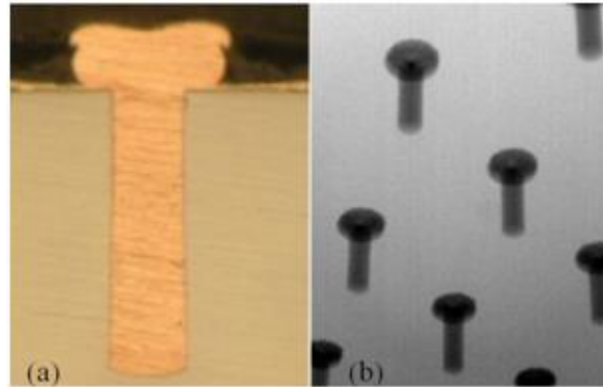


Figure 5-6 Cross-sectional image of Cu-filled TSV with Cu micro-bumps (a) and X-ray photo of TSV after Sn plating (b) [113]

A solder bump maker (SBM) technology that does not require the solder mask has also been reported [114-116]. The SBM is composed of resin, additives, and Sn58Bi solder powder. A guide is used for controlling the thickness of the SBM layer, and excessively printed SBM materials are removed using a blade. Then, the guide is removed, the chip is reflowed, and the bumps are formed. A coining process is applied for guaranteeing the height uniformity by compressing the bumps at elevated temperature. The SBM bumps have low volume and can be directly formed on the top of the TSVs. Figure 5-7 shows the schematic of bumping, and Figure 5-8 shows the cross-sectional image of the bumps after coining.

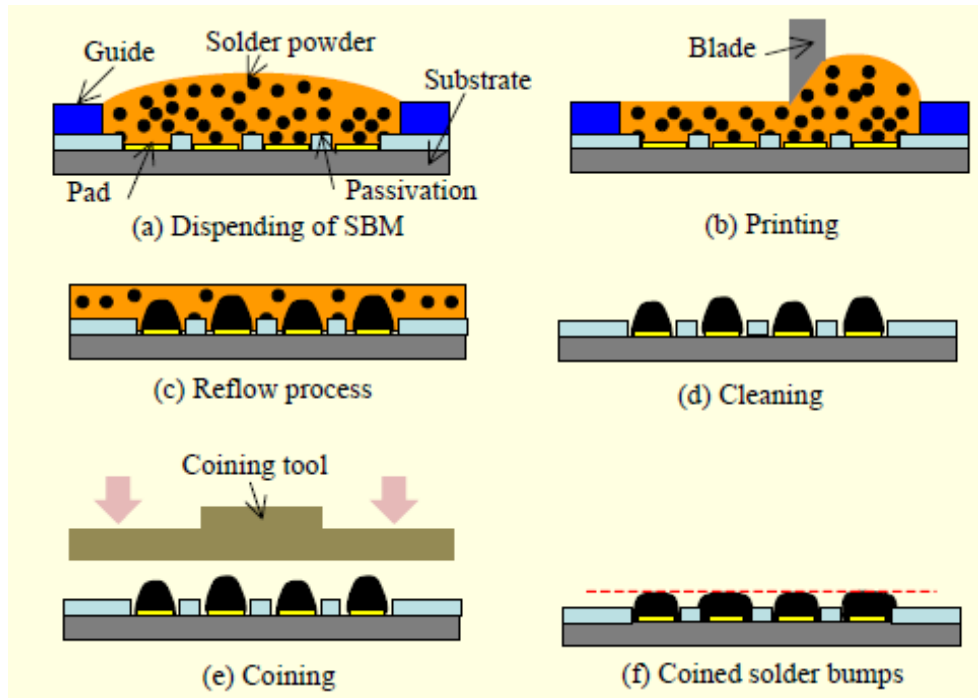


Figure 5-7 Schematic of SBM bumping [115]

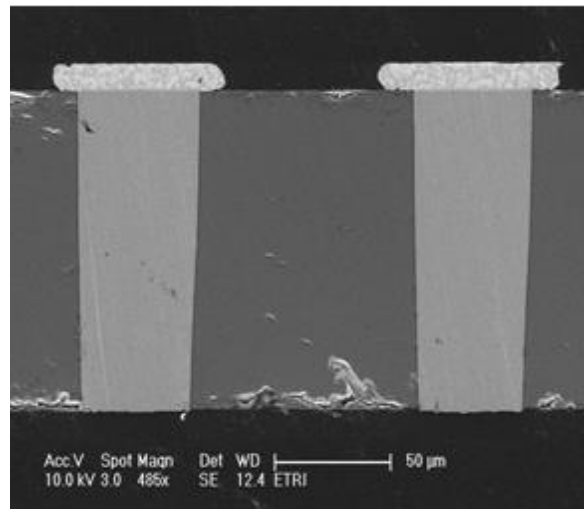


Figure 5-8 Cross-sectional image showing TSVs and coined bumps [116]

New interconnection materials and bonding techniques are emerging, and various new processes are developed. Traditional flip-chip bonding approaches and several novel

technologies have been introduced in the 3D chip-to-chip or chip-to-wafer packaging area.

5.2.2.1. Bonding with the C4 Reflow Process

Owing to the numerous advantages such as low cost and the ability to rework, C4 is a very successful technology widely used in flip-chip packaging. As flip-chip bonding techniques have been used in 3D chip stacking, C4 interconnections in 3D chip stacks have also been studied [85-88, 91, 92]. In the C4 assembly approach, solders are fabricated on the chip, and then the chip is positioned and placed on the substrate. Finally, the interconnection is created by reflow.

Reflow is one of the most important steps in the C4 process. For 3D assembly, multiple chips must be stacked one over another, and two joining strategies may be used: sequential reflow and parallel reflow. In the former, the bottom chips are mounted first, followed by reflow. Then, other chips are sequentially assembled from the bottom to the top, and reflow is repeated after each chip is mounted. In the latter, an alternative approach, several chips are mounted together, and then all the chips are joined in a single reflow. Parallel reflow results in higher manufacturing throughput; however, this approach requires better control of the placement process, because the solder bumps are not connected until reflow. In contrast, for sequential reflow, the relative displacement between each layer can be controlled in each joining process, at the cost of time and the risk of dissolving more UBM material in the solder [91]. Both approaches have been

successfully implemented in experiments, and Figure 5-9 shows a three-layer stack by IBM using sequential reflow.

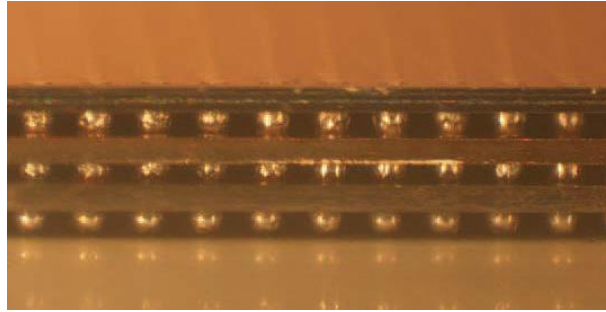


Figure 5-9 A three-layer chip stack fabricated with sequential reflow by IBM [87]

As the size of the micro-bumps decreases, flux cleaning becomes more and more difficult, especially for large dies. Two approaches have been investigated for resolving this issue. One improves the flux-cleaning tools or processes, and the other approach adopts a fluxless bumping method. Au et al. have applied an additional force-flow system to the inline pressurized spray system, and a test on a four-layer stacked-chip module with a 30 μm gap showed that the force-flow system is four times more efficient than only the inline pressurized spray [85]. Maria et al. have attempted two approaches: fluxless bonding approach with formic acid ambient and flux bonding with a water-soluble flux. Both led to successful results [88].

5.2.2.2. Bonding with Thermocompression

In thermocompression, interconnection materials are pressed together at elevated temperature to form joints. The process temperature and pressure depend on the material

and joint geometry. Various studies have been conducted on creating interconnections between stacked strata using thermocompression. For instance, micro-inserts and interlocking bump structures (Sec. 5.2.1.) have been assembled in this manner [98, 99]. Thermocompression does not require reflow and has been used for creating minute, fine-pitch interconnections [83]. Zhan et al. have compared two thermocompression bonding methods: conventional thermocompression, in which the top chip was continuously compressed, and gap-control thermocompression, which contains two compressions, with each compression having its own pressure and duration. The experiment showed that novel gap-control bonding might prohibit the issue of solder squeezing and lead to better bonding results [112].

Direct Cu–Cu bonding with thermocompression offers several benefits such as low electrical resistivity, high thermal conductivity, and low susceptibility to electromigration. Key parameters of this process include temperature, pressure, duration, and surface cleanliness of Cu [117]. The variation of Cu pillar or pad height is a concern, and Lee et al. have proposed a method for compensating the variation in bump height using electroless Ni plating [105]. In the approach by Lee et al., the Cu pillars and Cu studs were formed on two chips. After bonding with thermocompression, the bonded parts were subjected to cleaning, surface roughening, catalyst, and conditioning, followed by immersion in the Ni-P solution for plating. As a result, electroless plating led to improved quality of interconnections by filling the gap between the Cu pillars and the studs, thereby decreasing resistance by 15%.

5.2.2.3. Low-Temperature Interconnection Methods

In addition to traditional thermocompression and reflow soldering, novel low-temperature interconnecting processes have also been developed [118]. In C2C and C2W approaches, low-temperature soldering processes such as the transient liquid phase (TLP) and solid-state diffusion bonding typically feature a low melting point at bonding but a high re-melting temperature due to the formation of an intermetallic layer. These methods may significantly decrease the temperature required at assembly, thereby decreasing the stress induced by thermal mismatch. Bonding materials reported in studies include InSn by Morinaga et al. [119], AuInSn by Xie et al. [120], CuSn by Zhang, Agarwal et al. [121, 122] and Sakuma et al. [123], and CuInNi by Sakuma et al. [123]. Agarwal et al. have employed two relatively low temperature processes for the CuSn material, TLP, and solid metal bonding (SMB). The SMB bonding has a processing temperature lower than that of TLP, which is below the melting point of Sn [121]. Sakuma et al. have compared the reliability of CuInNi and CuSn bonding by finite element analysis (FEA) and experiments, and results indicated that the NiCuIn solder exhibited thermo-mechanical reliability better than that of the CuSn solder. Different failure modes were associated with two material combinations. For CuInNi, the failure was found in In, while for CuSn, failures such as die cracking were observed [123].

Notably, these low-temperature bonding methods exhibit an advantage in that they are not low-temperature processing. The packaging industry is trending in the direction of higher density, more controllable processes, higher thermomechanical reliability, and these goals have been achieved by these novel approaches. For example, in [123], low-

volume CuNiIn solder, a height of only 6 μm is successfully made on an annular, tungsten-filled TSV, and the samples exhibit good reliability in the thermal cycling tests.

5.2.3. Issues on Underfill

Underfill is a key technology for improving the thermal-mechanical reliability of flip-chip packages. Several variations of underfill have been developed for increasing reliability, simplifying the process, achieving higher yield, and decreasing voids [124]. As the industry began to utilize flip-chip technologies for the creation of the chip-stacking structure, this reliability-enhancing technology was also applied to 3D packaging. However, with decreasing distance between chips, dispensing underfill is becoming more challenging. Even then, several researchers have successfully dispensed underfill into small gaps [85, 86, 88, 123]. Au et al. have filled all gaps in a four-die stack package by a multiple line / multiple needle height dispensing process; hence, all gaps are simultaneously filled between the joints [85]. Au et al. have also found that the corner fillet value of conventional filling exposes the top-most solder joint gap interface (Figure 5-10). In contrast to the traditional capillary underfill process in which the flow of underfill is driven by surface tension, a vacuum filling approach was developed by researchers at IBM [88, 125]. In the vacuum filling approach, the flow of underfill is driven by the pressure difference, and this change in the dispensing mechanism leads to better filling quality than capillary underfill process. A scanning acoustic microscope (SAM) image shows that vacuum filling technology can fill a 14 μm gap without leaving a visible void in the underfill, while in its counterpart, the small voids appear (Figure 5-11).

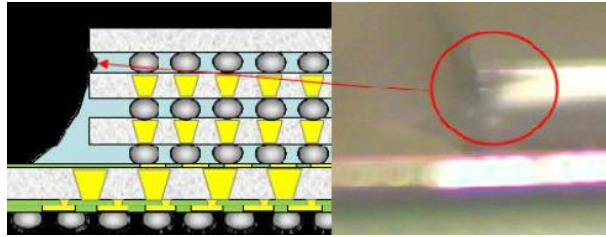


Figure 5-10 A gap exposed using a typical 50% corner fillet value in underfill dispensing [85]

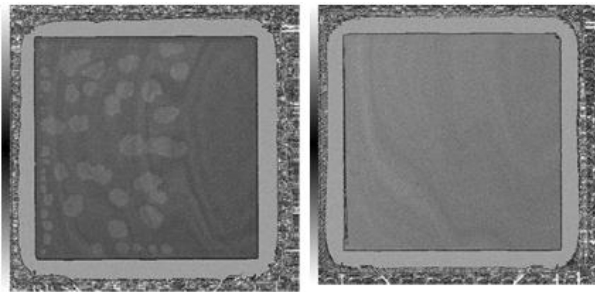


Figure 5-11 SEM image of flip-chip samples after capillary (left) and vacuum (right) underfill dispensing [125]

Instead of dispensing underfill after stacking, another approach uses no-flow underfill (NUF) or an adhesive material for filling the gaps between the chips. No-flow underfill is dispensed before the chip-attachment process and cured after assembly. The solder reflow and cure processes can be integrated, leading to a more efficient manufacturing process. Adhesive materials that are pre-applied before assembly may serve a function similar to that of underfill; therefore, in this paper, the term “simultaneous underfill” is used to describe the materials that simultaneously fill the space between Si chips or wafers with assembly.

Myo et al. have combined In-based low temperature with no-flow underfill [126]. In their study, the chip-stacking structure was fabricated by the sequential attachment of the chips. In each step, the underfill was dispensed onto the substrate (or lower chips), and then the chip was placed and bonded. Agarwal et al. have reported a similar underfill approach for the low-temperature chip-to-wafer bonding with CuSn micro-bumps [121].

Hybrid bonding technologies using metallic materials for interconnection as well as adhesive materials for simultaneous underfill have also been investigated. For example, the Cu/Sn interlocking bump technology in Sec. 5.2.1. uses adhesive for filling the gap and securing the structure [98]. Some scholars use the term “wafer-level underfill” (WLUF) for the pre-applied material on the wafer that glues the chips or wafers together during assembly and serves the same function as regular underfill later [124]. During manufacturing with wafer-level underfill, bumping is performed at the wafer level, and then the wafer-level underfill is applied on the wafer, usually by spin-coating (or vacuum lamination, screen printing, and stencil printing). A B-stage cure process follows if the underfill is initially in the liquid state. Then, the wafer is diced for assembly if chip-to-chips or chip-to-wafer stacking is used [127].

The resin or filler on the bump surface is a problem potentially affecting connection. For getting rid of these materials, hybrid bonding technology with a planarization process has been developed. Typically, the planarization process is CMP or diamond bit cutting. Nimura et al. have developed a low-cost thermal pressure planarization process. In their

approach, the resin was compressed by a silicon substrate coated with a release agent. The solder with adhesive and Au with adhesive bonding have been successfully implemented after this novel planarization process [128-130].

Because of the difficulty in dispensing underfill, 3D chip-stacking structures without underfill have also been investigated [104, 131]. Researchers have used FEA and experimental methods for examining the reliability of 3D packages with and without underfill materials. Although producing packages without underfill is typically not preferable, in some cases, reliability appears to be acceptable. For example, Kohara et al. have shown that samples with a thin die (thickness of 50 μm or 70 μm , chip area of 7.3 mm by 7.3 mm) connected to a silicon interposer by 40 μm pitch solder joints could survive 1000 thermal cycles even without underfill. However, with a thick die (thickness of 725 μm with the same chip area), the parts failed shortly after the test, but the parts with underfill passed. The results obtained from FE simulation are consistent with those obtained from the reliability test [131]. Therefore, experiments must be performed for carefully evaluating reliability, and numerical simulations are also suggested.

5.3. Wafer-to-Wafer Interconnection

Unlike chip-to-chip or chip-to-wafer stacking, the wafer-to-wafer process is completely performed at the wafer level, and only one singulation process is performed after all wafer-stacking steps have been completed. In this respect, the wafer-to-wafer process exhibits high manufacturing throughput. However, an issue associated with the wafer-to-wafer approach is yield. As there is no method available to cherry-pick the known good

dies (KGDs), the yield for wafer-to-wafer stacking is lower than that of chip-to-chip or chip-to-wafer stacking, and the yield decreases with increasing number of stacked layers. The cost-effectiveness of wafer-to-wafer stacking has been analyzed and compared with that of the chip-to-wafer approach [132, 133]. On one hand, the analysis in [133] shows that either chip-to-wafer or wafer-to-wafer stacking might be more cost-effective, depending on chip area and production volume; on the other hand, for the wafer-to-wafer approach, low yield could significantly increase the cost, caused by the loss of good dies, especially for large chips [134].

Owing to the wafer dimension, dispensing underfill into the narrow gaps between wafers is very difficult, if not impossible. Even after wafer dicing, filling underfill into the narrow gaps inside the chip stacks is still challenging (Sec. 5.2.3.). Thus, recent studies of wafer-to-wafer interconnection focus on processes using simultaneous underfill or techniques that do not necessitate underfill [135].

5.3.1. With Simultaneous Underfill

The simultaneous underfill approach is an emerging technology, which has attracted the attention of several researchers. Once the bonding process is completed, the gap between wafers is simultaneously occupied by the filled materials, and the filled materials act as a stress-redistribution layer for alleviating the reliability risk at the electrical joints. Depending on the interconnection structure and TSV formation process, wafer-to-wafer bonding with simultaneous underfill can be primarily divided into two categories: One is the metal bump interconnection with an adhesive or a polymer as simultaneous underfill,

and the other is adhesive bonding, followed by TSV formation, which is supported by the Wafer-on-Wafer (WOW) Alliance (also known as the WOW approach).

Hybrid bonding combines the interconnection of metal bumps with the simultaneous attachment of adhesive between wafers. Therefore, the adhesive acts as both a bonding material and an “underfill.” Hybrid bonding is advantageous in that old equipment and knowledge for creating metal-to-metal joints can be applied to this new method. Ko and Chang et al. have reported wafer-to-wafer hybrid bonding with CuSn and benzocyclobutene (BCB) [136, 137], and Figure 5-12 shows the process flow. Cu bumps were formed on the top wafer, and CuSn bumps were fabricated on the bottom wafer. Then, the BCB adhesive was applied to both wafers by spin-coating and lithography, followed by post-lithographic treatment for cleaning the bump surface. Bonding was carried out at 250 °C. Wafer thinning and backside metallization were conducted after bonding. Unlike other wafer-handling processes that require temporary bonding to a silicon or glass carrier, this approach features a carrier-less wafer-handling process, which can simplify the process flow. Figure 5-13 shows the cross-sectional scanning electron microscope (SEM) images showing the TSVs and micro-bumps.

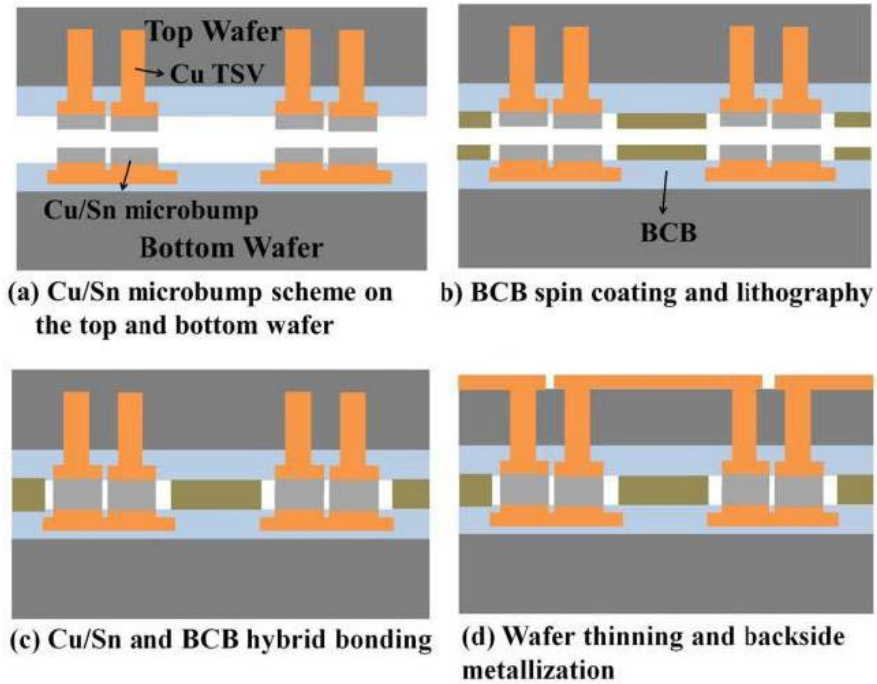


Figure 5-12 Schematic of the process flow of wafer-to-wafer hybrid bonding [136]

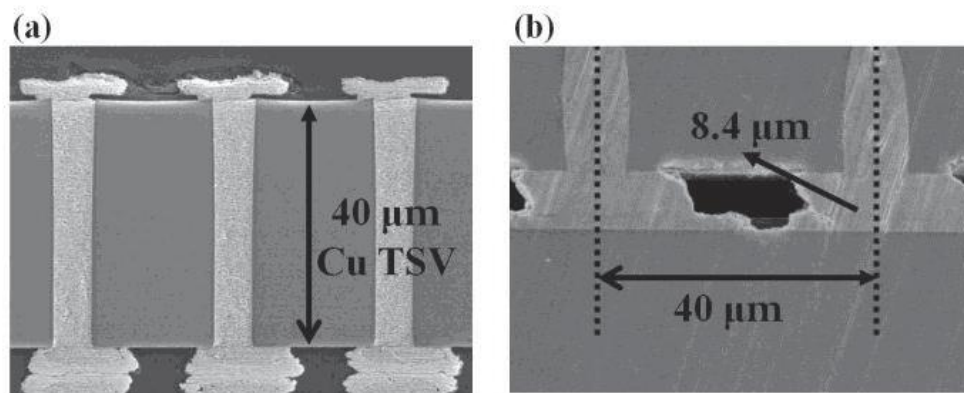


Figure 5-13 Cross-sectional images of TSVs and micro-bumps [137]

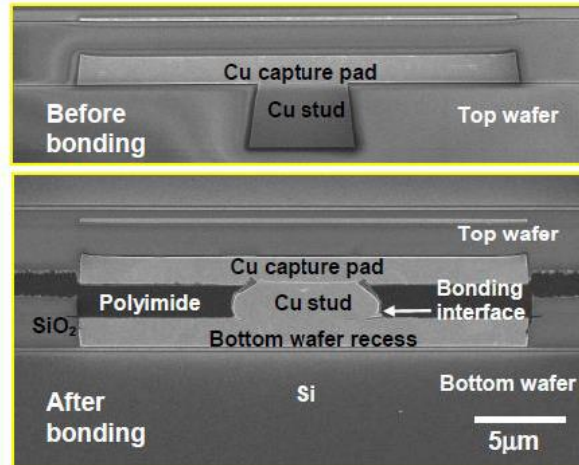


Figure 5-14 SEM cross-sectional image of the joint structure before (top) and after bonding (bottom) [138]

In addition to forming interconnections with eutectic solder materials, the Cu–Cu [117, 138-140] or Au–Au [129, 130] connection process with an adhesive (also known as transfer-join process or TJ) has also been developed. IBM researchers have fabricated joints with a mechanical lock-and-key structure using this process. In the structure shown in Figure 5-14, a Cu stud was made on the top wafer, and a recess was made on the bottom wafer. A polyimide (PI) layer was coated on the top wafer. After the PI on the Cu studs was removed, the wafers were aligned and bonded by thermocompression in vacuum.

Hybrid bonding, similar to several commonly used packaging methods, utilizes metal bumps for interconnection. These metal bumps are not only part of the electrical circuit but also an important mechanical structure providing support and enduring stresses and strains. The bump structure is a potential failure location under mechanical or thermomechanical loading. Adhesive bonding followed by TSV formation is a low-

temperature, bumpless process. This process is also referred to as WOW because of the support of the Wafer-on-Wafer alliance. Figure 5-15 shows the difference between a bump-based joint and a bumpless joint.

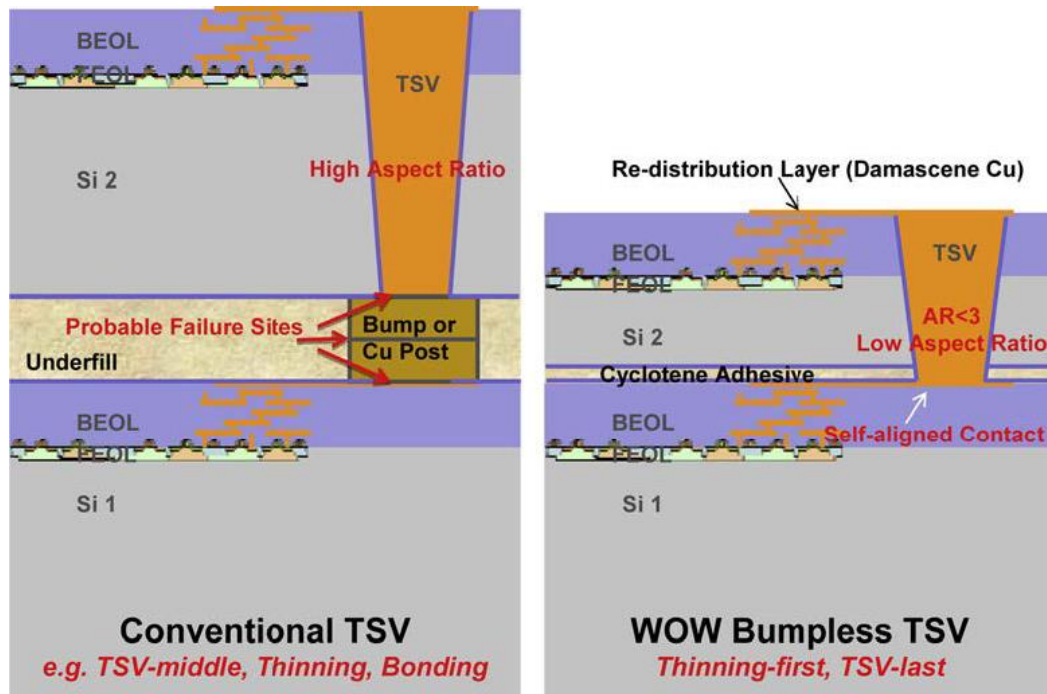


Figure 5-15 Comparison of the conventional joint structure and the WOW bumpless structure [141]

Several technical papers have reported fabrication with WOW technology, and electrical and mechanical properties have also been studied [141-143]. Figure 5-16 shows a detailed schematic of the process. First, the wafer is temporarily bonded to the support glass wafer, followed by thinning. Typically, the wafer is thinned down to less than 20 μm or even 10 μm . Then, the wafer is bonded with a BCB/cycloteneTM adhesive, and TSV etching and filling are then performed. Figure 5-17 shows stacked wafers with TSV fabricated by this process.

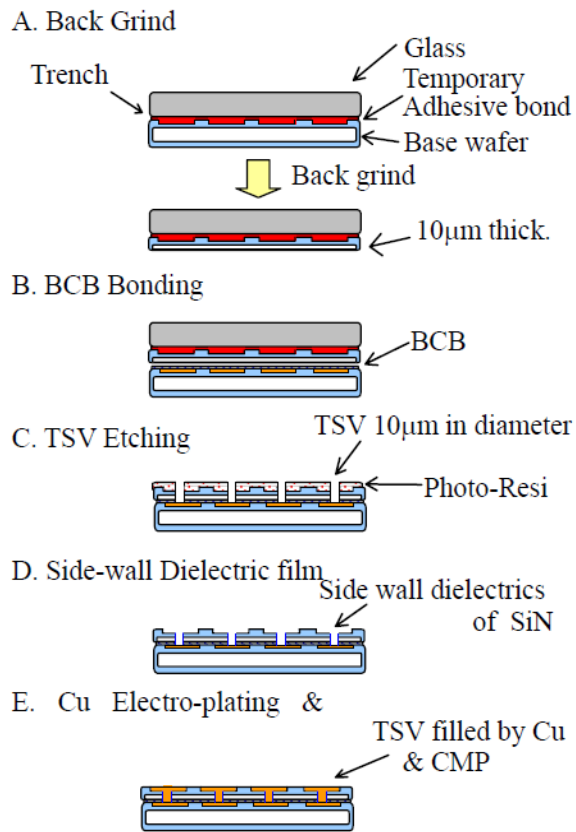


Figure 5-16 Process flow of the WOW bumpless interconnection technology [142]

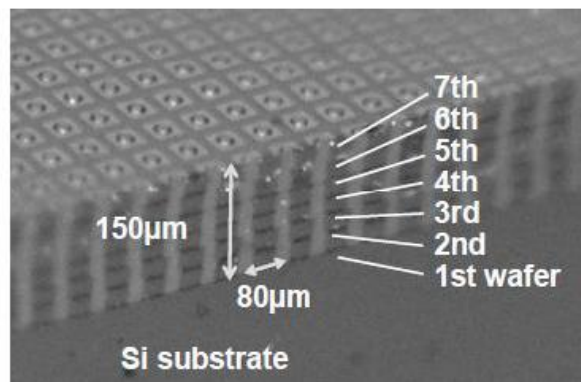


Figure 5-17 A seven-layer wafer-stacking structure using the WOW process [143]

5.3.2. Without Underfill

Underfill is applied to fill the gaps between Si chips or wafers for enhancing the reliability of electronic packages. If two wafers with active circuits can be directly bonded together without any gap, there is no need for underfill. For example, silicon direct bonding is a technology that directly puts two wafers into contact by the fusion of either Si-Si or Si-SiO₂-Si. The bonding surface of the wafers must be very flat and clean. Bonding can be conducted at room temperature, but high-temperature (above 800 °C) annealing is required to formulate strong covalent bonds at the interface. Low-temperature solutions can be obtained by activating the wafer surface using wet chemical or plasma before bonding [118, 144]. Three-dimensional integration using silicon direct bonding has been studied by organizations such as IBM and Freescale. Face-to-face and face-to-back joining are both applicable [145-148]. Figure 5-18 shows the schematic of a face-to-back joining process for stacking a silicon-on-insulator (SOI) wafer to another wafer based on the IBM platform. First, the top wafer is temporally attached to a carrier glass wafer and then thinned down, aligned, and bonded to the bottom wafer, while the bottom wafer typically remains at full thickness for supporting the stacking structure. After bonding, the TSVs are formed through the thinned wafer for creating electrical paths. Figure 5-19 shows the SEM image of a four-layer stack fabricated by bonding via SiO₂ fusion, and Figure 5-20 shows the cross-sectional SEM image showing the TSV. In addition to the TSV-last option in Figure 5-18, simultaneously creating metal-to-metal interconnections by wafer bonding has also been proven to be experimentally feasible [65, 149, 150].

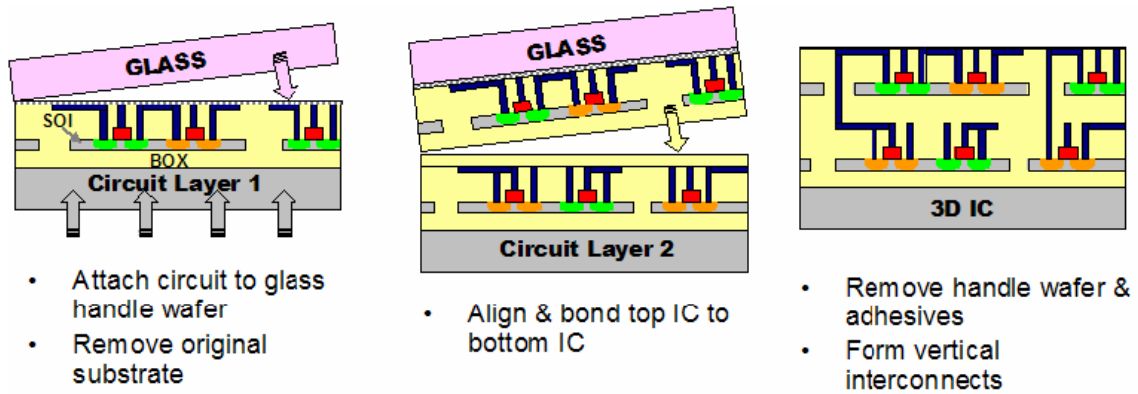


Figure 5-18 Schematic of bonding an SOI wafer to the bottom wafer based on the IBM platform [146]

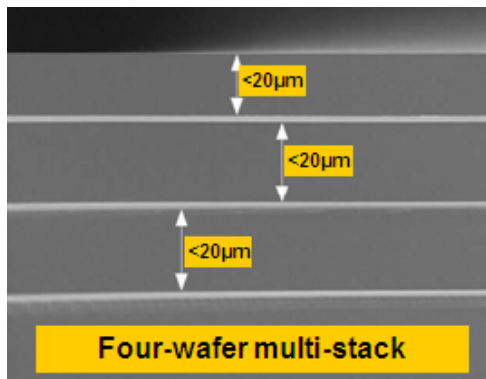


Figure 5-19 SEM image of a four-layer stack fabricated with SiO_2 fusion bonding [147]

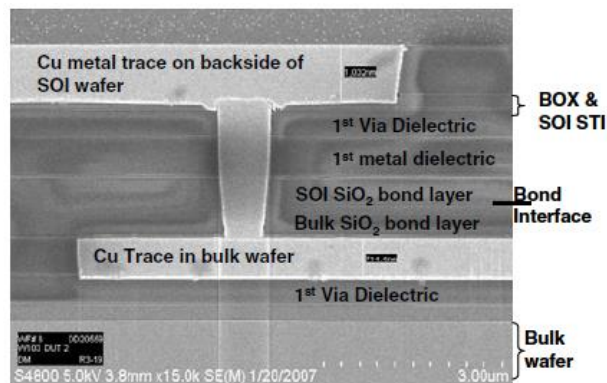


Figure 5-20 SEM cross-sectional image showing a TSV connecting two bonded wafers [148]

5.4. Summary

This chapter summarizes the state-of-the-art technologies in chip-to-chip, chip-to-wafer, and wafer-to-wafer interconnection schemes. Different interconnection structures with different fabrication processes are compared. In chip-to-chip and chip-to-wafer stacking, several flip-chip packaging technologies have been applied to 2.5D and 3D processes, and various innovational approaches have been explored: bump formation, low-temperature assembly process, flux cleaning, and underfill dispensing. At the wafer-to-wafer level, technologies such as silicon or oxide fusion, wafer-on-wafer adhesive bonding with the via-last approach, and hybrid bonding using metallic interconnection with adhesive have been developed. Regardless of the fabrication and assembly of TSVs, wafer thinning is commonly performed in wafer-level processes, and thin-wafer handling techniques have been extensively investigated. Although each interconnection method listed in this article has its advantages and drawbacks, all of the 3D packaging technologies share a common goal: to productively and cost-effectively create reliable, high-density interconnections for 3D applications.

Chapter 6. TSV Technology in MEMS Packaging

6.1. Uniqueness of 3D Packaging for MEMS Application

In recent years, TSV technology has reshaped the packaging of electronic devices. By providing a vertical electrical connection completely passing through a silicon die, this technology can help in reducing the length of the connection path and the size of electronic packages. As the industry has a high demand for performance and miniaturization, three-dimensional (3D) integration using TSV has attracted attention from both industry and academia.

However, several obstacles are observed for 3D packaging. One major challenge for 3D integrated circuits (IC) is thermal management. High-density circuits in a chip stack can generate a large amount of heat caused by Joule heating, which leads to thermomechanical stress and atomic migration; both these factors may cause reliability issues [80].

Fortunately, TSV-based 3D packaging technology can be relatively easier to implement in devices that do not generate excessive amounts of heat. Examples include memories, silicon interposers (“2.5D packaging”), and microelectromechanical system (MEMS) products. For instance, MEMS sensors have low power consumption; hence, thermal management for MEMS is significantly easier. In addition, MEMS devices typically do

not have a large number of I/Os; in addition, they typically have only two or three dies if there is only one sensor in the package, making it possible to fabricate only a few TSVs using a low aspect ratio. Therefore, adopting TSV as a method of interconnection in MEMS is feasible from a process viewpoint.

6.1.1. Typical Structure of MEMS Sensor Packages

Figure 4-3 shows the structure of a typical MEMS sensor package. Two dies are present in the package: MEMS die and application specific IC (ASIC) die. A cap is used for sealing the microstructures on the MEMS surface; it does not necessarily have an electrical connection. Wire bonding is used for building the electrical interconnection between MEMS, ASIC, and the substrate because it permits high flexibility in design. The MEMS and ASIC die can exhibit a side-by-side or stacked configuration if the die size is appropriate. Molding is often utilized for protecting the dies and bonding wires. Alternatively, a cavity package can be built, which uses a lid, not the mold, as an enclosure method for providing protection to the internal components.

6.1.2. Stacking Schemes for 3D MEMS Packaging

Several methods exist for interconnecting dies in an MEMS package if TSV can be fabricated through dies between the MEMS and ASIC. Different integration schemes have been discussed in Ref. [151]. One of the promising schemes is to flip the MEMS die and create a direct electrical connection to the ASIC using several pairs of nodes that connect with each other. A metal ring is applied on the peripheral regions of the die for hermetic sealing. TSVs are fabricated through the ASIC die, and the solder bumps are

made on the bottom of the ASIC as second-level interconnection. Figure 6-1 shows a schematic of this interconnect structure. CMOS IC die functions as the MEMS cap. Compared with a conventional packaging scheme, this method does not require any extra capping, which is significantly advantageous. In addition, wafer-to-wafer (W2W) bonding becomes possible, which can enhance manufacturing throughput.

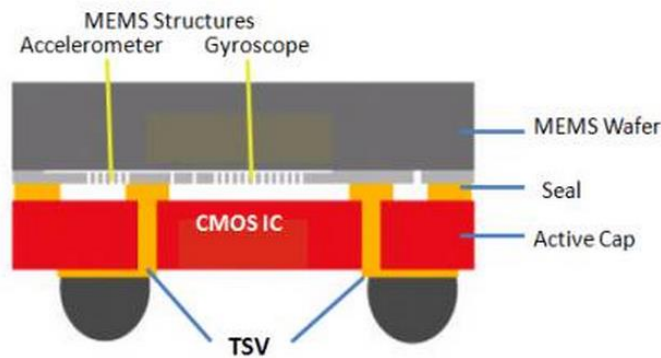


Figure 6-1 Schematic of the cross-sectional image of the MEMS sensor with TSVs through the CMOS IC die [152]

6.2. Reliability of TSV

The reliability of interconnections is crucial to the electronic product. During fabrication and usage, dies experience temperature changes. Because different materials in the package have different coefficients of thermal expansion (CTE), stress can develop in the TSVs caused by either the local CTE mismatch between a silicon die and via-filling materials or the global deformation of the package, which is also a result of CTE mismatch.

Several TSVs are being adopted for various applications, and the reliability challenges can be different in each case. Identifying the risk sites and studying the factors that affect

these risks is necessary for design. Finite element analysis (FEA) has been employed for this task. For example, Liu [153] and Lu [72] have analyzed the stress and crack driving force with several via design parameters. Moreover, several other via types have been developed, and their reliabilities have to be verified.

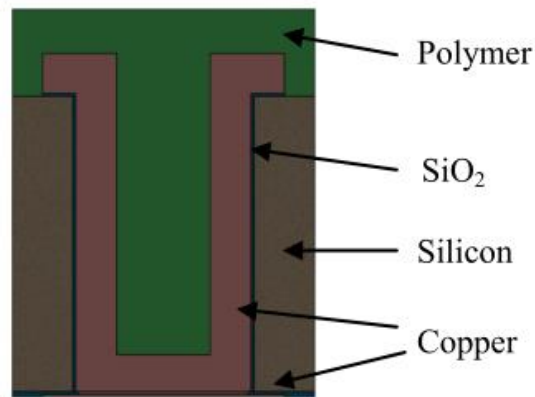


Figure 6-2 Schematic of a TSV structure

In this research, a MEMS package having a structure similar to that shown in Figure 6-1 was studied. The model included an ASIC die, a MEMS die, TSVs, metal sealing rings, solder balls, and PCB. Some details such as the combs of the accelerometer on the MEMS die surface were neglected in the model. The geometry dimensions were based on the package information in Refs. [154-156], including package size and package thickness. The thickness of the ASIC die was 100 μm . The aspect ratio of the via was 5:3. The TSV thickness was referred to the one in Ref. [154]. The cavity in the TSV was filled by a polymer. The solder bumps and metal nodes were on the “top” and “bottom” sides, respectively, in Figure 6-2, to make interconnection with the MEMS die.

Such a TSV has a half-open structure with a Cu layer covering the side wall and “bottom” of the TSV, and the cavity is filled by a polymer. Hence, the corners are the most critical location for the Cu layer, shown in Figure 6-3. The reliability risk can be affected by either the thickness of the Cu layer or material property of the polymer. The height and diameter were maintained constant during the study because it is not practical to consider such a major redesign on dies and package.

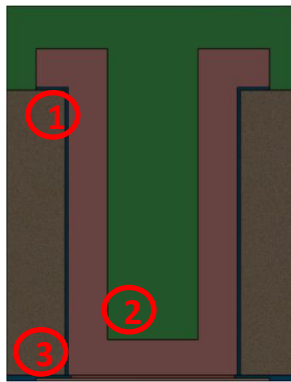


Figure 6-3 Schematic showing the critical location for TSV

6.2.1. Effect of the Polymer Material Properties: CTE and Young's Modulus

Table 6-1 shows the material properties used for simulation, except for the filling polymer. For investigating the effect of polymer material properties on the reliability of TSV, parametric studies on CTE and Young's modulus, which are key material parameters affecting the thermomechanical stresses of TSV, were performed for the TSV model. Figure 6-4 shows the variation in the TSV stresses with change in the CTE and Young's modulus of the polymer. Stresses at three corners are separately plotted. The

CTE ranges from 25 ppm to 100 ppm, and the Young's modulus ranges from 2.3 GPa to 9.2 GPa.

For corner #1, it is easy to conclude that the best combination is low CTE and low modulus for low TSV stress. However, the actual material may not simultaneously exhibit both these properties. Practically speaking, a material with low CTE typically exhibits high Young's modulus (hard), and vice versa. In this sense, in the plot of each corner in Figure 6-5, a diagonal line can be drawn along the surface, which is denoted by circles. In fact, this diagonal line can indicate the change in the stresses corresponding from one material with a CTE and Young's modulus of 100 ppm and 2.3 GPa, respectively, to another material with a CTE and Young's modulus of 30 ppm and 8.7 GPa, respectively. Figure 6-5 shows the comparison of these diagonal lines for the three corners. As can be observed in Figure 6-5, corner #1 is the most sensitive to the change in the material, and it is the most risky site. Corners #2 and #3 exhibit marginal differences with change in the polymer material.

Table 6-1 Material properties for TSV stress simulation

Material	Young's Modulus (GPa)	Poisson's Ratio	CTE (ppm/°C)
Silicon	$E_x=E_y=169; E_z=130$ $G_{xy}=50.8; G_{yz}=G_{xz}=79.5$	$\nu_{xy}=0.062$ $\nu_{yz}=\nu_{xz}=0.36$	2.6
SiO ₂	75	0.17	0.5
Al	69	0.35	22.2
Copper	110	0.35	16.4

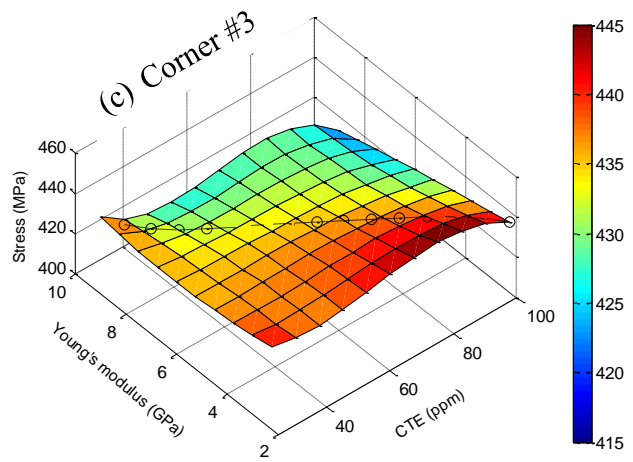
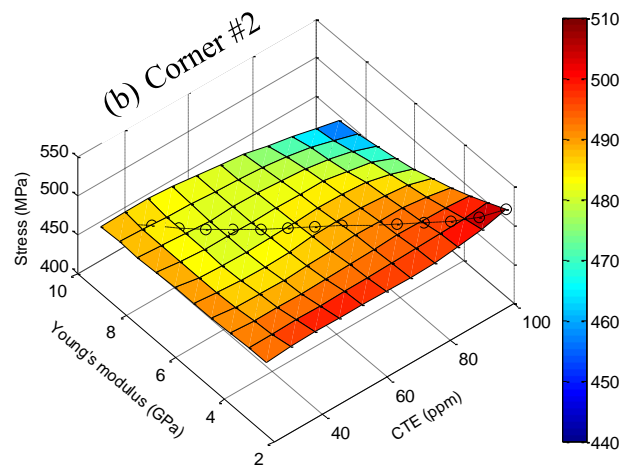
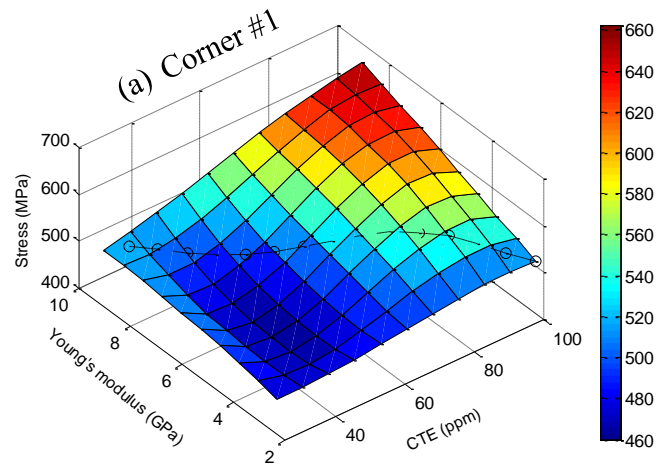


Figure 6-4 Effect of CTE and Young's modulus of the TSV polymer on TSV stress at three critical locations

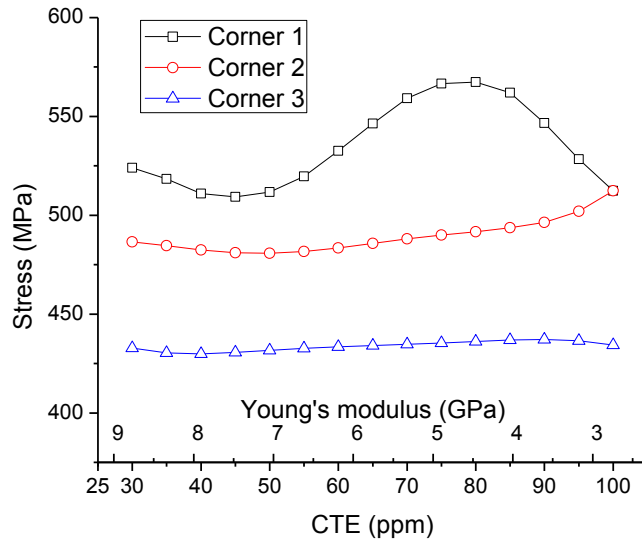


Figure 6-5 Effect of Young's modulus on the von Mises stress at the critical locations

6.3. Summary

We quantitatively compared the effect of different filling materials on the stress at critical locations for Cu TSVs used in MEMS packages. Results show that the upper corner of the TSV, which is the joint location of the side wall and the trace that connects to the solder bump, is typically more sensitive to properties of filling materials. Generally, small CTE and Young's modulus decrease the stress at the inner corners. However, in reality, low CTE materials typically exhibit higher modulus, and vice versa. In addition, the stress at different locations may exhibit different trends with changes in the materials, especially for TSV with a complex structure; hence, the most critical location might be changeable. For these reasons, it is imperative to evaluate the design of each structure and candidate material case by case.

Chapter 7. Closure

Stress is an issue critical for MEMS packaging. On the one hand, stresses on the die lead to a signal offset, a phenomena that particularly affects MEMS and some analog devices. On the other hand, stresses, especially those on the interconnections, cause mechanical failure, which is a challenge to almost all types of packages.

The research described in this dissertation focuses on studying the stresses induced in MEMS packaging by computational modeling techniques. Both die stress and interconnection stress were studied.

For overmolded packages, the die stress is significantly affected by the molding compound, which encapsulates the die. The epoxy-based molding compound exhibits materials characteristics which are affected by temperature and moisture. For comprehensively investigating the effect of temperature and moisture on packaging stress, the thermomechanical stress was studied first using a viscoelastic material model. Results show that packaging stress is dependent on environmental temperature, cooling rate, and time. The cooling rate at the glass transition temperature considerably affects the cooling rate at other temperature ranges. Besides, simulation techniques and measurement methods for the diffusion of moisture are introduced and compared. For simulating the diffusion of moisture, the direct concentration approach [41] was found to be incorrect by

verification and theoretical proof. Analysis involving both moisture and temperature was performed using coupled-field elements, and the effect of moisture on viscoelasticity was implemented using a customized APDL code. Results have shown that moisture is a factor important for packaging stress. As compared to the parts under dry condition, those subjected to moisture exhibit a lower compressive stress on MEMS die as a result of hygroscopic swelling, and the effect of moisture on stress relaxation makes the stress even smaller.

Besides, the reliability issue caused by packaging stress is becoming more challenging. As TSV technology enables 3D packaging, it also adds stress to the interconnection structures, especially the via. In this dissertation, the risk sites on Cu-based via structures, targeted for MEMS applications, were identified. The effect of material properties on thermal stresses at the critical locations of the TSV was studied. Results indicate that the impact of the material on stress is probably dependent on location. Besides, as some material properties might be dependent on each other, the situation can be more complicated. Therefore, currently, FEA with adequate accuracy is suggested for each specific design.

Reference

- [1] Harper, C. A., 1996, *Electronic Packaging and Interconnection Handbook*, McGraw-Hill, Inc., New York, NY, USA.
- [2] Zhang, H., 2011, "Investigation of Hygroscopic Swelling Behavior of Molding Compound and its Impact on Encapsulated MEMS Packages," Ph.D. Dissertation, State University of New York at Binghamton, Binghamton, NY, USA.
- [3] Gilleo, K., 2005, *MEMS/MOEMS Packaging: Concepts, Designs, Materials, and Processes*, McGraw-Hill, Inc., New York, NY, USA.
- [4] Riley, G., 2000, "Introduction to Flip Chip: What, Why, How," <http://web.archive.org/web/20090130092400/http://flipchips.com/tutorial01.html>.
- [5] Centre for High Performance Integrated Technologies and Systems (CHIPTEC), 1997, "Tape-Automated Bonding," <http://www.eleceng.adelaide.edu.au/Personal/alsarawi/node8.html>.
- [6] Yu, D., 2008, "Dynamic responses of PCB under product level free drop impact," M.S. Thesis, State University of New York at Binghamton, Binghamton, NY, USA.
- [7] Ho, P. S., and Kwok, T., 1989, "Electromigration in Metals," *Reports on Progress in Physics*, **52**, p. 301.
- [8] Zhang, Y., Liu, Y., Liang, L., and Fan, X., 2012, "The effect of Atomic Density Gradient in Electromigration," *International Journal of Materials and Structural Integrity*, **6**(1), pp. 36-53.
- [9] Zhao, Y., Basaran, C., Cartwright, A., and Dishongh, T., 2000, "Thermomechanical behavior of micron scale solder joints under dynamic loads," *Mechanics of Materials*, **32**(3), pp. 161-173.
- [10] Gomez, J., Lin, M., and Basaran, C., 2006, "Damage Mechanics Modeling of Concurrent Thermal and Vibration Loading on Electronics Packaging," *Multidiscipline Modeling in Materials and Structures*, **2**(3), pp. 309-326.
- [11] Lall, P., Lowe, R., and Goebel, K., 2012, "Prognostication of Accrued Damage in Board Assemblies under Thermal and Mechanical Stresses," *Proc. 62nd Electronic Components and Technology Conference (ECTC)*, pp. 1475-1487.
- [12] Ardebili, H., Ee Hua, W., and Pecht, M., 2003, "Hygroscopic Swelling and Sorption Characteristics of Epoxy Molding Compounds used in Electronic Packaging,"

- IEEE Transactions on Components and Packaging Technologies, **26**(1), pp. 206-214.
- [13] Moore, G., 2006, "Chapter 7: Moore's law at 40," Understanding Moore's Law: Four Decades of Innovation, D. Brock, ed., Chemical Heritage Foundation, Philadelphia, PA, USA, pp. 67-84.
- [14] Tsai, T. C., Tsao, W. C., Lin, W., Hsu, C. L., Lin, C. L., Hsu, C. M., Lin, J. F., Huang, C. C., and Wu, J. Y., 2010, "CMP Process Development for the Via-Middle 3D TSV Applications at 28nm Technology Node," *Advanced Metallization Conference*. Albany, NY, USA.
- [15] Reinhardt, K. A., and Kern, W., 2008, *Handbook of Silicon Wafer Cleaning Technology*, William Andrew, Norwich, NY, USA.
- [16] Osada, K., 2011, "Panel Discussion: Advanced packaging and 3D Technologies," *16th Asia and South Pacific Design Automation Conference*. Yokohama, Japan.
- [17] Castoldi, L., 2012, "The MEMS Revolution," *SEMI Networking Day Italy*. Milano, Italy.
- [18] Sparks, D., 2015, "MEMS Sensor Packaging," *Sensors Expo & Conference*. San Jose, CA, USA.
- [19] Ramm, P., 2015, "Understanding Heterogeneous 3D Integration," <http://www.3dincites.com/2015/01/heterogeneous-3d-integration/>.
- [20] Li, Z., Lee, S., Lewis, B. J., Houston, P. N., Baldwin, D. F., Stout, E. A., Tessier, T. G., and Evans, J. L., 2010, "Assembly Process Development for Fine Pitch Flip Chip Silicon-to-Silicon 3D Wafer Level Integration with No Flow Underfill," *Journal of Microelectronics and Electronic Packaging*, **7**, pp. 146-151.
- [21] Zhang, X., Park, S., and Judy, M. W., 2007, "Accurate Assessment of Packaging Stress Effects on MEMS Sensors by Measurement and Sensor - Package Interaction Simulations," *Journal of Microelectromechanical Systems*, **16**(3), pp. 639-649.
- [22] Zhang, X., Park, S. B., Navarro, R., and Judy, M. W., 2006, "Accurate assessment of packaging stress effects on MEMS devices," *Proc. 10th Intersociety Conference on Thermal and Thermomechanical Phenomena in Electronics Systems (ITHERM '06)*, pp. 1336-1342.
- [23] Krondorfer, R., Kim, Y. K., Kim, J., Gustafson, C.-G., and Lommasson, T. C., 2004, "Finite element simulation of package stress in transfer molded MEMS pressure sensors," *Microelectronics Reliability*, **44**(12), pp. 1995-2002.

- [24] Krondorfer, R. H., 2003, "On Packaging of MEMS: Simulation of Transfer Moulding and Packaging Stress and Their Effect on a Family of Piezo-Resistive Pressure Sensors," Ph. D. Dissertation, Norwegian University of Science and Technology.
- [25] Krondorfer, R. H., and Kim, Y. K., 2007, "Packaging Effect on MEMS Pressure Sensor Performance," IEEE Transactions on Components and Packaging Technologies, **30**(2), pp. 285-293.
- [26] Kenner, V., Harper, B., and Itkin, V., 1997, "Stress Relaxation in Molding Compounds," Journal of Electronic Materials, **26**(7), pp. 821-826.
- [27] Chae, S.-H., Zhao, J.-H., Edwards, D., and Ho, P., 2010, "Characterization of the Viscoelasticity of Molding Compounds in the Time Domain," Journal of Electronic Materials, **39**(4), pp. 419-425.
- [28] Woodworth, L., 2010, "Characterization of Time- and Temperature-Dependent Mechanical Properties of Advanced Polymers using Bragg Grating Sensors," M. S. Thesis, University of Maryland, College Park.
- [29] Ernst, L. J., Zhang, G. Q., Jansen, K. M. B., and Bressers, H. J. L., 2003, "Time- and Temperature-Dependent Thermo-Mechanical Modeling of a Packaging Molding Compound and its Effect on Packaging Process Stresses," Journal of Electronic Packaging, **125**(4), pp. 539-548.
- [30] Kim, Y. K., Gang, J. H., and Lee, B.-Y., 2011, "Material Property Effects on Solder Failure Analyses," Microelectronics Reliability, **51**(5), pp. 985-993.
- [31] Imaoka, S., 2008, "Sheldon's ANSYS Tips on Viscoelasticity," http://ansys.net/tips_sheldon/STI0807_Viscoelasticity.zip.
- [32] Imaoka, S., 2006, "Sheldon's ANSYS Tips and Tricks: Viscoelasticity and Creep," http://ansys.net/tips_sheldon/STI0604_Viscous_Behavior.zip.
- [33] ANSYS, Inc., 2013, *ANSYS Mechanical APDL Theory Reference, Release 14.5*, Canonsburg, PA.
- [34] Gujrati, P. D., 2010, "Nonequilibrium Thermodynamics: Structural Relaxation, Fictive Temperature, and Tool-Narayanaswamy Phenomenology in Glasses," Physical Review E, **81**(5), p. 051130.
- [35] Ferry, J. D., 1980, *Viscoelastic Properties of Polymers*, Wiley, New York, NY, USA.
- [36] IPC/JEDEC, 2008, "Moisture/Reflow Sensitivity Classification for Nonhermetic Solid State Surface Mount Devices."

- [37] Crank, J., 1975, *The Mathematics of Diffusion*, Oxford University Press, London, UK.
- [38] Yoon, S., Han, B., and Wang, Z., 2007, “On Moisture Diffusion Modeling Using Thermal-Moisture Analogy,” *Journal of Electronic Packaging*, **129**(4), pp. 421-426.
- [39] Jang, C., Park, S., Han, B., and Yoon, S., 2008, “Advanced Thermal-Moisture Analogy Scheme for Anisothermal Moisture Diffusion Problem,” *Journal of Electronic Packaging*, **130**(1), p. 011004.
- [40] Sutton, M., 2012, “Moisture Diffusion Modeling with ANSYS at R14 and Beyond,” http://www.padtinc.com/blog/wp-content/uploads/oldblog/PADT-Webinar-Moisture-Diffusion-2012_05_24.pdf.
- [41] Xie, B., Fan, X. J., Shi, X. Q., and Ding, H., 2009, “Direct Concentration Approach of Moisture Diffusion and Whole-Field Vapor Pressure Modeling for Reflow Process—Part I: Theory and Numerical Implementation,” *Journal of Electronic Packaging*, **131**(3), p. 031010.
- [42] Wong, E. H., and Rajoo, R., 2003, “Moisture Absorption and Diffusion Characterization of Packaging Materials—Advanced Treatment,” *Microelectronics Reliability*, **43**(12), pp. 2087-2096.
- [43] Xie, B., Fan, X. J., Shi, X. Q., and Ding, H., 2009, “Direct Concentration Approach of Moisture Diffusion and Whole-Field Vapor Pressure Modeling for Reflow Process—Part II: Application to 3D Ultrathin Stacked-Die Chip Scale Packages,” *Journal of Electronic Packaging*, **131**(3), p. 031011.
- [44] Chen, X., Zhao, S., and Zhai, L., 2005, “Moisture Absorption and Diffusion Characterization of Molding Compound,” *Journal of Electronic Packaging*, **127**, pp. 460-465.
- [45] Zhou, J., and Law, J. S., 2008, “Effect of Non-Uniform Moisture Distribution on the Hygroscopic Swelling Coefficient,” *IEEE Transactions on Components and Packaging Technologies*, **31**(2), pp. 269-276.
- [46] Jang, C., Yoon, S., and Han, B., 2010, “Measurement of the Hygroscopic Swelling Coefficient of Thin Film Polymers Used in Semiconductor Packaging,” *IEEE Transactions on Components and Packaging Technologies*, **33**(2), pp. 340-346.
- [47] Bhargava, P., Chuang, K. C., Chen, K., and Zehnder, A., 2006, “Moisture diffusion properties of HFPE-II-52 polyimide,” *Journal of Applied Polymer Science*, **102**(4), pp. 3471-3479.
- [48] Galloway, J. E., and Miles, B. M., 1997, “Moisture Absorption and Desorption Predictions for Plastic Ball Grid Array Packages,” *IEEE Transactions on*

Components, Packaging, and Manufacturing Technology, Part A, **20**(3), pp. 274-279.

- [49] Kim, Y., Liu, D., Lee, H., Liu, R., Sengupta, D., and Park, S., 2015, "Investigation of Stress in MEMS Sensor Device due to Hygroscopic and Viscoelastic Behavior of Molding Compound," *IEEE Transactions on Components, Packaging, and Manufacturing Technology*, **5**(7), pp. 945-955.
- [50] Jang, C., Han, B., and Yoon, S., 2010, "Comprehensive Moisture Diffusion Characteristics of Epoxy Molding Compounds Over Solder Reflow Process Temperature," *IEEE Transactions on Components and Packaging Technologies*, **33**(4), pp. 809-818.
- [51] Stellrecht, E., Han, B., and Pecht, M. G., 2004, "Characterization of Hygroscopic Swelling Behavior of Mold Compounds and Plastic Packages," *IEEE Transactions on Components and Packaging Technologies*, **27**(3), pp. 499-506.
- [52] Wong, E. H., Chan, K. C., Rajoo, R., and Lim, T. B., 2000, "The Mechanics and Impact of Hygroscopic Swelling of Polymeric Materials in Electronic Packaging," *Proc. 50th Electronic Components & Technology Conference*, pp. 576-580.
- [53] Park, S., Zhang, H., Zhang, X., Ng, S. L., and Lee, H. C., 2009, "Temperature dependency of coefficient of hygroscopic swelling of molding compound," *Proc. 59th Electronic Components and Technology Conference*, pp. 172-179.
- [54] Zhou, J., Tee, T. Y., and Fan, X. J., 2010, "Hygroscopic swelling of polymeric materials in electronic packaging: characterization and analysis," *Moisture Sensitivity of Plastic Packages of IC Devices*, X. J. Fan, and E. Suhir, eds., Springer, New York, pp. 153-179.
- [55] Park, S., Dhakal, R., and Joshi, R., 2005, "Comparative Analysis of BGA Deformations and Strains Using Digital Image Correlation and Moiré Interferometry," *Proc. Society for Experimental Mechanics 2005 Annual Conference*.
- [56] Changsoo, J., Samson, Y., and Han, B., 2010, "Measurement of the Hygroscopic Swelling Coefficient of Thin Film Polymers Used in Semiconductor Packaging," *IEEE Transactions on Components and Packaging Technologies*, **33**(2), pp. 340-346.
- [57] Kwak, J. B., 2010, "Experimental assessment of electronic package deformation using optical full-field deformation measurement system," Ph.D. Dissertation, State University of New York at Binghamton.

- [58] Zhou, J., 2006, “Analytical and Numerical Bound Analysis of Hygroscopic Swelling Characterization,” *Proc. 56th Electronic Components and Technology Conference*, p. 6.
- [59] Yoon, S., Han, B., Cho, S., and Jang, C.-S., 2005, “Non-linear Finite Element Analysis for Electronic Packages Subjected to Combined Hygroscopic and Thermo-mechanical Stresses,” *Proc. 7th Electronic Packaging Technology Conference (EPTC)*, p. 6.
- [60] Liu, D., and Park, S., 2014, “A Note on the Normalized Approach to Simulating Moisture Diffusion in a Multimaterial System Under Transient Thermal Conditions Using ansys 14 and 14.5,” *Journal of Electronic Packaging*, **136**(3), pp. 034501-034501.
- [61] Fan, X., and Zhao, J.-H., 2011, “Moisture Diffusion and Integrated Stress Analysis in Encapsulated Microelectronics Devices,” *Proc. 12th International Conference on Thermal, Mechanical and Multi-Physics Simulation and Experiments in Microelectronics and Microsystems (EuroSimE)*, pp. 1/8-8/8.
- [62] Yoon, S., Jang, C., and Han, B., 2008, “Nonlinear Stress Modeling Scheme to Analyze Semiconductor Packages Subjected to Combined Thermal and Hygroscopic Loading,” *Journal of Electronic Packaging*, **130**(2), p. 024502.
- [63] Ishisaka, A., and Kawagoe, M., 2004, “Examination of the Time–Water Content Superposition on the Dynamic Viscoelasticity of Moistened Polyamide 6 and Epoxy,” *Journal of Applied Polymer Science*, **93**(2), pp. 560-567.
- [64] Walter, H., Dermitzaki, E., Wunderle, B., and Michel, B., 2010, “Influence of Moisture on Humidity Sensitive Material Parameters of Polymers used in Microelectronic Applications,” *Proc. 3rd Electronic System-Integration Technology Conference (ESTC)*, IEEE, pp. 1-5.
- [65] “Ziptronix Pioneering 3D Integrated Circuit Process Technology,” <http://www.i-micronews.com/lectureArticle.asp?id=2009>.
- [66] Ma, X., Jansen, K. M. B., and Ernst, L. J., 2006, “Moisture Effects on the Creep of Thermosetting IC Packaging Polymers,” *Proc. 7th International Conference on Thermal, Mechanical and Multiphysics Simulation and Experiments in Micro-Electronics and Micro-Systems*, pp. 1-5.
- [67] Rzepka, S., Pantou, R., Bormann, F., Bramer, B., Brabandt, I., and Michel, B., 2013, “Toolbox for Visco-Elastic Material Modeling of Smart Lightweight Structures,” *Proc. 14th International Conference on Thermal, Mechanical and Multi-Physics Simulation and Experiments in Microelectronics and Microsystems (EuroSimE)*, pp. 1-8.

- [68] O'Reilly, R., Khenkin, A., and Harney, K., 2009, "Sonic Nirvana: Using MEMS Accelerometers as Acoustic Pickups in Musical Instruments," http://www.analog.com/library/analogdialogue/archives/43-02/mems_microphones.html.
- [69] LeVeque, R. J., 2011, "High Performance Scientific Computing ", <http://faculty.washington.edu/rjl/uwamath583s11/sphinx/notes/html/#parallel-computing>.
- [70] Kim, Y., Lee, H., Zhang, X., and Park, S., 2014, "Optimal Material Properties of Molding Compounds for MEMS Package," *IEEE Transactions on Components, Packaging and Manufacturing Technology*, **4**(10), pp. 1589-1597.
- [71] Maxfield, C., 2012, "2D vs. 2.5D vs. 3D ICs 101," <http://www.eetimes.com/design/programmable-logic/4370596/2D-vs--2-5D-vs--3D-ICs-101>.
- [72] Lu, K. H., 2010, "Thermo-Mechanical Reliability of 3-D Interconnects Containing Through-Silicon-Vias (TSVs)," Ph.D. Dissertation, The University of Texas at Austin, Austin, TX, USA.
- [73] Pares, G., De Crecy, F., Moreau, S., Maurice, C., Borbely, A., Mazuir, J., Chapelon, L. L., and Sillon, N., 2011, "Assessment and Characterization of Stress Induced by Via-First TSV Technology," *Journal of Microelectronics and Electronic Packaging*, **8**, pp. 129-139.
- [74] He, R., Wang, H., Zhou, J., Guo, X., Yu, D., and Wan, L., 2011, "Nonlinear Thermo-Mechanical Analysis of TSV Interposer Filling with Solder, Cu and Cu-cored Solder," *Proc. 12th International Conference on Electronic Packaging Technology and High Density Packaging (ICEPT-HDP)*, pp. 1-4.
- [75] Lee, S. W. R., Hon, R., Zhang, S. X. D., and Wong, C. K., 2005, "3D Stacked Flip Chip Packaging with Through Silicon Vias and Copper Plating or Conductive Adhesive Filling," *Proc. 55th Electronic Components and Technology Conference (ECTC)*, pp. 795-801.
- [76] Venkatadri, V., Sammakia, B., Srihari, K., and Santos, D., 2011, "A Review of Recent Advances in Thermal Management in Three Dimensional Chip Stacks in Electronic Systems," *Journal of Electronic Packaging*, **133**(4), p. 041011.
- [77] Onkaraiah, S., and Chuan Seng, T., 2010, "Mitigating Heat Dissipation and Thermo-Mechanical Stress Challenges in 3-D IC Using Thermal Through Silicon Via (TTSV)," *Proc. 60th Electronic Components and Technology Conference (ECTC)*, pp. 411-416.

- [78] Xilinx, Inc., 2011, "Stacked & Loaded: Xilinx SSI, 28-Gnps I/O Yield Amazing FPGAs," *Xcell Journal*, **74**, pp. 9-13.
- [79] Tu, K. N., Hsiao, H.-Y., and Chen, C., 2012, "Transition from Flip Chip Solder Joint to 3D IC Microbump: Its Effect on Microstructure Anisotropy," *Microelectronics Reliability*, **51**(1), pp. 2-6.
- [80] Tu, K. N., 2011, "Reliability Challenges in 3D IC Packaging Technology," *Microelectronics Reliability*, **51**(3), pp. 517-523.
- [81] Dunne, R., Takahashi, Y., Mawatari, K., Matsuura, M., Bonifield, T., Steinmann, P., and Stepniak, D., 2012, "Development of a Stacked WCSP Package Platform Using TSV (Through Silicon Via) Technology," *Proc. 2012 IEEE 62nd Electronic Components and Technology Conference (ECTC)*, pp. 1062-1067.
- [82] Chen, Q., Zhang, D., Xu, Z., Beece, A., Patti, R., Tan, Z., Wang, Z., Liu, L., and Lu, J.-Q., 2012, "A Novel Chip-to-Wafer (C2W) Three-Dimensional (3D) Integration Approach Using a Template for Precise Alignment," *Microelectronic Engineering*, **92**, pp. 15-18.
- [83] Yu, A., Lau, J. H., Ho, S. W., Kumar, A., Hnin, W. Y., Yu, D.-Q., Jong, M. C., Kripesh, V., Pinjala, D., and Kwong, D.-L., 2009, "Study of 15 μ m Pitch Solder Microbumps for 3D IC Integration," *Proc. 59th Electronic Components and Technology Conference (ECTC)*, pp. 6-10.
- [84] Lee, C.-K., Zhan, C.-J., Lau, J. H., Huang, Y.-J., Fu, H.-C., Huang, J.-H., Hsiao, Z.-C., Chen, S.-W., Huang, S.-Y., Fan, C.-W., Lin, Y.-M., Kao, K.-S., Ko, C.-T., Chen, T.-H., Lo, R., and Kao, M. J., 2012, "Wafer Bumping, Assembly, and Reliability Assessment of μ bumps with 5 μ m Pads on 10 μ m Pitch for 3D IC Integration," *Proc. 62nd Electronic Components and Technology Conference (ECTC)*, pp. 636-640.
- [85] Au, K. Y., Beleran, J. D., Yang, Y. B., Zhang, Y. F., Kriangsak, S. L., Wilson, P. L. O., Drake, Y. S. K., Toh, C. H., and Surasit, C., 2011, "Thru Silicon Via Stacking & Numerical Characterization for Multi-Die Interconnections Using Full Array & Very Fine Pitch Micro C4 Bumps," *Proc. 61st Electronic Components and Technology Conference (ECTC)*, pp. 296-303.
- [86] Au, K. Y., Kriangsak, S. L., Zhang, X. R., Zhu, W. H., and Toh, C. H., 2010, "3D Chip Stacking & Reliability Using TSV-Micro C4 Solder Interconnection," *Proc. 60th Electronic Components and Technology Conference (ECTC)*, pp. 1376-1384.
- [87] Dang, B., Wright, S. L., Andry, P. S., Sprogis, E. J., Tsang, C. K., Interrante, M. J., Webb, B. C., Polastre, R. J., Horton, R. R., Patel, C. S., Sharma, A., Zheng, J., Sakuma, K., and Knickerbocker, J. U., 2008, "3D Chip Stacking with C4 Technology," *IBM Journal of Research and Development*, **52**(6), pp. 599-609.

- [88] Maria, J., Dang, B., Wright, S. L., Tsang, C. K., Andry, P., Polastre, R., Liu, Y., Wiggins, L., and Knickerbocker, J. U., 2011, "3D Chip Stacking with 50 μm Pitch Lead-Free Micro-C4 Interconnections," *Proc. 61st Electronic Components and Technology Conference (ECTC)*, pp. 268-273.
- [89] Patterson, D. S., 2012, "2.5D/3D Packaging Enablement through Copper Pillar Technology," *Chip Scale Review*, **16**(3), pp. 20-26.
- [90] Farooq, M. G., Graves-Abe, T. L., Landers, W. F., Kothandaraman, C., Himmel, B. A., Andry, P. S., Tsang, C. K., Sprogis, E., Volant, R. P., Petrarca, K. S., Winstel, K. R., Safran, J. M., Sullivan, T. D., Chen, F., Shapiro, M. J., Hannon, R., Liptak, R., Berger, D., and Iyer, S. S., 2011, "3D Copper TSV Integration, Testing and Reliability," *Proc. 2011 IEEE International Electron Devices Meeting (IEDM)*, pp. 7.1.1-7.1.4.
- [91] Busby, J., Dang, B., Gruber, P., Hawken, D., Shah, J., Weisman, R., Perfecto, E., Ruhmer, K., and Buchwalter, S., 2008, "C4NP Lead Free Solder Bumping and 3D Micro Bumping," *Proc. IEEE/SEMI Advanced Semiconductor Manufacturing Conference (ASMC 2008)* pp. 333-339.
- [92] Shih, D. Y., Dang, B., Gruber, P., Lu, M., Kang, S., Buchwalter, S., Knickerbocker, J., Perfecto, E., Garant, J., Knickerbocker, S., Semkow, K., Sundlof, B., Busby, J., Weisman, R., Ruhmer, K., and Hughlett, E., 2008, "C4NP for Pb-free Solder Wafer Bumping and 3D Fine-Pitch Applications," *Proc. International Conference on Electronic Packaging Technology & High Density Packaging (ICEPT-HDP)*, pp. 1-7.
- [93] Mathewson, A., Brun, J., Ponthenier, G., Franiatte, R., Nowodzinski, A., Sillon, N., Poupon, G., Deputot, F., and Dubois-Bonvalot, B., 2007, "Detailed Characterisation of Ni Microinsert Technology For Flip Chip Die on Wafer Attachment," *Proc. 57th Electronic Components and Technology Conference (ECTC)*, pp. 616-621.
- [94] Mathewson, A., Brun, J., Puget, C., Franiatte, R., Sillon, N., Depoutot, F., and Dubois-Bonvalot, B., 2006, "Microstructured Interconnections for High Security Systems," *Proc. 1st Electronics Systemintegration Technology Conference*, pp. 126-132.
- [95] Poupon, G., Sillon, N., Henry, D., Gillot, C., Mathewson, A., Di Cioccio, L., Charlet, B., Leduc, P., Vinet, M., and Batude, P., 2009, "System on Wafer: A New Silicon Concept in SiP," *Proceedings of the IEEE*, **97**(1), pp. 60-69.
- [96] Park, S.-H., Lee, K.-Y., Won, H.-J., Oh, T.-S., and Kim, Y.-H., 2007, "Flip Chip Process Using Mushroom Bumps and Interlocking Bumps," *Proc. 40th International Symposium on Microelectronics (IMAPS)* pp. 723-727.

- [97] Oh, T. S., Lee, K.-Y., and Won, H.-J., 2009, "Flip-Chip Process Using Interlocking-Bump Joints," *IEEE Transactions on Components and Packaging Technologies*, **32**(4), pp. 909-914.
- [98] Jang, D. M., Ryu, C., Lee, K. Y., Cho, B. H., Kim, J., Oh, T. S., Lee, W. J., and Yu, J., 2007, "Development and Evaluation of 3-D SiP with Vertically Interconnected Through Silicon Vias (TSV)," *Proc. 57th Electronic Components and Technology Conference (ECTC)*, pp. 847-852.
- [99] Souriau, J. C., Castagne, L., Liotard, J., Inal, K., Mazuir, J., Le Texier, F., Fresquet, G., Varvara, M., Launay, N., Dubois, B., and Malia, T., 2012, "3D Multi-Stacking of Thin Dies Based on TSV and Micro-Inserts Interconnections," *Proc. 62nd Electronic Components and Technology Conference (ECTC)*, pp. 1047-1053.
- [100] Nowodzinski, A., Boutry, H., Franiatte, R., Mandrillon, V., Anciant, R., Verrun, S., and Simon, G., 2012, "Reliability Tests on Micro-Insert Die Bonding Technology," *Proc. International Semiconductor Conference Dresden-Grenoble (ISCDG)*, pp. 83-87.
- [101] Ebersberger, B., and Lee, C., 2008, "Cu Pillar Bumps as a Lead-Free Drop-in Replacement for Solder-Bumped, Flip-Chip Interconnects," *Proc. 58th Electronic Components and Technology Conference (ECTC)*, pp. 59-66.
- [102] Lee, C. H., 2009, "Interconnection with Copper Pillar Bumps : Process and Applications," *Proc. IEEE International Interconnect Technology Conference (IITC)*, pp. 214-216.
- [103] Chang, J. Y., Cheng, R. S., Kao, K. S., Chang, T. C., and Chuang, T. H., 2012, "Reliable Microjoints Formed by Solid-Liquid Interdiffusion (SLID) Bonding Within a Chip-Stacking Architecture," *IEEE Transactions on Components, Packaging and Manufacturing Technology*, **2**(6), pp. 979-984.
- [104] Sa, Y.-K., Yoo, S., Shin, Y.-S., Han, M.-K., and Lee, C.-W., 2010, "Joint Properties of Solder Capped Copper Pillars for 3D Packaging," *Proc. 60th Electronic Components and Technology Conference (ECTC)*, pp. 2019-2024.
- [105] Lee, J., Fernandez, D. M., Paing, M., Yeo, Y. C., and Gao, S., 2012, "Electroless Ni Plating to Compensate for Bump Height Variation in Cu-Cu 3-D Packaging," *IEEE Transactions on Components, Packaging and Manufacturing Technology*, **2**(6), pp. 964-970.
- [106] Tang, Y.-S., Chang, Y.-J., and Chen, K.-N., 2012, "Wafer-level Cu-Cu Bonding Technology," *Microelectronics Reliability*, **52**(2), pp. 312-320.
- [107] Miller, L. F., 1969, "Controlled Collapse Reflow Chip Joining," *IBM J. Res. Dev.*, **13**.

- [108] Kripesh, V., Wong Wai, K., and Iyer, M., 2003, "Ultra-Fine Pitch Pb-free & Eutectic Solder Bumping with Fine Particle Size Solder Paste for Nano Packaging," *Proc. 5th Electronics Packaging Technology Conference (EPTC 2003)*, pp. 732-737.
- [109] Gan, H., Wright, S. L., Polastre, R., Buchwalter, L. P., Horton, R., Andry, P. S., Patel, C., Tsang, C., Knickerbocker, J., Sprogis, E., Pavlova, A., Kang, S. K., and Lee, K. W., 2006, "Pb-free Microjoints (50 μm Pitch) for the Next Neneration Microsystems: the Fabrication, Assembly and Characterization," *Proc. 56th Electronic Components and Technology Conference (ECTC)*, p. 6.
- [110] Dang, B., Shih, D.-Y., Buchwalter, S., Tsang, C., Patel, C., Knickerbocker, J., Gruber, P., Knickerbocker, S., Garant, J., Semkow, K., Ruhmer, K., and Hughlett, E., 2008, "50 μm Pitch Pb-Free Micro-Bumps by C4NP Technology," *Proc. 58th Electronic Components and Technology Conference (ECTC)*, pp. 1505-1510.
- [111] Yin, W., Yu, D., Dai, F., Song, C., Bo, Z., Wan, L., Yu, H., and Sun, J., 2012, "Development of Micro-Alloying Method for Cu Pillar Solder Bump by Solid Liquid Interaction," *Proc. 62nd Electronic Components and Technology Conference (ECTC)*, pp. 1709-1714.
- [112] Zhan, C.-J., Chuang, C.-C., Juang, J.-Y., Lu, S.-T., and Chang, T.-C., 2010, "Assembly and Reliability Characterization of 3D Chip Stacking with 30 μm Pitch Lead-free Solder Micro Bump Interconnection," *Proc. 60th Electronic Components and Technology Conference (ECTC)*, pp. 1043-1049.
- [113] Ma, S., Sun, X., Zhu, Y., Zhu, Z., Cui, Q., Chen, M., Xiao, Y., Chen, J., Miao, M., Lu, W., and Jin, Y., 2012, "Design and Process Development of a Stacked SRAM Memory Chip Module with TSV Interconnection," *Proc. 62nd Electronic Components and Technology Conference (ECTC)*, pp. 1925-1929.
- [114] Bae, H.-C., Choi, K.-S., Eom, Y.-S., Lim, B.-O., Sung, K.-J., Jung, S., Kim, B.-G., Kang, I.-S., and Moon, J.-T., 2010, "3D SiP Module Using TSV and Novel Solder Bump Maker," *Proc. 60th Electronic Components and Technology Conference (ECTC)*, pp. 1637-1641.
- [115] Sung, K.-J., Choi, K.-S., Bae, H.-C., Kwon, Y.-H., and Eom, Y.-S., 2012, "Novel Bumping and Underfill Technologies for 3D IC Integration," *ETRI Journal*, **34**(5), pp. 706-712.
- [116] Sung, K.-J., Choi, K.-S., Lim, B.-O., Bae, H.-C., Choo, S.-W., Moon, J.-T., Kwon, Y. H., Nam, E. S., and Eom, Y.-S., 2010, "Solder Bump Maker with Coining Process on TSV Chips for 3D Packages," *Proc. 11th International Conference on Electronic Packaging Technology & High Density Packaging (ICEPT-HDP)*, pp. 185-189.

- [117] Xie, Y., Cong, J. J., and Sapatnekar, S., 2010, "3D Process Technology Considerations," *Three-Dimensional Integrated Circuit Design: EDA, Design and Microarchitectures*, Springer, New York, NY, USA.
- [118] Ko, C.-T., and Chen, K.-N., 2012, "Low Temperature Bonding Technology for 3D Integration," *Microelectronics Reliability*, **52**(2), pp. 302-311.
- [119] Morinaga, E., Oka, Y., Nishimori, H., Miyagawa, H., Satoh, R., Iwata, Y., and Kanezaki, R., 2012, "Study of Low Temperature and High Heat-Resistant Fluxless Bonding via Nanoscale Thin Film Control Toward Wafer-Level Multiple Chip Stacking for 3D LSI," *Proc. 62nd Electronic Components and Technology Conference (ECTC)*, pp. 14-19.
- [120] Xie, L., Choi, W. K., Premachandran, C. S., Selvanayagam, C. S., Bai, K. W., Zeng, Y. Z., Ong, S. C., Liao, E., Khairyanto, A., Sekhar, V. N., and Thew, S., 2011, "Design, Simulation and Process Optimization of AuInSn Low Temperature TLP Bonding for 3D IC Stacking," *Proc. 61st Electronic Components and Technology Conference (ECTC)*, pp. 279-284.
- [121] Agarwal, R., Zhang, W., Limaye, P., Labie, R., Dimcic, B., Phommahaxay, A., and Soussan, P., 2010, "Cu/Sn Microbumps Interconnect for 3D TSV Chip Stacking," *Proc. 60th Electronic Components and Technology Conference (ECTC)*, pp. 858-863.
- [122] Zhang, W., Limaye, P., Civale, Y., Labie, R., and Soussan, P., 2010, "Fine Pitch Cu/Sn Solid State Diffusion Bonding for Making High Yield Bump Interconnections and Its Application in 3D Integration," *Proc. 3rd Electronic System-Integration Technology Conference (ESTC)*, pp. 1-4.
- [123] Sakuma, K., Sueoka, K., Kohara, S., Matsumoto, K., Noma, H., Aoki, T., Oyama, Y., Nishiwaki, H., Andry, P. S., Tsang, C. K., Knickerbocker, J. U., and Orii, Y., 2010, "IMC Bonding for 3D Interconnection," *Proc. 2010 Electronic Components and Technology Conference (ECTC)*, pp. 864-871.
- [124] Zhang, Z., and Wong, C. P., 2004, "Recent Advances in Flip-Chip Underfill: Materials, Process, and Reliability," *IEEE Transactions on Advanced Packaging*, **27**(3), pp. 515-524.
- [125] Sakuma, K., Kohara, S., Sueoka, K., Orii, Y., Kawakami, M., Asai, K., Hirayama, Y., and Knickerbocker, J. U., 2011, "Development of Vacuum Underfill Technology for a 3D Chip Stack," *Journal of Micromechanics and Microengineering*, **21**(3).
- [126] Myo, P., Chong, S. C., Xie, L., Ho, S. W., Toh, W. H. S., and Chai, T. C., 2010, "3D Stacking by Hybrid Bonding with Low Temperature Solder," *Proc. 12th Electronics Packaging Technology Conference (EPTC)*, pp. 246-250.

- [127] Gregory, C., Lueck, M., Huffman, A., Lannon, J. M., and Temple, D. S., 2012, "High Density Metal-Metal Interconnect Bonding with Pre-applied Fluxing Underfill," *Proc. 62nd Electronic Components and Technology Conference (ECTC)*, pp. 20-25.
- [128] Nimura, M., Mizuno, J., Sakuma, K., and Shoji, S., 2011, "Solder/Adhesive Bonding Using Simple Planarization Technique for 3D Integration," *Proc. 61st Electronic Components and Technology Conference (ECTC)*, pp. 1147-1152.
- [129] Nimura, M., Mizuno, J., Shigetou, A., Sakuma, K., Ogino, H., Enomoto, T., and Shoji, S., 2013, "Hybrid Au-Au Bonding Technology Using Planar Adhesive Structure for 3D Integration," *Proc. 63rd Electronic Components and Technology Conference (ECTC)*, pp. 1153-1157.
- [130] Nimura, M., Mizuno, J., Shigetou, A., Sakuma, K., Ogino, H., Enomoto, T., and Shoji, S., 2013, "Study on Hybrid Au-Underfill Resin Bonding Method With Lock-and-Key Structure for 3-D Integration," *IEEE Transactions on Components, Packaging and Manufacturing Technology*, **3**(4), pp. 558-565.
- [131] Kohara, S., Horibe, A., Sueoka, K., Matsumoto, K., Yamada, F., Orii, Y., Sakuma, K., Kinoshita, T., and Kawakami, T., 2012, "Thermal Stress Analysis of Die Stacks with Fine-Pitch IMC Interconnections for 3D Integration," *Proc. IEEE International 3D Systems Integration Conference (3DIC)*, pp. 1-7.
- [132] Dong, X., and Xie, Y., 2009, "System-level Cost Analysis and Design Exploration for Three-Dimensional Integrated Circuits (3D ICs)," *Proc. 14th Asia and South Pacific Design Automation Conference (ASP-DAC 2009)*, pp. 234-241.
- [133] Chen, Y., Niu, D., Xie, Y., and Chakrabarty, K., 2010, "Cost-Effective Integration of Three-Dimensional (3D) ICs Emphasizing Testing Cost Analysis," *Proc. IEEE/ACM International Conference on Computer-Aided Design (ICCAD)*, pp. 471-476.
- [134] Lecarpentier, G., Agarwal, R., WenqiZhang, Limaye, P., Labie, R., Phommahaxay, A., and Soussan, P., 2010, "Die-to-Wafer Bonding of Thin Dies Using a 2-Step Approach; High Accuracy Placement, then Gang Bonding " *Proc. 6th Int'l Conference & Exhibit on Device Packaging*.
- [135] Ko, C.-T., and Chen, K.-N., 2010, "Wafer Level Bonding/Stacking Technology for 3D Integration," *Microelectronics Reliability*, **50**(4), pp. 481-488.
- [136] Ko, C.-T., Hsiao, Z.-C., Chang, Y.-J., Chen, P.-S., Hwang, Y.-J., Fu, H.-C., Huang, J.-H., Chiang, C.-W., Sheu, S.-S., Chen, Y.-H., Lo, W.-C., and Chen, K.-N., 2012, "A Wafer-Level Three-Dimensional Integration Scheme With Cu TSVs Based on Microbump/Adhesive Hybrid Bonding for Three-Dimensional Memory

Application,” *IEEE Transactions on Device and Materials Reliability*, **12**(2), pp. 209-216.

- [137] Chang, Y. J., Ko, C. T., Hsiao, Z. C., Yu, T. H., Chen, Y. H., Lo, W. C., and Chen, K. N., 2012, “Electrical Characterization and Reliability Investigations of Cu TSVs with Wafer-Level Cu/Sn-BCB Hybrid Bonding,” *Proc. International Symposium on VLSI Technology, Systems, and Applications (VLSI-TSA)*, pp. 1-2.
- [138] Liu, F., Yu, R. R., Young, A. M., Doyle, J. P., Wang, X., Shi, L., Chen, K. N., Li, X., Dipaola, D. A., Brown, D., Ryan, C. T., Hagan, J. A., Wong, K. H., Lu, M., Gu, X., Klymko, N. R., Perfecto, E. D., Merryman, A. G., Kelly, K. A., Purushothaman, S., Koester, S. J., Wisnieff, R., and Haensch, W., 2008, “A 300-mm Wafer-Level Three-Dimensional Integration Scheme Using Tungsten Through-Silicon Via and Hybrid Cu-Adhesive Bonding,” *Proc. IEEE International Electron Devices Meeting (IEDM)*, pp. 1-4.
- [139] Huyghebaert, C., Van Olmen, J., Civale, Y., Phommahaxay, A., Jourdain, A., Sood, S., Farrens, S., and Soussan, P., 2010, “Cu to Cu Interconnect Using 3D-TSV and Wafer to Wafer Thermocompression Bonding,” *Proc. 2010 International Interconnect Technology Conference (IITC)*, pp. 1-3.
- [140] Swinnen, B., Ruythooren, W., De Moor, P., Bogaerts, L., Carbonell, L., De Munck, K., Eyckens, B., Stoukatch, S., Sabuncuoglu Tezcan, D., Tokei, Z., Vaes, J., Van Aelst, J., and Beyne, E., 2006, “3D Integration by Cu-Cu Thermo-Compression Bonding of Extremely Thinned Bulk-Si Die Containing 10 μm Pitch Through-Si Vias,” *Proc. International Electron Devices Meeting (IEDM '06)*, pp. 1-4.
- [141] Diehl, D., Kitada, H., Maeda, N., Fujimoto, K., Ramaswami, S., Sirajuddin, K., Yalamanchili, R., Eaton, B., Rajagopalan, N., Ding, R., Patel, S., Cao, Z., Gage, M., Wang, Y., Tu, W., Kim, S. W., Kulzer, R., Drucker, I., Erickson, D., Ritzdorf, T., Nakamura, T., and Ohba, T., 2012, “Formation of TSV for the Stacking of Advanced Logic Devices Utilizing Bumpless Wafer-on-Wafer Technology,” *Microelectronic Engineering*, **92**, pp. 3-8.
- [142] Fujimoto, K., Maeda, N., Kitada, H., Kim, Y. S., Kodama, S., Nakamura, T., Suzuki, K., and Ohba, T., 2012, “Development of Cost-Effective Wafer Level Process for 3D-Integration with Bump-Less TSV Interconnects,” *Proc. 62nd Electronic Components and Technology Conference (ECTC)*, pp. 537-540.
- [143] Kitada, H., Maeda, N., Fujimoto, K., Suzuki, K., Kawai, A., Arai, K., Suzuki, T., Nakamura, T., and Ohba, T., 2009, “Stress Sensitivity Analysis on TSV Structure of Wafer-on-a-Wafer (WOW) by the Finite Element Method (FEM),” *Proc. IEEE International Interconnect Technology Conference (IITC)*, pp. 107-109.
- [144] Ramm, P., Lu, J. J.-Q., and Taklo, M. M. V., 2012, *Handbook of Wafer Bonding*, Wiley-VCH, Weinheim, Germany.

- [145] Chatterjee, R., Fayolle, M., Leduc, P., Pozder, S., Jones, B., Acosta, E., Charlet, B., Enot, T., Heitzmann, M., Zussy, M., Roman, A., Louveau, O., Maitrejean, S., Louis, D., Kernevez, N., Sillon, N., Passemard, G., Po, V., Mathew, V., Garcia, S., Sparks, T., and Zhihong, H., 2007, "Three Dimensional Chip Stacking using a Wafer-to-Wafer Integration," *Proc. IEEE International Interconnect Technology Conference (IITC)*, pp. 81-83.
- [146] Bernstein, K., Andry, P., Cann, J., Emma, P., Greenberg, D., Haensch, W., Ignatowski, M., Koester, S., Magerlein, J., Puri, R., and Young, A., 2007, "Interconnects in the Third Dimension: Design Challenges for 3D ICs," *Proc. 44th ACM/IEEE Design Automation Conference (DAC '07)*, pp. 562-567.
- [147] Skordas, S., Tulipe, D. C. L., Winstel, K., Vo, T. A., Priyadarshini, D., Upham, A., Song, D., Hubbard, A., Johnson, R., Cauffman, K., Kanakasabapathy, S., Lin, W., Knupp, S., Malley, M., Farooq, M. G., Hannon, R., Berger, D., and Iyer, S. S., 2012, "Wafer-Scale Oxide Fusion Bonding and Wafer Thinning Development for 3D Systems Integration: Oxide Fusion Wafer Bonding and Wafer Thinning Development for TSV-Last Integration," *Proc. 3rd IEEE International Workshop on Low Temperature Bonding for 3D Integration (LTB-3D)*, pp. 203-208.
- [148] Pozder, S., Chatterjee, R., Jain, A., Huang, Z., Jones, R. E., and Acosta, E., 2007, "Progress of 3D Integration Technologies and 3D Interconnects," *Proc. IEEE International Interconnect Technology Conference (IITC)*, pp. 213-215.
- [149] Enquist, P., Fountain, G., Petteway, C., Hollingsworth, A., and Grady, H., 2009, "Low Cost of Ownership Scalable Copper Direct Bond Interconnect 3D IC Technology for Three Dimensional Integrated Circuit Applications," *Proc. IEEE International Conference on 3D System Integration (3DIC)*, pp. 1-6.
- [150] Radu, I., Landru, D., Gaudin, G., Riou, G., Tempesta, C., Letertre, F., Di Cioccio, L., Gueguen, P., Signamarcheix, T., Euvrard, C., Dechamp, J., Clavelier, L., and Sadaka, M., 2010, "Recent Developments of Cu-Cu Non-Thermocompression Bonding for Wafer-to-Wafer 3D Stacking," *Proc. IEEE International 3D Systems Integration Conference (3DIC)* pp. 1-6.
- [151] Lau, J. H., Lee, C., Premachandran, C. S., and Yu, A., 2009, *Advanced MEMS Packaging*, McGraw-Hill Companies, Inc.
- [152] Ristic, L., 2012, "Sensor fusion and MEMS for 10-DoF solutions," <http://www.embedded.com/print/4395167>.
- [153] Liu, X., Chen, Q., Dixit, P., Chatterjee, R., Tummala, R. R., and Sitaraman, S. K., 2009, "Failure mechanisms and optimum design for electroplated copper Through-Silicon Vias (TSV)," *Proc. 59th Electronic Components and Technology Conference*, pp. 624-629.

- [154] Chung, H., Tu, C.-M., Lwo, B.-J., and Lee, C.-Y., 2013, "A Complete Resistance Extraction Methodology and Circuit Models for Typical TSV Structures," *International Journal of Electronics*, **100**(9), pp. 1256-1269.
- [155] Gagnard, X., and Mourier, T., 2010, "Through Silicon Via: From the CMOS Imager Sensor Wafer Level Package to the 3D Integration," *Microelectronic Engineering*, **87**(3), pp. 470-476.
- [156] Wang, M.-J., Hung, C.-Y., Kao, C.-L., Lee, P.-N., Chen, C.-H., Hung, C.-P., and Tong, H.-M., 2012, "TSV Technology for 2.5 D IC Solution," *Proc. 62nd Electronic Components and Technology Conference (ECTC)*, IEEE, pp. 284-288.